

3-22-2018

An Efficient Euler Method to Predict Shock Migration on a Straked Delta Wing Design

Dylan N. Hope

Follow this and additional works at: <https://scholar.afit.edu/etd>

Part of the [Aerodynamics and Fluid Mechanics Commons](#)

Recommended Citation

Hope, Dylan N., "An Efficient Euler Method to Predict Shock Migration on a Straked Delta Wing Design" (2018). *Theses and Dissertations*. 1772.

<https://scholar.afit.edu/etd/1772>

This Thesis is brought to you for free and open access by the Student Graduate Works at AFIT Scholar. It has been accepted for inclusion in Theses and Dissertations by an authorized administrator of AFIT Scholar. For more information, please contact richard.mansfield@afit.edu.



AN EFFICIENT EULER METHOD TO PREDICT
SHOCK MIGRATION ON AN OSCILLATING
STRAKED DELTA WING DESIGN

THESIS

Dylan N. Hope, 2nd Lt, USAF

AFIT-ENY-MS-18-M-264

DEPARTMENT OF THE AIR FORCE
AIR UNIVERSITY

AIR FORCE INSTITUTE OF TECHNOLOGY

Wright-Patterson Air Force Base, Ohio

DISTRIBUTION STATEMENT A. APPROVED FOR PUBLIC RELEASE;
DISTRIBUTION UNLIMITED.

The views expressed in this thesis are those of the author and do not reflect the official policy or position of the United States Air Force, Department of Defense, or the United States Government.

AFIT-ENY-MS-18-M-264

AN EFFICIENT EULER METHOD TO PREDICT
SHOCK MIGRATION ON AN OSCILLATING
STRAKED DELTA WING DESIGN

THESIS

Presented to the Faculty
Department of Aeronautics and Astronautics
Graduate School of Engineering and Management
Air Force Institute of Technology
Air University
Air Education and Training Command
In Partial Fulfillment of the Requirements for the
Degree of Master of Science in Aeronautical Engineering

Dylan N. Hope, BSAE
2nd Lt, USAF

March, 2018

DISTRIBUTION STATEMENT A. APPROVED FOR PUBLIC RELEASE;
DISTRIBUTION UNLIMITED.

Abstract

In support of the Air Force Office of Scientific Research, this project sought to identify the significance of nonlinear aerodynamic phenomena in regards to LCO of a straked delta wing design. Previous works include unsteady Navier-Stokes aeroelastic analysis of various wing designs and flight test of F-16 transonic LCO with interest focused on oscillatory SITES behavior. The research presented within this investigation further expanded the understanding of unsteady aerodynamics by performing aeroelastic analysis of a wing oscillated in pitch with an Euler-based, boundary layer coupled numerical method (ZEUS).

The wing was tested for a multitude of LCO parameters such as median AoA, oscillation amplitude, oscillation frequency, Mach number, and the type of numerical solver used. Computed pressure data sets were analyzed along the wing's surface at 4 chordwise stations along the wing's span.

Results indicate that oscillatory shock migration occurs in response to the pitching motion of the wing. ZEUS has the capability to run either a fully inviscid solution or a boundary layer coupled solution (BLC). While the use of both methods found shock migration to occur, the BLC solution predicted more significant shock migration. The inviscid solution predicted more aggressive shocks located further aft on the wing than the BLC solution. In regards to oscillation amplitude, increasing the amplitude resulted in a greater range of shock migration than lower amplitude cases. Both oscillation frequencies tested did not show any noteworthy differences. The aforementioned findings support the theory that potential oscillatory shock migration can occur during certain cases of transonic LCO. In addition, it was concluded that based on the flow solver used (ZEUS), shock movement during LCO is not purely a function of viscosity (SITES), although the modeling of viscous effects does affect the range of shock migration.

Table of Contents

	Page
Abstract	ii
List of Figures	v
List of Tables	xi
List of Symbols	xii
List of Abbreviations	xiii
I. Introduction	1
1.1 Background and Motivations	2
1.2 Research Objectives	4
II. Literature Review	6
2.1 Introduction	6
2.2 Fundamentals of Linear Aeroelastic Analysis	6
2.3 LCO Theory	9
2.3.1 Store Aerodynamics	10
2.3.2 Shock Induced Trailing Edge Separation	12
2.3.3 Nonlinear Structural Damping	15
2.3.4 Computational Analysis of LCO	16
2.4 Current AFSEO Methodology	18
2.5 Straked Delta Wing Wind Tunnel Experiment by Cunningham	19
2.6 Chapter Summary	24
III. Methodology	25
3.1 Introduction	25
3.2 ZEUS	25
3.2.1 Mesh Generation and Finite Element Model	25
3.2.2 Unsteady Euler Solver on Stationary Cartesian Grid	28
3.2.3 Time-Accurate Euler Method	29
3.2.4 Transpiration Boundary Conditions	33
3.2.5 Boundary Layer Coupling	34
3.2.6 Integral Boundary Layer Method	34
3.2.7 Boundary Layer Coupling Scheme	36
3.2.8 Time Steps and Loops in ZEUS	37
3.3 Computational Model	38
3.3.1 Matching of Reynolds Number	38

	Page
3.3.2 Computational Model Design	40
3.3.3 Grid Sensitivity Study	42
3.4 Test Matrix	44
3.4.1 Sinusoidal Transient Effects	44
3.5 Post Processing of Data	45
IV. Results and Analysis	46
4.1 Introduction	46
4.2 Fully Inviscid and Boundary Layer Coupled Solution	48
4.3 Effects of Median AoA and Oscillation Amplitude	54
4.4 Frequency Comparison	57
4.5 Comparison of Shock Migration at Various Spanwise Locations	63
4.6 Variation in Moment Coefficient	68
4.7 Summary of Results	72
V. Conclusions and Recommendations	74
5.1 Shock Migration and Variable Shock Strength during LCO	74
5.1.1 Shock Migration	74
5.1.2 Change in C_p during Oscillation	74
5.2 Future Research Areas	75
5.2.1 Validation of ZEUS results	75
5.2.2 Replicate Experiment with a Navier-Stokes Solver	76
Appendix A. C_p Data for Wing Station 1	77
Appendix B. C_p Data for Wing Station 2	89
Appendix C. C_p Data for Wing Station 3	101
Appendix D. C_p Data for Wing Station 4	113
Appendix E. Temporal Comparison of each wing station	125
Bibliography	132
Vita	135

List of Figures

Figure		Page
1.1	Example of LCO.	3
2.1	Flow features on an airfoil at and above the critical Mach number. (Federal Aviation Administration, 2004: 15-7)	13
2.2	Simple Wing/Strake Configuration. Pressure sensors are located along the dotted lines labled 1-4. (dimensions in mm) [8]	21
2.3	Dimensions of wing panel (dimensions in mm) [8]. The computational model used in this study is slightly different than the model presented here.	22
2.4	An example of a test matrix used in Cunninghamman’s experiment. [8]	23
3.1	Mesh Generation, Top View, Close. XY plane view of the computational mesh.	26
3.2	Mesh Generation, Top View, Full. XY plane view of the computational mesh.	27
3.3	Mesh Generation, Close View. ZEUS uses a built-in, automated mesh generation scheme to extrapolate a 3-D mesh from the 2-D panel distribution along the wing’s surface.	28
3.4	Mesh Generation, Full View. ZEUS uses a built-in, automated mesh generation scheme to extrapolate a 3-D mesh from the 2-D panel distribution along the wing’s surface.	29
3.5	Flow Chart of the Euler Solver in ZEUS. NCYC, NEQTN and NSTEP refer to input parameters within ZEUS [32].	37
3.6	Dimensioned Top View of Wing. All dimensions on the drawing are in units of mm. Planform area is equal to 0.144 m ² . Chord length is 0.8207 m. Span is 0.435.8 m.	40
3.7	3-D View of the computational SiS model at AoA = 4°. The 4 black lines on the outer wing section indicate the locations along which Cp was evaluated. The locations denote C _{p1} , C _{p2} , C _{p3} and C _{p4} with the following physical locations: y = 209 mm, 274 mm, 336 mm and 395 mm from the centerline, respectively. C _{p1} is located most inboard and C _{p4} nearest the right wing tip.	41

Figure		Page
3.8	Grid Sensitivity. The plot depicts changes in the trim AoA as a function of panel density for a load factor of 1. The label below each point indicates the number of spanwise and chordwise distributions along the wing, respectively.	42
3.9	Aerodynamic Panels on Wing. 1400 panels were created from a distribution of 41 nodes along the chord and 36 nodes across the span of the Wing.	43
4.1	Example figure indicating the min and max C_p and $\frac{x}{c}$ as well as C_{p0} for the time trace of C_{p1} . $M = 0.9$, Frequency = 5.7 Hz, Trim = 4° , $\Delta\alpha = 4^\circ$	48
4.2	Inviscid/Viscous comparison for C_{p1} . $M = 0.9$, Frequency = 5.7 Hz, Trim = 4°	51
4.3	Inviscid/Viscous comparison for C_{p1} . $M = 0.9$, Frequency = 5.7 Hz, Trim = 10°	52
4.4	Inviscid/Viscous comparison for C_{p4} . $M = 0.9$, Frequency = 5.7 Hz, Trim = 7°	53
4.5	BLC trim and $\Delta\alpha$ comparison for C_{p1} . $M = 0.9$, Frequency = 5.7 Hz.	55
4.6	BLC trim and $\Delta\alpha$ comparison for C_{p1} . $M = 0.95$, Frequency = 5.7 Hz.	56
4.7	BLC frequency comparison for C_{p1} . $M = 0.9$, Frequency = 5.7/7.4 Hz.	59
4.8	BLC frequency comparison for C_{p4} . $M = 0.95$, Frequency = 5.7/7.4 Hz.	60
4.9	Time history of C_p for three points along the chord of position 1. $M = 0.9$, Frequency = 5.7 Hz.	61
4.10	Time history of C_p for three points along the chord of position 3. $M = 0.95$, Frequency = 5.7 Hz.	62
4.11	Time history of C_p for all 4 positions along the wing. The chordwise position, X, has been normalized by the root chord to retain each position's relative distance to one another. $t^* = 0.23, 0.74$ indicate peak nose up and nose down of the wing, respectively. $M = 0.9$, Frequency = 5.7 Hz, Trim = 4° , $\Delta\alpha = 2^\circ$	64

Figure		Page
4.12	Time history of C_p for all 4 positions along the wing. The chordwise position, X, has been normalized by the root chord to retain each position's relative distance to one another. $t^* = 0.23, 0.74$ indicate peak nose up and nose down of the wing, respectively. $M = 0.9$, Frequency = 5.7 Hz, Trim = 7° , $\Delta\alpha = 4^\circ$	65
4.13	Time stamp of C_p when $t^* = 0.0$ indicating trimmed position. $M = 0.9$, Frequency = 5.7 Hz, Trim = 7° , $\Delta\alpha = 4^\circ$	66
4.14	Time stamp of C_p when $t^* = 0.0$ indicating peak nose up position. $M = 0.9$, Frequency = 5.7 Hz, Trim = 7° , $\Delta\alpha = 4^\circ$	66
4.15	Time stamp of C_p when $t^* = 0.0$ indicating oscillating nose down past trim. $M = 0.9$, Frequency = 5.7 Hz, Trim = 7° , $\Delta\alpha = 4^\circ$	67
4.16	Time stamp of C_p when $t^* = 0.0$ indicating peak nose down position. $M = 0.9$, Frequency = 5.7 Hz, Trim = 7° , $\Delta\alpha = 4^\circ$	67
4.17	Variation in the pitching moment coefficient about the quarter-chord for each wing station over the course of a single oscillation. $M = 0.9$, Frequency = 5.7 Hz, Trim = 04° , $\Delta\alpha = \pm 2^\circ, \pm 4^\circ$, BLC and Inviscid.	69
4.18	Variation in the pitching moment coefficient about the quarter-chord for each wing station over the course of a single oscillation. $M = 0.9$, Frequency = 5.7 Hz, Trim = 07° , $\Delta\alpha = \pm 2^\circ, \pm 4^\circ$, BLC and Inviscid.	70
4.19	Variation in the pitching moment coefficient about the quarter-chord for each wing station over the course of a single oscillation. $M = 0.9$, Frequency = 5.7 Hz, Trim = 10° , $\Delta\alpha = \pm 2^\circ, \pm 4^\circ$, BLC and Inviscid.	71
A.1	Frequency Comparison. Time history of C_p for $M = 0.90$, Frequency = 5.7 Hz.	78
A.2	Frequency Comparison. Time history of C_p for $M = 0.90$, Frequency = 7.4 Hz.	79
A.3	Time history of C_p for for three points along the chord of station 1. $M = 0.90$, Frequency = 5.7 Hz.	80
A.4	Time history of C_p for for three points along the chord of station 1. $M = 0.95$, Frequency = 5.7 Hz.	81
A.5	Mach Comparison. Time history of C_p varying Mach number down the column. Frequency = 5.7 Hz, Trim = 4°	82

Figure		Page
A.6	Mach Comparison. Time history of C_p varying Mach number down the column. Frequency = 5.7 Hz, Trim = 7°.	83
A.7	BLC trim and $\Delta\alpha$ comparison of C_p . M = 0.9, Frequency = 5.7 Hz.	84
A.8	BLC trim and $\Delta\alpha$ comparison of C_p . M = 0.95, Frequency = 5.7 Hz.	85
A.9	Inviscid/Viscous comparison of C_p . M = 0.9, Frequency = 5.7 Hz, Trim = 4°.	86
A.10	Inviscid/Viscous comparison of C_p . M = 0.9, Frequency = 5.7 Hz, Trim = 7°.	87
A.11	Inviscid/Viscous comparison of C_p . M = 0.9, Frequency = 5.7 Hz, Trim = 10°.	88
B.1	Frequency Comparison. Time history of C_p for M = 0.90, Frequency = 5.7 Hz.	90
B.2	Frequency Comparison. Time history of C_p for M = 0.90, Frequency = 7.4 Hz.	91
B.3	Time history of C_p for for three points along the chord of station 2. M = 0.90, Frequency = 5.7 Hz.	92
B.4	Time history of C_p for for three points along the chord of station 2. M = 0.95, Frequency = 5.7 Hz.	93
B.5	Mach Comparison. Time history of C_p varying Mach number down the column. Frequency = 5.7 Hz, Trim = 4°.	94
B.6	Mach Comparison. Time history of C_p varying Mach number down the column. Frequency = 5.7 Hz, Trim = 7°.	95
B.7	BLC trim and $\Delta\alpha$ comparison of C_p . M = 0.9, Frequency = 5.7 Hz.	96
B.8	BLC trim and $\Delta\alpha$ comparison of C_p . M = 0.95, Frequency = 5.7 Hz.	97
B.9	Inviscid/Viscous comparison of C_p . M = 0.9, Frequency = 5.7 Hz, Trim = 4°.	98
B.10	Inviscid/Viscous comparison of C_p . M = 0.9, Frequency = 5.7 Hz, Trim = 7°.	99
B.11	Inviscid/Viscous comparison of C_p . M = 0.9, Frequency = 5.7 Hz, Trim = 10°.	100

Figure		Page
C.1	Frequency Comparison. Time history of C_p for $M = 0.90$, Frequency = 5.7 Hz.	102
C.2	Frequency Comparison. Time history of C_p for $M = 0.90$, Frequency = 7.4 Hz.	103
C.3	Time history of C_p for for three points along the chord of station 3. $M = 0.90$, Frequency = 5.7 Hz.	104
C.4	Time history of C_p for for three points along the chord of station 3. $M = 0.95$, Frequency = 5.7 Hz.	105
C.5	Mach Comparison. Time history of C_p varying Mach number down the column. Frequency = 5.7 Hz, Trim = 4°.	106
C.6	Mach Comparison. Time history of C_p varying Mach number down the column. Frequency = 5.7 Hz, Trim = 7°.	107
C.7	BLC trim and $\Delta\alpha$ comparison of C_p . $M = 0.9$, Frequency = 5.7 Hz.	108
C.8	BLC trim and $\Delta\alpha$ comparison of C_p . $M = 0.95$, Frequency = 5.7 Hz.	109
C.9	Inviscid/Viscous comparison of C_p . $M = 0.9$, Frequency = 5.7 Hz, Trim = 4°.	110
C.10	Inviscid/Viscous comparison of C_p . $M = 0.9$, Frequency = 5.7 Hz, Trim = 7°.	111
C.11	Inviscid/Viscous comparison of C_p . $M = 0.9$, Frequency = 5.7 Hz, Trim = 10°.	112
D.1	Frequency Comparison. Time history of C_p for $M = 0.90$, Frequency = 5.7 Hz.	114
D.2	Frequency Comparison. Time history of C_p for $M = 0.90$, Frequency = 7.4 Hz.	115
D.3	Time history of C_p for for three points along the chord of station 4. $M = 0.90$, Frequency = 5.7 Hz.	116
D.4	Time history of C_p for for three points along the chord of station 4. $M = 0.95$, Frequency = 5.7 Hz.	117
D.5	Mach Comparison. Time history of C_p varying Mach number down the column. Frequency = 5.7 Hz, Trim = 4°.	118

Figure	Page
D.6	Mach Comparison. Time history of C_p varying Mach number down the column. Frequency = 5.7 Hz, Trim = 7°. 119
D.7	BLC trim and $\Delta\alpha$ comparison of C_p . M = 0.9, Frequency = 5.7 Hz. 120
D.8	BLC trim and $\Delta\alpha$ comparison of C_p . M = 0.95, Frequency = 5.7 Hz. 121
D.9	Inviscid/Viscous comparison of C_p . M = 0.9, Frequency = 5.7 Hz, Trim = 4°. 122
D.10	Inviscid/Viscous comparison of C_p . M = 0.9, Frequency = 5.7 Hz, Trim = 7°. 123
D.11	Inviscid/Viscous comparison of C_p . M = 0.9, Frequency = 5.7 Hz, Trim = 10°. 124
E.1	C_p on the wing's surface for all 4 chordwise stations. Each plot indicates a temporal snap shot for the test case: M = 0.90, Frequency = 5.7 Hz, Trim = 4°, $\Delta\alpha = \pm 2^\circ$ 126
E.2	C_p on the wing's surface for all 4 chordwise stations. Each plot indicates a temporal snap shot for the test case: M = 0.90, Frequency = 5.7 Hz, Trim = 4°, $\Delta\alpha = \pm 4^\circ$ 127
E.3	C_p on the wing's surface for all 4 chordwise stations. Each plot indicates a temporal snap shot for the test case: M = 0.90, Frequency = 5.7 Hz, Trim = 7°, $\Delta\alpha = \pm 2^\circ$ 128
E.4	C_p on the wing's surface for all 4 chordwise stations. Each plot indicates a temporal snap shot for the test case: M = 0.90, Frequency = 5.7 Hz, Trim = 7°, $\Delta\alpha = \pm 4^\circ$ 129
E.5	C_p on the wing's surface for all 4 chordwise stations. Each plot indicates a temporal snap shot for the test case: M = 0.90, Frequency = 5.7 Hz, Trim = 10°, $\Delta\alpha = \pm 2^\circ$ 130
E.6	C_p on the wing's surface for all 4 chordwise stations. Each plot indicates a temporal snap shot for the test case: M = 0.90, Frequency = 5.7 Hz, Trim = 10°, $\Delta\alpha = \pm 4^\circ$ 131

List of Tables

Table		Page
3.1	Test Matrix. The SiS model was run for various combinations of Mach, trim, oscillation amplitude and oscillation frequency. x and o indicate an oscillation frequency of 5.7 Hz and 7.4 Hz, respectively. I indicates a fully inviscid test case.	44
4.1	Tabulated Results for cases of interest for position 1 on the wing. The shock movement is reported in percent of local chord. The percent change in C_p from the shock migration is reported as $(C_{p,max} - C_{p,min})/C_{p0}$	73

List of Symbols

Symbol		Page
M	Mass Matrix	6
C	Damping Matrix	6
K	Stiffness Matrix	6
x	Structural Deformation	6
F_a	Aerodynamic Forces	6
F_e	External Forces	6
q_∞	Dynamic Pressure	7
H	Aerodynamic Influence Coefficient Matrix	7
Φ	Modal Matrix, Total Velocity Potential	8

List of Abbreviations

Abbreviation		Page
LCO	Limit Cycle Oscillation	1
AFSEO	Air Force SEEK EAGLE Office	1
AFB	Air Force Base	1
SITES	Shock Induced Trailing Edge Separation	4
ZEUS	ZONA Euler Unsteady Solver	4
EOM	Equation of Motion	6
AIC	Aerodynamic Influence Coefficient	7
EA	Elastic Axis	10
AoA	Angle of Attack	13
RANS	Reynolds-averaged Navier Stokes	13
TPS	Test Pilot School	14
NSD	Nonlinear Structural Damping	15
CFD	Computational Fluid Dynamics	18
FEM	Finite Element Method	26
SBLI	Shock Boundary Layer Interaction	48
BLC	Boundary Layer Coupled	48

AN EFFICIENT EULER METHOD TO PREDICT SHOCK MIGRATION ON AN OSCILLATING STRAKED DELTA WING DESIGN

I. Introduction

As modern threats emerge and evolve, so must the development of new weapon systems. Along with the advent of these new systems, current delivery platforms, such as the multi-role F-16 aircraft, must be able to safely handle and accommodate unforeseen load variations. F-16s are required to achieve both high altitudes and supersonic speeds, which leads to thin airfoil shapes and reduced weight structures. The introduction of heavy loads from newly designed weapon systems compounded with thin, flexible wing structures of the F-16 can result in an aeroelastic instability known as flutter and an aeroelastic nonlinearity known as limit cycle oscillations (LCO). LCO results in undesirable airframe vibrations which can adversely affect pilot performance and degrade targeting accuracy. Additionally, the occurrence of LCO can lead to increased maintenance costs and reduced system lifespan.

The F-16 has nine traditional load stations: a pair of wingtip stations; a pair of underwing missile stations; a pair of generally air-to-ground stations; a pair of inboard stations which can be used to carry external fuel stores; and a centerline station. Due to the ever increasing number of available weapon systems, the total number of possible permutations of load configurations on the F-16 grows. Each of these load configurations must first be certified by the Air Force SEEK EAGLE Office (AFSEO) before the configuration may be flown operationally.

AFSEO is responsible for the test, evaluation, and certification of external equipment and munitions carried by Air Force aircraft. As of 1983, AFSEO at Eglin Air Force Base (AFB) has conducted all flutter testing of the F-16. Considering the extensive analysis conducted during flight test, it would be impractical to test all available

load configurations for the numerous flight regimes of the F-16 due to constraints on time, cost and manpower. Thus, computational techniques which emphasize rapid solutions with minimal sacrifice to accuracy are required to identify flutter sensitive configurations [20, p. 1]. Subsequently, only the most critical configurations will require flight test validation. When employed successfully, a computational approach to flight test will lead to reduced costs and expedited fielding of new weapon systems required by the warfighter.

1.1 Background and Motivations

Aeroelasticity is the term used to describe the field of study concerned with the interaction of the aerodynamic forces imposed on an elastic structure in an airstream and the resulting deformation, both statically and dynamically. Classical aerodynamics allows for the prediction of forces on a body given a flow condition. Elasticity is used to determine the deflection of an elastic body under a load. Dynamics introduces the effect due to inertial forces. When all three aforementioned fields are applied simultaneously, the process is used to conduct dynamic aeroelastic analysis.

In regards to static aeroelasticity, divergence is an important property which results in catastrophic failure. Divergence occurs when the deformation of a lifting surface serves to increase the aerodynamic load, thus leading to further deformation of the structure; this process continues until complete failure of the structure [18, p. 127]. Flutter is similar to divergence, but it is a dynamic aeroelastic phenomenon. Flutter is a self-excited dynamic instability in which the aerodynamic forces on a flexible body couple with the structure's natural modes of vibration to produce oscillatory behavior of increasing amplitude [18, p. 175-176]. In general, two or more modes of vibration, such as bending and torsional motion, which under the influence of unsteady aerodynamic forces, interact with each other in such a way that energy is transferred from the passing airstream into the vibrating structure. A special case of nonlinear flutter in which the amplitude of the oscillations remains constant is known as a limit cycle oscillation.

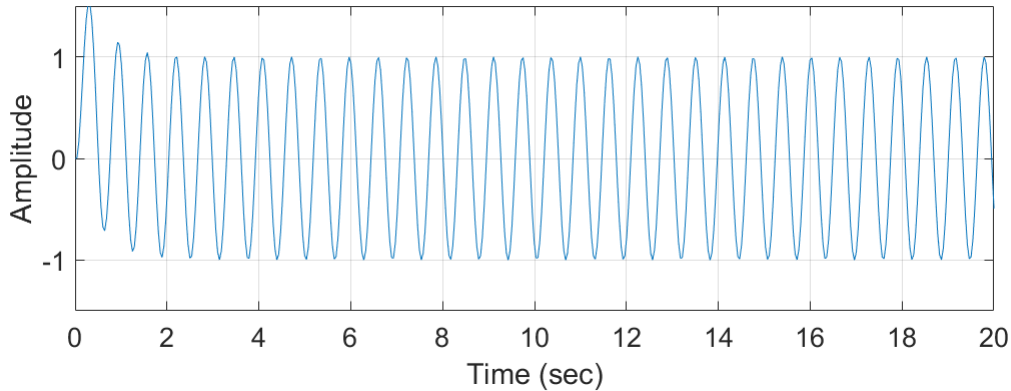


Figure 1.1: Example of LCO.

Limit cycle oscillations are defined as self-sustained oscillations in which there is a balance between the destabilizing and restoring forces of a system, thus LCO lies on the boundary of instability [22, p. 1]. In regards to aeroelastic LCO, aerodynamic forces are translated into the aircraft's structure, which in turn deforms due to the applied load. The resultant deformation alters the aerodynamic forces and the process is repeated such that there is a balance between the structural restoring forces and aerodynamic loads. The motion of LCO is unique in that the motion is of limited amplitude, cyclic (motion repeats for a given time period) and oscillatory (vibrational amplitude occurs around some mean value). This means that in its most fundamental state, LCO is defined by sinusoidal motion [2, p. 1]. Figure 1.1 depicts a hypothetical LCO in which some perturbation disturbs the system from rest, resulting in the quasi-steady, nonlinear oscillatory motion of the system attempting to return to equilibrium.

The F-16 and F/A-18 are LCO prone at high subsonic and transonic speeds for store configurations with AIM-9 missiles on the wingtips and heavy stores on the outboard pylons. The LCO response is primarily characterized by antisymmetric motion of the wing and stores and lateral motion of the fuselage. In the case of the F-16, LCO occurs at both elevated aircraft load factor maneuvers and level flight, while the vibrations may be self-excited or induced by control inputs. Once initiated, the oscillations perpetuate until flight conditions are altered to a non-LCO prone condition. [2, p. 1].

The phenomenon of LCO is considered to be closely linked to classical flutter with the exception that the coupling of the unsteady aerodynamic forces and structural response is nonlinear in nature [2, p. 1]. Due to the complicated nature of LCO, the nonlinear differential equations of motion which govern this vibration infrequently have no analytical solution. Modern computational flutter analyses can accurately predict the frequency of LCO and the predicted flutter speed with zero damping is often quite representative of the LCO onset speed in straight, level flight. When considering more applicable portions of the flight regime such as transonic flight, classical linear flutter analysis techniques fail to predict the onset velocity or amplitude of LCO [10, p. 1].

Amongst aeroelasticians, there is little disagreement that LCO is a product of the nonlinear interaction of the structural and aerodynamic forces acting on the aircraft. However, there is no consensus as to which of these sources is the most significant contributor to the phenomenon. One possible explanation for the occurrence of transonic LCO is the presence of shock induced trailing edge separation (SITES). The role of SITES in limit cycles is thought to act as a nonlinear spring which both triggers and drives LCO [6]. SITES occurs when the flow in the boundary layer separates due to the pressure jump across a shock.

1.2 Research Objectives

The focus of this research is to provide further validation of ZONA Technologies Euler unsteady solver (ZEUS) as a tool to predict the onset and severity of LCO in the F-16. The program used for the flow analysis of the oscillating wing presented in this thesis is an Euler solver with the option to add a coupled boundary layer flow. As an Euler solver, the flow is assumed to be inviscid which raises the question, "Why use an inviscid solver when the aerodynamic phenomenon of interest is a viscous effect?". Although ZONA's Euler solver will fail to account for large regions of separation potentially caused by the formation of shocks, the primary interest is the shock movement as a result of wing oscillations.

ZEUS has been optimized to provide rapid solutions to unsteady flow fields and solutions can be run in a fraction of the time required for a full time-accurate Navier-Stokes solution. With the speed of an Euler solver in mind, ZEUS has the potential to provide predictive flight test capabilities for AFSEO and allow for a faster and more budget-friendly approach to flight test.

At the request of AFOSR project sponsors, the research will compare computational results from ZEUS to previous wind tunnel tests conducted by Cunningham [7] on a half-span straked delta wing design, which closely resembles the F-16's wing geometry. Cunningham's tests had the objectives to 1) understand the physics of unsteady transonic vortex flows about a simple straked delta wing and 2) to generate a steady and unsteady airloads data base for a simple straked delta wing to be used for validation of CFD computer codes. For the purposes of this research, a simple straked delta wing was oscillated in pitch for a variety of Mach numbers, trim conditions, oscillation amplitudes and oscillation frequencies in order to closely replicate the wind tunnel experiment and compare the results between the two sources. Additionally, the significance of viscous effects in shock migration was of particular interest. For this reason, fully inviscid and boundary layer coupled solutions were run in parallel to compare any disparities between the two methods.

II. Literature Review

2.1 Introduction

This chapter will provide an overview from a selection of the computational methods currently employed for aeroelastic analysis in addition to previous research and experiments relevant to limit cycle oscillations. As a precursor to LCO, this section will begin with a review of linear flutter analysis. Next, LCO theory will be discussed along with some of the possible sources of the nonlinear nature of LCO. A brief discussion focusing on AFSEO's approach to flutter and LCO testing will provide foundation for the motivation behind the author's research. Finally, the chapter will conclude with an in-depth analysis of Cunningham's [7] wind tunnel experiment which provides a basis for the author's own research.

2.2 Fundamentals of Linear Aeroelastic Analysis

Linear aeroelasticity begins with a summation of the forces on a lifting surface in the form of second order equations of motion in matrix form (EOM)

$$\mathbf{M}\ddot{\mathbf{x}}(t) + \mathbf{C}\dot{\mathbf{x}}(t) + \mathbf{K}\mathbf{x}(t) = \mathbf{F}(t) \quad (2.1)$$

where \mathbf{M} , \mathbf{C} , and \mathbf{K} are the mass, damping and stiffness matrices, respectively, generated by the structural FEM. The aerodynamic forces acting upon the lifting surface are located on the right hand side of the EOM and can be further defined as

$$\mathbf{F}(t) = \mathbf{F}_a(\mathbf{x}(t)) + \mathbf{F}_e(t) \quad (2.2)$$

where \mathbf{x} represents structural deformation, \mathbf{F}_a represents aerodynamic forces, and $\mathbf{F}_e(t)$ represents external forces such as impulse type gust loads, store ejection forces or control surface deflections due to pilot input [33, p. 2-1]. Should $\mathbf{F}_a(\mathbf{x}(t))$ be nonlinear with respect to time, then a discrete time approach with initial conditions is required.

To further define the system, dynamic pressure is denoted with q_∞ and an aerodynamic influence coefficient (AIC) with \mathbf{H} . We begin recasting (2.1) by assuming no external forces ($\mathbf{F}_e(t) = \mathbf{0}$) and that $\mathbf{F}_a(\mathbf{x})$ can be interpreted as an aerodynamic feedback term. Thus the aerodynamic feedback can be related to the structural deformation by way of a convolution integral:

$$\mathbf{F}_a(\mathbf{x}(t)) = \int_0^t q_\infty \mathbf{H} \left(\frac{L}{V}(t - \tau) \right) \mathbf{x}(\tau) d\tau \quad (2.3)$$

where:

- $q_\infty \mathbf{H}$ is the aerodynamic transfer function
- V is the freestream velocity
- τ is the integration variable

and:

- L is the reference length, typically half-chord [33].

The Laplace domain analogue of Equation 2.3 is

$$\mathbf{F}_a(\mathbf{x}(s)) = q_\infty \bar{\mathbf{H}} \left(\frac{sL}{V} \right) \mathbf{x}(s) \quad (2.4)$$

where:

- $\bar{\mathbf{H}}$ is the frequency domain counterpart of \mathbf{H}
- s is the complex number frequency parameter

which when combined with (2.1) simplifies to form the eigenproblem:

$$[s^2 \bar{\mathbf{M}} + s \bar{\mathbf{C}} + \bar{\mathbf{K}} - q_\infty \bar{\mathbf{H}} \left(\frac{sL}{V} \right)] \mathbf{x}(s) = 0 \quad (2.5)$$

The end result of (2.5) is a computationally intensive eigenproblem due to the large size of the mass, damping and stiffness matrices. Common practice makes a simplifying assumption that aeroelastic instabilities typically consist of interacting lower-order modes [33]. The “modal approach” truncates the infinite number of modes required for continuous system analysis: 50 natural modes are usually sufficient to conduct analysis of a whole aircraft structure [33, p. 2-3]:

$$\mathbf{x} = \Phi \mathbf{q} \quad \text{in the s-domain} \quad (2.6)$$

where Φ represents a modal matrix with only the selected lower order natural modes [33, p. 2-4]. The generalized coordinates, \mathbf{q} , is the eigenvector which will be determined. With the eigenvectors in hand, the structural deflections of the airframe are known and then aerodynamic forces can be calculated. With (2.4) and (2.6), the classical flutter matrix equation is produced:

$$[s^2 \mathbf{M} + s \mathbf{C} + \mathbf{K} - q_\infty \mathbf{Q}(\frac{sL}{V})] \mathbf{q} = 0 \quad (2.7)$$

where:

$$\begin{aligned} \mathbf{M} &= \Phi^T \bar{\mathbf{M}} \Phi \quad \text{is the generalized mass matrix with selected modes} \\ \mathbf{K} &= \Phi^T \bar{\mathbf{K}} \Phi \quad \text{is the generalized stiffness matrix with selected modes} \\ \mathbf{C} &= \Phi^T \bar{\mathbf{Z}} \Phi \quad \text{is the generalized damping matrix with selected modes} \end{aligned}$$

and:

$$\mathbf{Q}(\frac{sL}{V}) = \Phi^T \bar{\mathbf{H}}(\frac{sL}{V}) \Phi \quad \text{is the generalized aerodynamic forces matrix}$$

The solution process to generate the aerodynamic transfer function with unsteady aerodynamic methods is often facilitated by assuming simple harmonic motion. The frequency domain aerodynamic transfer function in matrix form is called

the Aerodynamic Influence Coefficient (AIC) [33, p. 2-4]. The formulation of the AIC matrices is the major functionality of ZAERO by way of the g-Method, a flutter solution method unique to ZAERO. The g-Method can robustly handle non-zero structural damping and represents the commercial state-of-the-art linear aeroelastic algorithm. Other linear aeroelastic algorithms include the K-Method, P-Method and P-K Method [4].

2.3 LCO Theory

The use of the term LCO in aeroelastic diction has become more prevalent since the 1970s to describe the dynamic response of some aircraft and external store configurations to encounter a sustained, oscillatory, periodic, but non-divergent motion within portions of the flight envelope. Historically, terms such as limit cycle flutter and limited amplitude flutter have been used as well. LCO differs from classical flutter primarily in that the nonlinear coupling of aerodynamic and structural forces causes the oscillations to grow from an initial perturbation to some limited amplitude. For typical LCO, the amplitude of the vibrations is constant for a stabilized flight condition. Once above the LCO onset speed, the amplitude of the vibration grows until a new flight speed is achieved. Once the speed is again stabilized, the periodic motion will continue, but at a greater amplitude than the vibrations at lower velocity.

Denegri reported two distinct types of LCO which occurred during the flutter test of the Block 15 F-16A [10]. He classified the two cases of LCO as typical and non-typical LCO. Typical LCO was characterized by a gradual onset of sustained limited amplitude oscillations of the wing where the amplitude increased with increasing Mach number and dynamic pressure. Non-typical LCO was unique in that the oscillations may only be present in a limited portion of the flight envelope.

Although it is easy to recognize the phenomenon, the true source of LCO remains shrouded due to the nonlinear nature of this aeroelastic response. Speculation of the root cause of LCO exists, whether it be aerodynamic nonlinearities, structural

nonlinearities, or a complex interaction of the two. For this reason, classical linear flutter analysis has been shown to adequately predict oscillation frequency and modal composition of the LCO mechanism, but unable to predict the onset speed or severity of the LCO [10, p. 1]. If the source/sources of LCO can be identified, computational models which better predict LCO characteristics can be developed. The following sections will discuss some of the prevailing theories concerning LCO from the perspective of a computational approach.

2.3.1 Store Aerodynamics. Several researchers have observed that many fighter aircraft experience LCO at speeds below the predicted flutter speed when carrying certain combinations of external stores [2, 7, 10, 13, 20, 25, 30]. Stores located under the wing and at the wing tip can affect LCO by altering the inertial properties of the wing or by changing the aerodynamics of the wing. Although the general trends for the addition of store mass in relation to the elastic axis (EA) are established, the role of store aerodynamics in LCO is still under investigation. The EA is a line which spans from the wing root to the wing tip and produces pure bending when a transverse force is applied or pure torsion when a moment is applied. If store mass is added forward of the EA, the flutter speed generally increases, producing a stabilizing effect, and vice versa for store mass added aft of the EA [19].

It has been hypothesized that store aerodynamics can affect LCO through two primary mechanisms: the store carriage loads transferred into the structure may sufficiently change the total forces experienced by the wing or the store could interfere with the airflow on the wing. In a study by Parker, Maple and Beran [25], it was found that store aerodynamics LCO influence are most likely a combination of both mechanisms. The aerodynamic nonlinearity responsible for LCO in the Goland wing was shock motion and periodic shock formation; stores were added to the underwing and wingtip locations to determine how store aerodynamics affected LCO characteristics. The aerodynamic forces on the store imparted energy into the structure increasing the

amplitude of LCO while underwing stores interfered with airflow along the bottom of the wing which served to limit the amplitude of LCO.

Several sources indicate that outboard stores and wingtip missiles play a significant role in LCO characteristics. Bunton found that both the F-16 and F/A-18 encounter LCO at high subsonic and transonic speeds for store configurations with heavy stores on the outboard pylons and AIM-9 missiles loaded on the wingtips [2]. A study by Dubben and Denegri found differences in LCO response characteristics associated with slight aerodynamic differences in underwing missiles [13]. Dubben discovered that slightly longer missiles with a raised collar section for the attachment of fins and canards displayed vastly different LCO response than shorter missiles. Computational analyses suggest that the fin collar has a significant effect on the wing pressure distribution.

A study presented by Hajj and Beran [16] performed higher-order spectral analysis to identify nonlinear aeroelastic phenomena responsible for LCO during a maneuver on the F-16. The results from flight test analysis showed that nonlinearities leading to the LCO were mostly present at the forward locations on the wingtip and underwing launchers. The detection of nonlinearities in the launchers and not at the pylon-wing interface indicates that the nonlinearities are associated with the aerodynamic or structural properties of the launcher.

Dowell et al. [15] implemented a nonlinear harmonic balance compressible RANS flow solver to model the unsteady aerodynamics of the F-16 wing. The aerodynamic model consisted of a clean wing with stores and missiles modeled by assuming aerodynamic slender body theory. The structural portion of the aeroelastic model consisted of modal masses and mode shapes obtained from a NASTRAN FEM. The structural inertia and stiffness of the stores were included in the structural model. The focus of his study was to detect any possible aerodynamic nonlinearities coinciding with LCO. Dowell found the flutter onset Mach number to be highly dependent on the geometry of the wing tip. Dowell reached the following conclusions:

1. An Euler or Navier-Stokes based CFD code is required to predict transonic flutter while a Navier-Stokes code is required for LCO prediction.
2. Correlation between computational results and flight test are highly sensitive to variations in structural frequencies and aerodynamic modeling of wingtip missile fins.
3. LCO frequency and structural modal participation were generally well predicted but mixed results were achieved with LCO amplitude prediction.

Dowell suggests modeling of flow separation on the missile fins and modeling of structural nonlinearities associated with the attachment points between the wing and missiles would lead to possible improvements to future computational methods.

2.3.2 Shock Induced Trailing Edge Separation. In addition to store aerodynamics, it has been proposed that shock induced trailing edge separation (SITES) may play a significant role in LCO characteristics, notably within the transonic regime. When an aircraft reaches its critical Mach number, the flow in some regions is sonic. A normal shock forms and decelerates the flow back to subsonic. Figure 2.1 illustrates the key features of transonic flow on an airfoil.

As the Mach number increases beyond the critical Mach number, a supersonic region forms on the airfoil and is in general terminated by a nearly normal shock, through which the flow is then returned to subsonic. With a further increase of the free stream Mach number, the shock moves aft while the strength of the shock increases. The adverse pressure gradient caused by the pressure jump across the shock can lead to boundary layer separation along the trailing edge. In addition to the changes in the Mach number, small variations in incidence may lead to considerable changes in the pressure distribution, shock position, and shock strength. If the boundary layer downstream of the shock separates completely, the flow can develop an unsteady phenomenon known as buzz. [29].

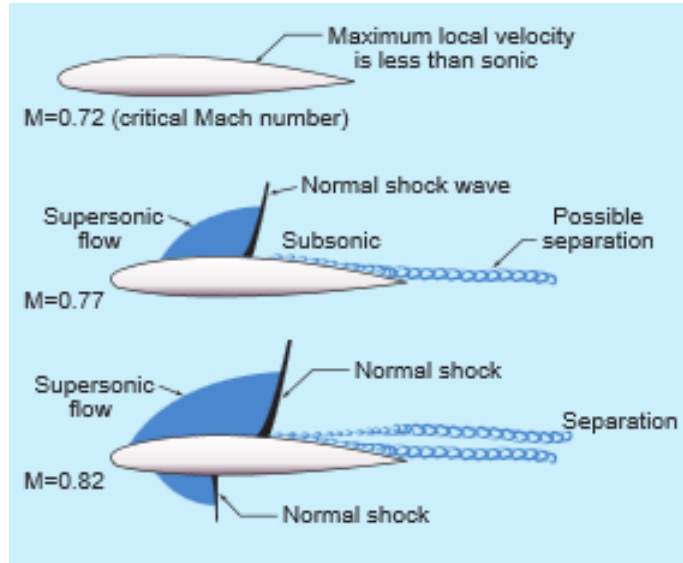


Figure 2.1: Flow features on an airfoil at and above the critical Mach number. (Federal Aviation Administration, 2004: 15-7)

The effect of SITES on LCO can be viewed as a feedback loop in which the oscillatory motion of the wing causes the migration of the shock, or the reverse case in which a self-sustained shock oscillation known as shock buffet can lead to vibrations in the wing. The shock oscillation serves to initiate shock buffet, a large-scale flow-induced shock motion which is self-sustained and repeated in an alternating fashion along the upper and lower surfaces of the airfoil. As the angle of attack (AoA) of a wing increases, the shock strength intensifies while moving aft. Once at a sufficiently high AoA, the boundary layer separates either at the foot of the shock or at the trailing edge, leading to a nose-down pitching moment which serves to reduce wing incidence. At some point the flow will reattach and the nose-down moment dissipates. The stored elastic energy within the wing then returns the wing to an elevated AoA and the SITES process is repeated in a cyclic fashion.

Rokoni found that the interaction of shocks formed from transonic flow over a supercritical airfoil with the boundary layer lead to self-sustained shock oscillations and lift fluctuations which results in the initiation of the buffeting phenomenon [26]. Reynolds-averaged Navier Stokes (RANS) equations were utilized to account for the

strong viscous-inviscid boundary layer interaction behind the shock. This method was used to predict buffet onset and was validated with experimental data.

Cunningham, an advocate of SITES LCO, has suggested that SITES is the non-linear spring which triggers and drives LCO. Cunningham observed that the appearance of SITES coincides with the classical trailing edge divergence, a well-established indicator of buffet onset [6]. The role of SITES in LCO was developed in response to the observation that bending mode responses were very well predicted whereas torsion mode responses were consistently underpredicted. The alternating transition from SITES to attached flow could couple with wing torsional motion and low damping, resulting in LCO.

An analysis by Meijer and Cunningham has shown indications that at transonic speeds, SITES plays a dominant role in the development of LCO on a fighter type aircraft [21]. They utilized steady wind tunnel data to develop a LCO prediction method. The method was used to correctly identify several configurations known to encounter LCO. While this semi-empirical technique requires wind-tunnel data for the airframe of interest, their results have the potential to identify aeroelastic instabilities early in the design process of new aircraft.

Due to ease of access and potential for future growth, the majority of the previously mentioned experiments consisted of computational analysis. A study by Tauer [28] combined both computational methods with flight test as part of the Air Force's Test Pilot School (TPS) program. Tauer sought to use the flight test in order to 1) validate computational methods for use by AFSEO and 2) to identify nonlinear sources of LCO on the F-16 with particular interest in SITES. The flight test used tufting and shadowgraph techniques to conduct in-flight flow visualization. From his flight test, Tauer observed the following:

1. The presence of shocks did not result in any noticeable separation on the tufts.
2. Shock waves did not move in response to the pitching and plunging of the wing during LCO.

The movement of shocks on the wing was non-periodic and correlated to changes in flight conditions. For the smaller amplitude LCO experienced during Tauer’s flight test, it appears that some aerodynamic nonlinearity other than SITES is the culprit behind F-16 LCO. Tauer suggested that further analysis of the complex aerodynamics of the underwing with stores may provide insight to the development and sustainment of LCO.

2.3.3 Nonlinear Structural Damping. Within the transonic regime, it is understandable to hypothesize the influence of SITES in LCO characteristics. Despite the plausibility of this hypothesis, LCO is not a phenomenon restricted to transonic flight. A study by Mignolet, Liu, and Chen [23] indicated that a nonlinear transonic aerodynamic model cannot wholly represent the mechanism for wing and store LCO. Rather, a nonlinear structural damping (NSD) model based on Coulomb friction, possibly compounded with nonlinear aerodynamics, would more accurately represent LCO across more of the flight regime instead of just the transonic regime.

NSD can also help to explain why some wind-tunnel tests experience flutter while the matching flight test resulted in LCO. While the aerodynamics should be similar due to matched Reynolds number, the wind tunnel models are constructed of far fewer pieces and components than the full-scale aircraft. The reduced model complexity could result in changes to the NSD which could explain the variation between the wind tunnel test and flight test. A final argument made by Mignolet, Liu, and Chen in support of NSD questions why previous flight tests of four identical F-16s found variations in LCO onset speeds and amplitudes for each aircraft. While the aerodynamics of each aircraft should be the same, unique variations in the structural integrity based on wear patterns from years of use could explain the differences in LCO for each aircraft [23].

Chen has proposed that wing/store LCO is a post-flutter phenomenon which occurs when the flutter mode contains low unstable damping which is identified as a hump mode [5]. Chen goes on to say that the aircraft structure usually contains

structural nonlinearity such as friction damping. This amplitude-dependent friction damping can limit the growth of the oscillation amplitude resulting in a limited amplitude steady state oscillation. On the other hand, a typical flutter mode results in amplitude growth largely due to destabilizing negative aerodynamic damping, hence a drastic increase in the damping past the neutral stability point. Chen used his own flutter analysis technique, the g-method, to provide further evidence for NSD by showing a good correlation between the LCO/flutter prediction and the flutter test of the F-16 MA41 and MA43 models [5].

2.3.4 Computational Analysis of LCO. Within the past decades, the use of CFD has become more prevalent in the design and testing of aerospace structures. The use of CFD has also extended into the realm of both steady and unsteady aeroelastic analysis, to include the investigation of flutter and LCO. An aeroelastic study by Nikbay [24] performed both static and dynamic analysis of the HIRENASD wing based on NASA's reference data to investigate steady and unsteady aeroelastic responses in the transonic regime for low and high Reynolds numbers. The study used the ZEUS Euler solver, the same solver used in the present study.

Nikbay found the ZEUS Euler solver with boundary layer coupling showed some agreement with experimental results and a N-S solver. Due to lower fidelity modeling of viscous effects, ZEUS overpredicted the shock pressure magnitude, pressure change across the shock and aftward relocation of the shock on the upper surface for the steady case. For the unsteady case, the Euler solution predicts a more aggressive dynamic response which occurs further aft than both the RANS solution and experimental results. In general, the Euler solution results agree better with the experimental data sets near the mid-span locations where the effects of the wind tunnel wall boundary layers and wing tip vortices were not as prevalent.

In a vein similar to LCO, shock wave interactions with a separated boundary layer are associated with many unsteady phenomena. For aircraft in flight, flow-induced vibrations known as buffeting can occur when separation of the boundary

layer occurs. The shock induced fluctuations are often coupled with self-sustained periodic shock motion of varying amplitude, although the mechanisms responsible for the oscillatory motion are not yet fully understood. What is unique about the shock-boundary layer oscillation is that they do not require oscillatory motion of the wing to occur or perpetuate.

Work by Hashimoto et. al. [17] investigated the effects of turbulence modeling and grid resolution to improve 3-D buffet prediction accuracy with a N-S code. Hashimoto compared two Zonal Detached Eddy Simulations (ZDES) with the Spalart-Allmaras (SA) and Menter's Shear Stress Transport (SST) models. With the SST model, the shock wave location moved downstream to closely match experimental results, but the shock oscillated widely with a large pressure fluctuation behind the shock. Next, Hashimoto implemented a wall model with ZDES while reducing the number of cells by one-third in order to reduce the computational time required for unsteady simulation. ZDES with the wall model predicted shock wave location and the power spectral density of pressure close to the experiment and in general was able to predict the 3-D buffet reasonably well. As seen by this study, turbulence modeling plays a significant role in N-S codes when predicting transonic shock oscillations due to flow separation.

An alternative to a N-S solution is a boundary layer coupling method. In essence, the procedure involves coupling an outer inviscid region with a inner viscous boundary layer. The coupling method is based on the observation that for transonic flow the unsteady flowfield can be characterized by oscillating shocks and separating and reattaching boundaries. The coupled boundary layer method regards such flow as a simulation of two dynamic systems, the outer inviscid flow and inner viscous boundary, whose coupling requires proper convergence to ensure the coupling error between the two distinct flows is minimized. An in-depth description of this coupling process, called the Edwards method, can be found in the next chapter.

Edwards [14] used his method to compute the buffet properties for an 18% thick circular arc airfoil for $Re = 10E6$ and at $M = 0.76$. The calculated periodic shock frequency agreed closely with the experimental value. Additionally, the coupled boundary layer method was also able to compute the hysteresis effect due to increasing or decreasing Mach number on the onset and quenching of periodic motion quite accurately. For increasing Mach, periodic motion occurs at $M = 0.75$ compared to 0.76 experimentally while for decreasing Mach, periodic motion quenched at $M = 0.735$ compared to $M = 0.73$ experimentally. The increasing Mach number results were more accurate for Edwards method than those obtained by way of a N-S code, although the N-S code did more accurately predict the quenching boundary.

2.4 Current AFSEO Methodology

One of the most problematic conditions with performing LCO analysis is the tremendous volume of analysis cases that must be examined in order to provide certification for a given store configuration and its permutations [12, p. 887]. The ever-increasing cost of flight test compounded with the rapid proliferation of possible flight configurations of an aircraft has led to a considerable growth of AFSEO's work to clear new weapons and configurations. While typical flutter and LCO analysis only gives an indication of potential flight characteristics, flight test of the most critical configurations is conducted to determine the true LCO characteristics in order to verify the computational analyses.

Computational fluid dynamics (CFD) has become a powerful and accurate tool for aerodynamic analysis and design. Despite the potential of CFD to provide flow solutions for high fidelity full-scale numerical simulations, its ability to efficiently conduct aeroelastic analysis falls short. In order to reliably simulate aerodynamic flow and the associated nonlinear phenomena with the aircraft model requires a significant amount of time. A recent study by Tang showed that using CFL3D required 4 days of computation to complete a transonic LCO study on a 1 GHz computer of 2-D flow over

an airfoil [27]. Although powerful, the implementation of unsteady CFD to conduct the massive number of aircraft/store configurations for AFSEO is impractical.

AFSEO conducts bulk screening with lower fidelity models to identify flutter-critical or LCO-critical configurations to offset the high cost of flight test [11, p. 500]. This computational approach to flutter/LCO testing is intended to determine potentially dangerous configurations without the need for testing as well as identify configurations whose response characteristics are acceptable, thus eliminating the need for redundant flight testing [12, p. 887-888]. Given the scope of the problem and available computational resources, AFSEO's bulk simulations use MSC.NASTRAN's version of the K-method that includes a low-fidelity aerodynamic model. The F-16 aerodynamic model consists of only 13 panels split into 616 boxes. Aerodynamic modeling of the underwing stores is not included [11, p. 502]. While the aerodynamic model is low fidelity, the F-16 FEM model is the same fidelity as used with other F-16 aeroelastic simulations.

2.5 Straked Delta Wing Wind Tunnel Experiment by Cunningham

Steady and unsteady low speed wing tunnel tests were conducted in 1986 on a pitching simple straked wing model representative of modern fighter aircraft [1,9]. The model was oscillated in pitch at amplitudes sufficient to represent rapid pitch-ups and push-overs at dynamically scaled full scale maneuver times. The tests were used to show how wing and strake vortices develop and interact as well as how they break down and collapse to fully stalled flow. There was interest to extend this understanding to include compressibility effects as well as analysis of LCO flow conditions.

In 1991, Cunningham conducted a combined wind tunnel test using a common instrumented wing panel to investigate configurations at typical LCO flow conditions, and unsteady pressures and forces for a simple straked wing in flow that ranged from incompressible to transonic [7]. The simple straked wing portion of the test had the objective to extend the understanding of flow fields at low speeds and high incidences

up to transonic speeds and high incidences. The LCO portion of the test had the objective of providing information that could be used to help develop a prediction method for full scale LCO characteristics of elastic aircraft.

The wing test was conducted in the NLR (National Aerospace Laboratory) 2.0 x 1.6 m^2 high-speed wind tunnel located in Amsterdam. A sidewall mount was used to secure the semispan model for a range of Mach numbers spanning from $M = 0.225$ to $M = 0.90$. A hydraulic actuator was connected to the turntable which supported the wing balance beam was used to provide oscillatory pitching of the wing. The semispan model was constructed of an aluminum alloy so as to minimize inertial loads. The simple wing/strake (SiS) configuration is shown in Figures 2.2 and 2.3. The outer wing section was a linearly lofted NACA 64A204 with -3° of washout at the wingtip. The strake section was attached to the outer wing so that the entire wing oscillated as a single piece.

The model instrumentation included pressure transducers to measure the unsteady pressure coefficient on the wing. Individual pressure ports were located along pressure measurement sections placed both spanwise and chordwise along the wing. Placement of pressure sections can be found on Fig. 2.2. The pressure sections consisted of 4 chordwise sections and 3 spanwise sections located on the outer wing. Grouping of pressure transducers toward the wingtip was done to concentrate instrumentation in the regions of known shock induced separation.

The SiS model was tested at three Mach numbers: $M = 0.225$, 0.6, and 0.9, all of which were tested at a Reynolds number of $8 * 10^6$, based on the root chord. The wing was then swept from 6° to 48° of mean incidence with an oscillation amplitude of 0.5° to 8° at frequencies varying from 5.7 Hz to 15.2 Hz. A sample of the test matrix used by Cunningham can be found in Fig. 2.4. A similar test matrix was used by the author so that the computational results presented in this thesis could be compared to the original wind tunnel tests by Cunningham.

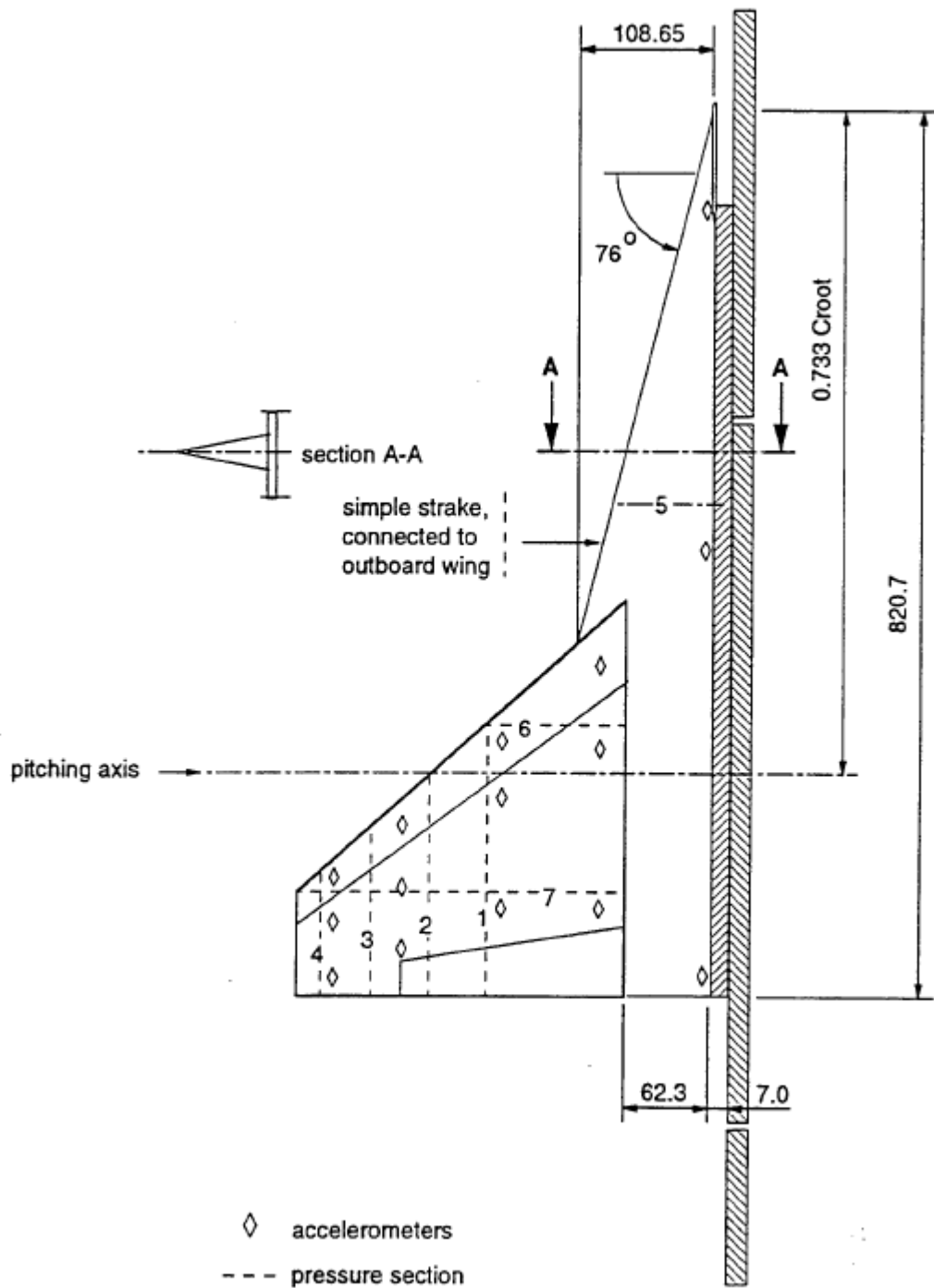


Figure 2.2: Simple Wing/Strake Configuration. Pressure sensors are located along the dotted lines labeled 1-4. (dimensions in mm) [8]

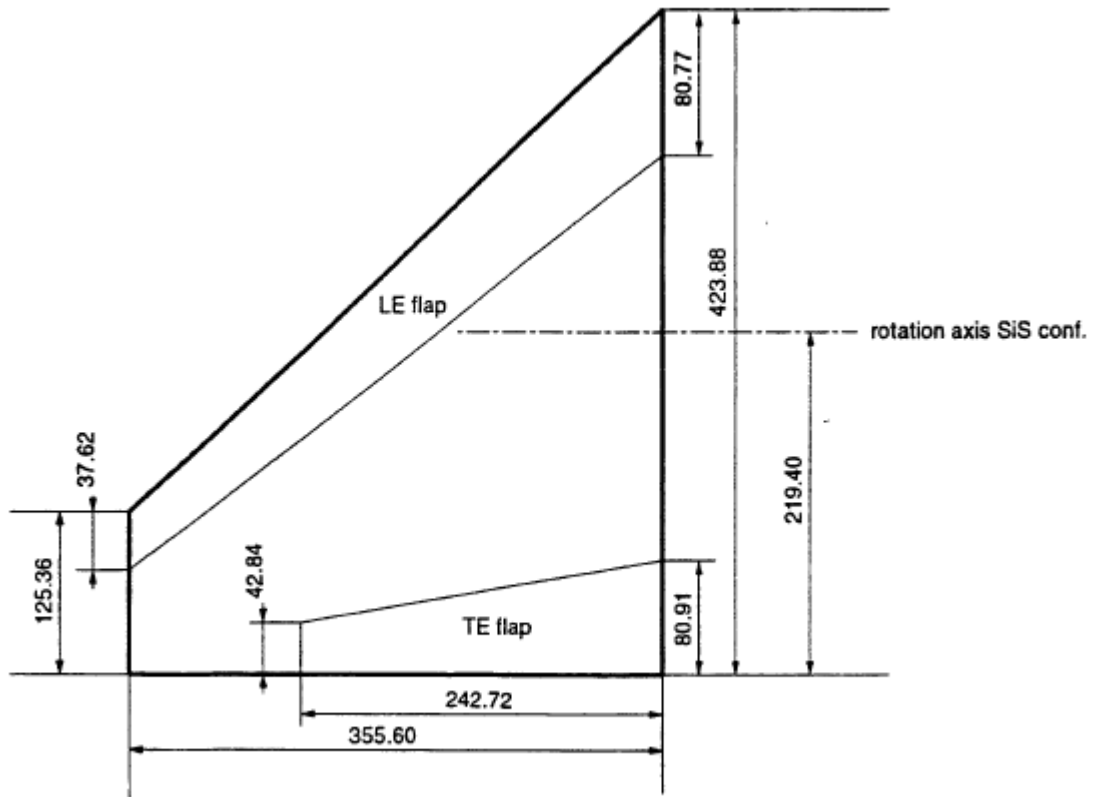


Figure 2.3: Dimensions of wing panel (dimensions in mm) [8]. The computational model used in this study is slightly different than the model presented here.

Mach	0.900								
Re*10 ⁻⁶	= 8.0								= 14.0
freq.	5.7			7.6			11.4	15.2	5.7
alpha	0.5	4.0	8.0	2.0	4.0	8.0	2.0	2.0	0.5
alpha									
4.0	499								527
5.0	500								528
6.0	501	566	574	584	592	601	609	617	529
7.0	502								530
8.0	503								531
9.0	504								533
10.0	505	567	575	585	593	602	610	618	534
10.5									535
11.0	506								536
11.5									537
12.0	507								538
12.5									539
13.0	508								540
14.0	509	568	576	586	594 595	603	611	619	541
15.0	510								542
16.0	511								543
17.0	512								544
18.0	513	569	579	587	596	604	612	620	545
19.0	514								548
20.0	515								547
21.0	516								549
22.0	517	570	580	588	597	605	613	621	526 550
23.0	518								551
24.0	519	565		583	591	600	608	616	
25.0	520								553
26.0	521	571	581	589	598	606	614	622	554
27.0	522								555
28.0	523								556
29.0	524								557
30.0	525	572	582	590	599	607	615	623	558
32.0	559								
34.0	560								
36.0	561								
38.0	562								
40.0	563								
42.0	564								
44.0									
46.0									
48.0									

Figure 2.4: An example of a test matrix used in Cunningham's experiment. [8]

2.6 Chapter Summary

Within the scope of this literature review, the author has covered the foundation and relevant research pertaining to LCO theory. An introduction covering the linear dynamic unstable aeroelastic response known as flutter explains the transition to the nonlinear response of LCO. Possible sources of LCO such as store aerodynamics, SITES and structural damping were investigated in detail to provide some speculation to the cause of LCO. Current AFSEO flutter/LCO methodology was explained next in order to define the motivation behind alternative computational methods for LCO prediction. Finally, Cunningham's 1994 Wind Tunnel experiment, which was the basis for the computational study conducted within this investigation, was reviewed.

III. Methodology

3.1 Introduction

This study performed a series of time-accurate analyses of a wing oscillated in pitch with a commercial Euler code in order to gather data on potential shock migration on the wing. All aeroelastic analysis were carried out with Zona Technologies' ZEUS software. ZEUS is a commercial Euler Unsteady Aerodynamic Solver which involves an automated mesh generation scheme while using a stationary Cartesian grid and implements a boundary layer coupling scheme. ZEUS uses a central difference with JST (Jameson-Schmidt-Turkel) Artificial Dissipation Scheme for flux construction and Green's Integral Boundary Layer Method to model turbulence. This chapter discusses the Euler method employed and the parameters unique to this study.

3.2 ZEUS

3.2.1 Mesh Generation and Finite Element Model. ZEUS utilizes an automated mesh generation scheme that requires the surface mesh of the lifting surfaces and bodies as input. The automated mesh generation is accomplished by creating a block around the model which defines the outermost boundaries of the three dimensional Cartesian mesh. For the purpose of defining the mesh orientation, the origin is located on the root chord with the x, y, and z axis defined as out the tail, laterally out the right wing, and vertically out the top of the aircraft, respectively. The surface grid lines run orthogonally in the X-Y and Y-Z planes. ZEUS then activates a segregation technique that divides the various lifting surfaces into several spanwise zones, called Y-zones. Each aircraft component is projected onto the X-Y plane into individual Y-zones. Within each Y-zone, the leading and trailing edge is extended upstream and downstream, respectively, with the slope of each additional line decreasing so that the final line is parallel to the upstream and downstream X-Y boundary.

A cubic spline technique then extends each line in the Y direction based on the following constraints: the slope of adjoining cells must match and the line must be perpendicular to the X-Z plane at the farfield boundary in the Y direction. The

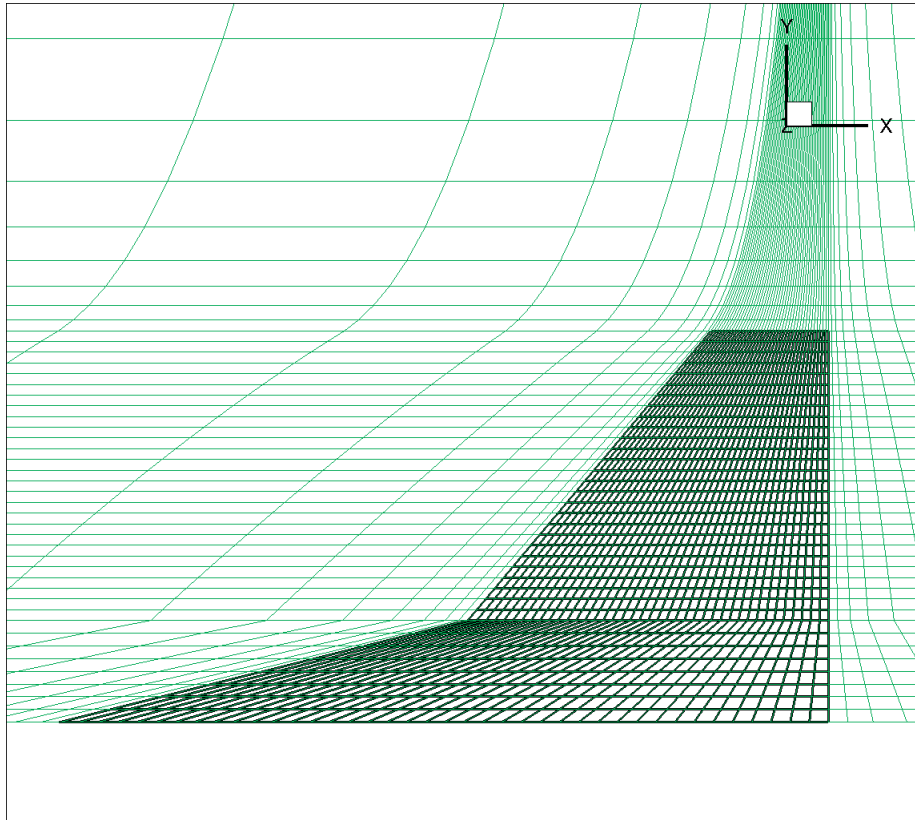


Figure 3.1: Mesh Generation, Top View, Close. XY plane view of the computational mesh.

Y-zones allow for ZEUS to build an automated sheared mesh by growing the gridlines from the surface mesh to the outer boundary of the block based on a user defined cell growth rate [32, p. 5-5]. A top-down view of the mesh can be seen in Figures 3.1 and 3.2.

The mesh boundaries were extended two chord lengths upstream, five chord lengths downstream, two spanwidths from the X-Z plane, and a chord length above and below the X-Y plane. The generated mesh can be found in Figures 3.3 and 3.4.

Although various finite element method (FEM) models for the F-16 exist, Cunningham's experiment did not seek to replicate mass/inertial properties of the model wing to a full scale wing. The wing was constructed of aluminum to reduce inertial loads. Impact testing was conducted on the model to determine natural frequencies and vibration modes. The results of these tests allowed for the selection of oscillation

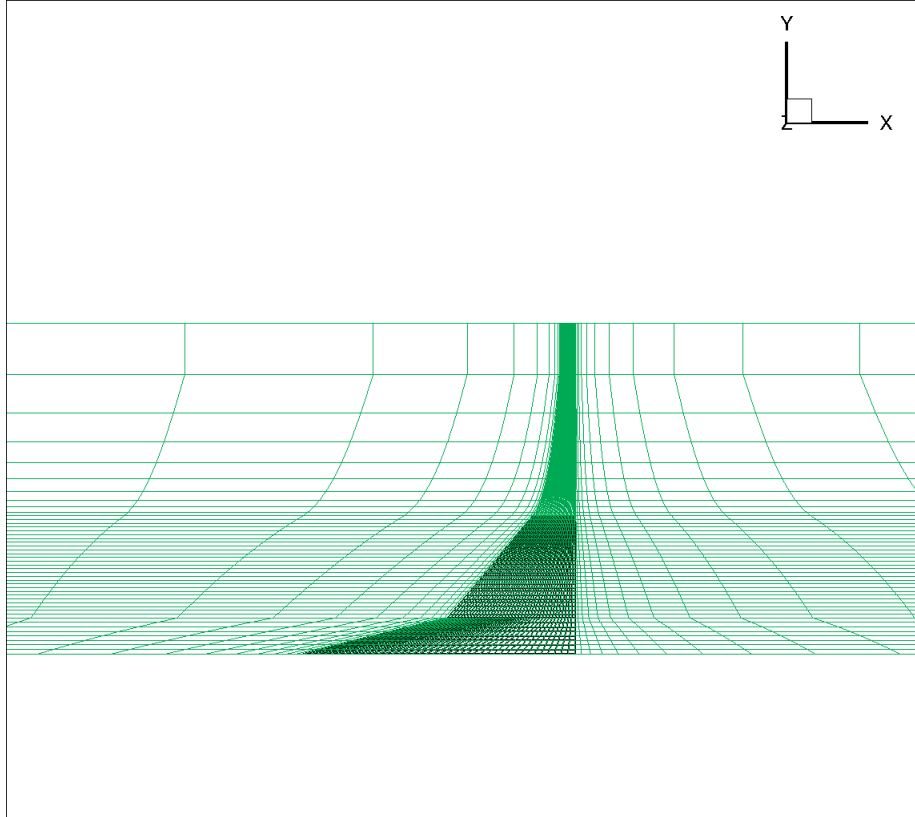


Figure 3.2: Mesh Generation, Top View, Full. XY plane view of the computational mesh.

frequencies that were not close to the natural frequencies of the model. For harmonic excitation frequencies below 8 Hz, the model was considered rigid. For this reason, it was decided to implement a rigid body computational model with only a rotational pitch mode.

A "dummy" file was used to define the FEM model which contained a single point located along the strake root at $x = 0.733 * C_{root}$. The single point had one eigenvector which defined rotational pitch mode. All of the aerodynamic panels were then splined to the single FEM point which resulted in rigid body rotational motion of the entire computational model. The entire strake-outboard wing structure was then converted to a control surface with a rotation axis located in the same position as that of the Cunningham model. Treating the entire wing structure as a control surface

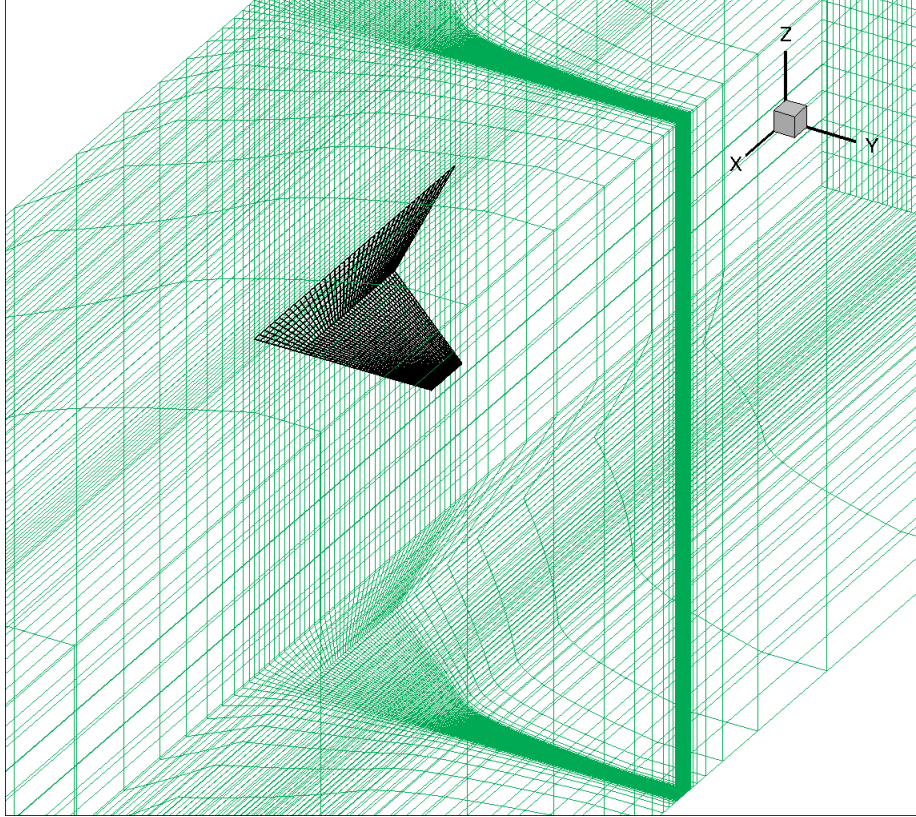


Figure 3.3: Mesh Generation, Close View. ZEUS uses a built-in, automated mesh generation scheme to extrapolate a 3-D mesh from the 2-D panel distribution along the wing's surface.

allowed for direct control of the wing's orientation so that LCO could be simulated by providing input to the wing to oscillate at a prescribed amplitude and frequency.

ZEUS can run both a full or linearized Euler solver. While ZONA recommends use of the linearized solver when possible, this recommendation applies more-so to small amplitude disturbances. Due to the nonlinear nature of the LCO simulations, high angles of attack, and large oscillation amplitudes, the full Euler solver was utilized. ZEUS' implementation of the Euler solver will be described in a later section.

3.2.2 Unsteady Euler Solver on Stationary Cartesian Grid. ZEUS generates unsteady aerodynamics based on a stationary Cartesian grid. ZEUS solves the time-accurate Euler equations by way of a cell-centered central-differencing finite-

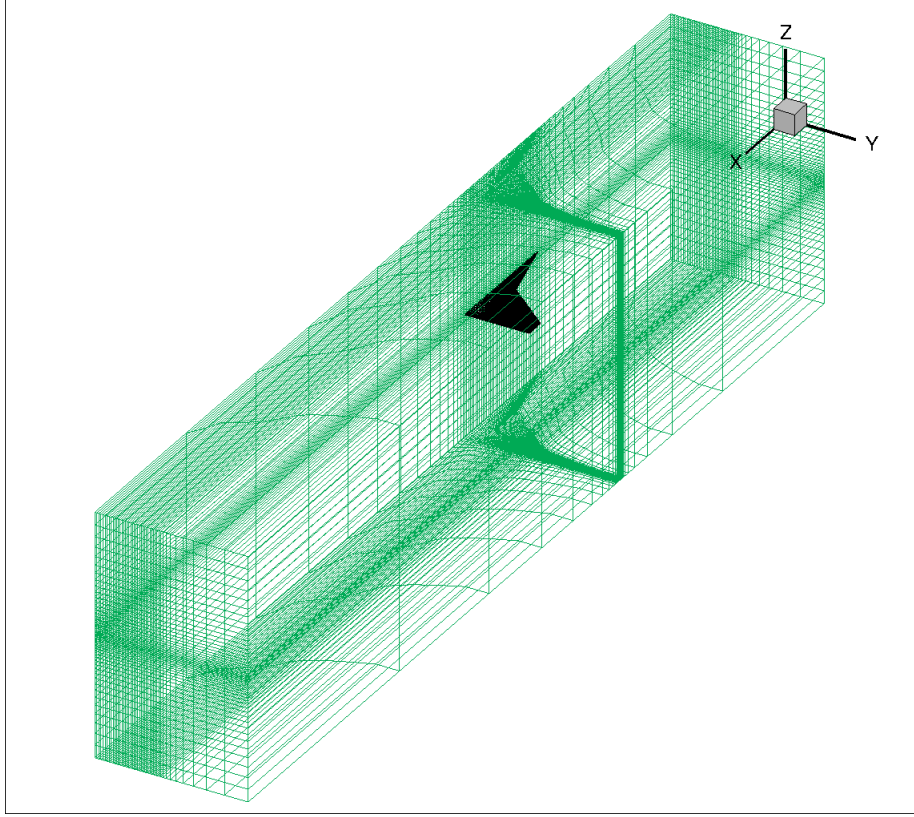


Figure 3.4: Mesh Generation, Full View. ZEUS uses a built-in, automated mesh generation scheme to extrapolate a 3-D mesh from the 2-D panel distribution along the wing's surface.

volume method with Jameson-Schmidt-Turkel (JST) artificial dissipation scheme implemented for the stability of the flow solver [32, 6.1].

3.2.3 Time-Accurate Euler Method. The three-dimensional Euler equations in conservative differential form and in curvilinear coordinates are as follows:

$$\frac{\partial Q}{\partial t} + \frac{\partial H_1}{\partial \xi} + \frac{\partial H_2}{\partial \eta} + \frac{\partial H_3}{\partial \zeta} = 0 \quad (3.1)$$

where Q is the product of conservative flow variables vector \mathbf{q} and the inverse of the transformation Jacobian \mathbf{J} , and H_i are the convective fluxes in three curvilinear

coordinate directions:

$$\begin{aligned}
 Q = Jq = J \begin{bmatrix} \rho \\ \rho u \\ \rho v \\ \rho w \\ e \end{bmatrix} & \quad H_1 = J \begin{bmatrix} \rho U \\ \rho u U + p\xi_x \\ \rho v U + p\xi_y \\ \rho w U + p\xi_z \\ (e + p)U - p\xi_t \end{bmatrix} \\
 H_2 = J \begin{bmatrix} \rho V \\ \rho u V + p\eta_x \\ \rho v V + p\eta_y \\ \rho w V + p\eta_z \\ (e + p)V - p\eta_t \end{bmatrix} & \quad H_3 = J \begin{bmatrix} \rho W \\ \rho u W + p\zeta_x \\ \rho v W + p\zeta_y \\ \rho w W + p\zeta_z \\ (e + p)W - p\zeta_t \end{bmatrix}
 \end{aligned} \tag{3.2}$$

U, V, W and u, v, w are the three components of the flow velocity in curvilinear and Cartesian coordinates, respectively, and are related by the following metric terms:

$$\begin{aligned}
 U &= \xi_i \cdot \langle u, v, w \rangle + \xi_t \\
 V &= \eta_i \cdot \langle u, v, w \rangle + \eta_t \\
 W &= \zeta_i \cdot \langle u, v, w \rangle + \zeta_t
 \end{aligned} \tag{3.3}$$

The gas is assumed to be perfect and the equation of state is:

$$e = \frac{1}{\gamma - 1} p + \frac{1}{2} \rho (u^2 + v^2 + w^2) \tag{3.4}$$

Applying Equation (3.1) to each finite-volume grid cell results in a set of ordinary differential equations of the form:

$$\frac{d}{dt} (q_{i,j,k} \Omega_{i,j,k}) + R(q_{i,j,k}) = 0 \tag{3.5}$$

where $\Omega_{i,j,k}$ is the volume of the cell with index (i,j,k) and the residual $R(q_{i,j,k})$ is obtained by evaluating the flux integral at all the cell surfaces and summing them up.

Jameson's artificial dissipation flux is added to the convective flux for stability:

$$R(q_{i,j,k}) - C_{i,j,k} - D_{i,j,k} = C_{i,j,k} - (D_{i,j,k}^{(2)} - D_{i,j,k}^{(4)}) \quad (3.6)$$

C and D are the flux integrals of the cell due to convective flux and artificial dissipation flux, respectively, while $D^{(2)}$ and $D^{(4)}$ are the 2nd and 4th order artificial dissipation fluxes. Both artificial dissipation fluxes are the sum of the artificial dissipation at all six surfaces of the computational cell. The 2nd and 4th order dissipative terms are defined as:

$$\begin{aligned} \epsilon_{(i+\frac{1}{2},j,k)}^{(2)} &= \kappa^{(2)} \min [0.25, \max(\nu_{i+1,j,k}, \nu_{i,j,k})] \\ \epsilon_{(i+\frac{1}{2},j,k)}^{(4)} &= \max \left[0, \frac{\kappa^{(4)}}{32} - \epsilon_{i+\frac{1}{2},j,k}^{(2)} \right] \end{aligned} \quad (3.7)$$

here $\kappa^{(2)}$ and $\kappa^{(4)}$ are the two parameters VIS2 and VIS4, respectively, found in the MKPARAM bulk data card used to control the amount of artificial dissipation present in the Euler solver for stability. The pressure sensor $\nu_{i,j,k}$ is defined as:

$$\nu_{i,j,k} = \left| \frac{p_{i-1,j,k} - 2p_{i,j,k} + p_{i+1,j,k}}{p_{i-1,j,k} + 2p_{i,j,k} + p_{i+1,j,k}} \right| \quad (3.8)$$

The pressure sensor serves as a switch to toggle the effects of the artificial dissipation. In the region close to the shock wave, the pressure has to jump and the value of $\epsilon^{(2)}$ is of order one which turns on the 2nd order dissipation and disables the 4th order dissipation. Alternatively, in an area with a smooth pressure region, the 2nd order term is turned off and the 4th order dissipation works to damp the high frequencies that the central-differencing scheme fails to damp.

For the time accurate solution, the $\frac{d}{dt}$ operator from Equation 3.5 is approximated by an second-order, implicit backward difference method of the following form:

$$\frac{3}{2\Delta t} [q^{n+1}\Omega^{n+1}] - \frac{2}{\Delta t} [q^n\Omega^n] + \frac{1}{2\Delta t} [q^{n-1}\Omega^{n-1}] + R(q^{n+1}) = 0 \quad (3.9)$$

The equation above can be formed into a steady-state problem with the pseudo time t^* :

$$\frac{d(q^{n+1}\Omega^{n+1})}{dt^*} + R^*(q^{n+1}) = 0 \quad (3.10)$$

where

$$R^*(q^{n+1}) = \frac{3}{2\Delta t} (q^{n+1}\Omega^{n+1}) - \frac{2}{\Delta t} (q^n\Omega^n) + \frac{1}{2\Delta t} (q^{n-1}\Omega^{n-1}) + R(q^{n+1}) \quad (3.11)$$

A five-stage Runge-Kutta (R-K) pseudo-time marching scheme can be applied to Equation 3.10. A dual-time stepping method is used for the solution of the time-accurate Euler equations due to the two different time-steps, Δt and Δt^* . The five-stage R-K pseudo-time marching method is an explicit scheme which limits the pseudo-time step size Δt^* to ensure numerical stability. ZEUS uses the Courant-Friedrichs-Lewy (CFL) number to control the size of the time step. The coefficients of the five-stage R-K scheme are chosen such that an optimal CFL number of about 4.0 without residual smoothing can be achieved. If residual smoothing is applied, the maximum attainable value for CFL is pushed up to 8.0. For most practical purposes, ZEUS should be able to use the CFL number of 7.0 for most cases with residual smoothing turned on [32, 6.1].

Due to the implicit method used for the physical time step, the dual-time stepping method in ZEUS has no limitations on the stability for the physical time step. Therefore, the physical time step should be driven by the flow physics. The ZEUS manual recommends at least 50 physical time steps within a sinusoidal excitation.

ZEUS incorporates a variable-coefficient implicit residual smoothing scheme to further increase the stability range of the Euler solver. In the case of a 2D flow field, the residual smoothing formula is as follows:

$$(1 - \beta_\xi \nabla_\xi \Delta_\xi)(1 - \beta_\eta \nabla_\eta \Delta_\eta) \bar{R}_{i,j} \equiv R_{i,j} \quad (3.12)$$

where $R_{i,j}$ and $\bar{R}_{i,j}$ are the residuals before and after smoothing. $\nabla\Delta$ is the standard second-difference operator and β is the residual smoothing coefficient. The value of β can be either a constant or a function of the local spectral radii.

3.2.4 Transpiration Boundary Conditions. For complex configurations, the generation of a body-fitted grid could be a daunting task. Additionally, the use of deforming mesh can cause problems such as grid cross-over or over-skewed mesh when performing unsteady simulations. In order to bypass these issues, ZEUS uses a stationary Cartesian grid by utilizing the transpiration boundary conditions to account for both thickness and small amplitude motion of the wing surface. Due to the stationary grid, all time-derivative based terms from Equations 3.2 such as ξ , η and ζ are dropped.

A thin wing with slight deformation about its mean position (horizontal plane, $z = 0$) is then considered. The shape of the upper and lower surfaces of the wing are defined as $z = f(x, y)$ and $g(x, y)$, respectively and the instantaneous position for the upper and lower surfaces are described by $z = F(t, x, y)$ and $G(t, x, y)$. Assuming $\|F\| \ll 1$, the surface velocity boundary condition on the upper surface of the wing at time t can be found with the first order approximation:

$$w(t, x, y, 0^+) = u(t, x, y, 0^+)F_x + v(t, x, y, 0^+)F_y + F_t + O(F) \quad (3.13)$$

The subscripts x , y and t indicate partial derivatives; $O(F)$ represents terms with the same order of magnitude as F or higher. The normal velocity boundary condition on the lower surface is treated in a similar fashion.

The normal momentum equation is used to derive the boundary condition for pressure:

$$\vec{n} \cdot \left[\frac{\partial \vec{V}}{\partial t} + (\vec{V} \cdot \nabla) \vec{V} \right] = \vec{n} \cdot \left(-\frac{\nabla p}{\rho} \right) \quad (3.14)$$

where \vec{V} is the flow velocity and \vec{n} is the unit normal at the wing surface. The pressure gradient in the normal direction can be derived from the previous equation for the

upper surface of the wing.

$$\begin{aligned}
 p_z(t, x, y, 0^+) &= p_x(t, x, y, 0^+)F_x + p_y(t, x, y, 0^+)F_y - \\
 \rho(F_{tt} + 2F_{tx}u + 2F_{ty}v + 2F_{xy}uv + F_{xx}u^2 + F_{yy}v^2) &+ O(F)
 \end{aligned}
 \tag{3.15}$$

Further details regarding the application of a stationary Cartesian grid to this Euler unsteady method can be found in Zhang [31].

3.2.5 Boundary Layer Coupling. In order to circumvent the need to develop a complex RANS solver for a Cartesian grid, ZEUS provides a boundary layer coupling scheme which accounts for the viscous effects associated with aerodynamic flows of general concern. When considering flows with relatively high Reynolds number in the millions, the boundary layer is confined to a thin space along the surface. This assumption allows the flow to be partitioned into two zones: a viscous boundary layer while the rest of the flow can be treated as inviscid. For the solution of the boundary layer, an integral method or finite difference method are available. Due to the complexity and uncertainties associated with accurately modeling turbulence with a finite difference method, an integral boundary layer method was chosen to be coupled with the ZEUS (Euler) solver.

3.2.6 Integral Boundary Layer Method. The integral boundary layer method is applied in a 2-D quasi-steady manner; the boundary layer parameters are solved independently at each physical time step in the freestream x direction and then coupled with the inviscid Euler flow solution for each individual strip in the y direction. The quantities of the integral boundary layer are governed by the following set of ordinary differential equations:

$$\begin{aligned}
 \frac{dU_e^v}{dx} &= F_1 + F_2 \frac{1}{\bar{m}} \frac{d\bar{m}}{dx} \\
 \frac{d\bar{H}}{dx} &= F_3 + F_4 \frac{1}{\bar{m}} \frac{d\bar{m}}{dx} \\
 \frac{dC_E}{dx} &= F_5 + F_6 \frac{dU_e^i}{dx}
 \end{aligned}
 \tag{3.16}$$

where U_e^v is the boundary layer edge velocity, F_i are nonlinear functions of the boundary layer parameters involved, \overline{H} is the shape factor, C_E is the lag entrainment coefficient and U_e^i is the inviscid flow velocity calculated by the Euler solver at the wall where the boundary layer grows. For further details on the derivation of the above equations and definitions of all parameters, please refer to Zhang [31]. The perturbation mass flow parameter, \overline{m} is defined as:

$$\overline{m} = \rho_e U_e \delta^* \quad (3.17)$$

where ρ_e and δ^* are the boundary layer edge density and displacement thickness, respectively.

As Equation 3.16 contains initial unknown flow quantities such as velocity and density at the boundary layer interface, the integral boundary layer solver must couple with the inviscid Euler solver iteratively until the boundary layer interface velocity matches between the integral boundary solver and the Euler solver. An overview of the boundary layer coupling procedure occurs in the following fashion.

1. Obtain the density and edge velocity (U_e^i) at the interface from the Euler solver to approximate the mass flow parameter using the boundary layer thickness from the previous iteration.
2. Solve the boundary layer equations with the assumed mass flow parameter to obtain a new boundary layer edge velocity U_e^v
3. Compare the velocities U_e^v and U_e^i . If the values are within tolerance, the solution has converged. If otherwise, update the boundary layer thickness to use in the next iteration. The method for updating δ^* is described in the next section.

The coupling of the integral boundary layer solver and Euler solver is performed at the end of each Newton sub-iteration. There is no boundary layer coupling convergence control implemented in ZEUS so the guarantee of convergence is left to the user to ensure.

3.2.7 *Boundary Layer Coupling Scheme.* In the final stage of the boundary layer coupling procedure, ZEUS utilizes two different schemes to update the boundary layer thickness, δ^* . The first scheme is called Carter's relaxation scheme [3]:

$$\frac{\delta_{n+1}^*}{\delta_n^*} = 1 + \omega \left(\frac{U_e^v}{U_e^i} - 1 \right) \quad (3.18)$$

where n indicates the step iteration and ω is the relaxation factor.

After the boundary layer thickness is obtained from the integral boundary layer solver at the end of each Newton sub-iteration, the wing surface slope, F_x , is added to the thickness to account for the thickening effect of the boundary layer in the inviscid Euler solution. Carter's scheme converges well and fast for flows with an attached boundary layer or even small separation bubbles but tends to fail for cases with a large separation region.

In an effort to extend the range of application of the integral boundary layer method, Edwards developed a variable gain integral control coupling scheme [14]. Edwards' scheme introduces some limiters and gain control functions to deal with cases with regions of extensive separation:

$$\begin{aligned} \delta_{n+1}^* &= \delta_n^* + XKINT * t_1 * (1.0 + t_1 * t_2) \left(\frac{U_e^v}{U_e^i} - 1 \right) \\ t_1 &= f_1(GAIN1, BRK1, BRK2, \delta^*) \\ t_2 &= f_2(GAIN2, BRK3, BRK4, C_f) \end{aligned} \quad (3.19)$$

where $XKINT$ is the major gain factor, t_1 is a nonlinear gain factor scheduled on δ^* rising from a value of 1.0 for values of δ^* less than $BRK1$ to a value of $GAIN1$ for δ^* greater than $BRK2$, t_2 is another nonlinear gain factor scheduled on the skin friction coefficient C_f falling from a value of 0.0 for C_f greater than $BRK4$ to a value of $GAIN2$ for C_f less than $BRK3$. A more detailed description of Edwards' coupling scheme can be found in [14].

ZEUS uses Edwards scheme by default when viscous effects are taken into account. The ZEUS user's manual recommends using the preset values for the limiters

and gains until the effects of changing those parameters are made clear with additional understanding of the flow.

3.2.8 Time Steps and Loops in ZEUS. As mentioned previously, ZEUS solves the time-accurate Euler equations with a dual-time stepping method which includes a pseudo-time marching loop within the physical time step loop. Within the pseudo-time calculation, ZEUS implements a Newton sub-iteration loop to solve for boundary layer coupling. Figure 3.5 shows each of these loops as they are solved in ZEUS.

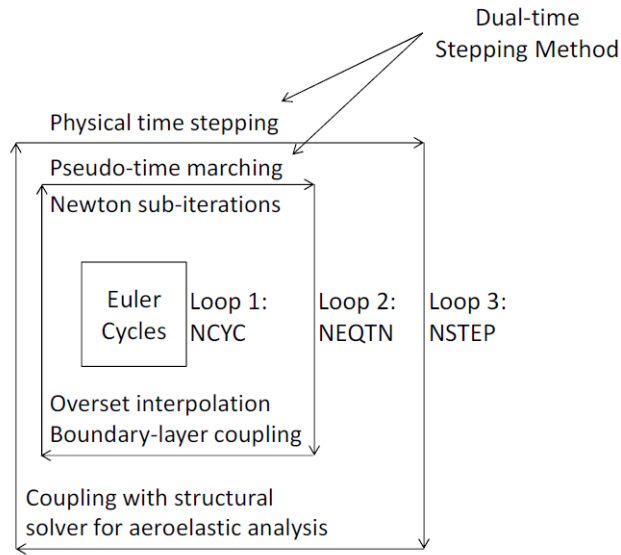


Figure 3.5: Flow Chart of the Euler Solver in ZEUS. NCYC, NEQTN and NSTEP refer to input parameters within ZEUS [32].

The Euler cycle refers to a 5th order R-K pseudo-time marching scheme. The coupling of the Newton sub-iterations within the Euler cycles combine to make the pseudo-time marching iterations to achieve a converged steady flow solution or instantaneous flow solution for each discrete physical time step.

With the exception of CFL, the number of Euler cycles and Newton sub-iterations, all flow parameter inputs described in the previous sections which are required for the ZEUS Euler solver were left at their default values. CFL was run at

a value of 6.0 for all cases except those at a trim of 10° for which CFL was reduced to 0.5 to ensure the solution converged while a physical time step of $0.5\text{E-}3$ was used in the time accurate analysis. The number of Euler cycles was increased to 3 while the Newton sub-iterations was increased to 12 cycles based on a convergence study.

3.3 Computational Model

3.3.1 Matching of Reynolds Number. The Reynolds number was matched to ensure similar flows between the computation test and wind tunnel test. All tests run in the NLR wind tunnel were performed at a Reynolds number of $8 * 10^6$ based on the root chord. The wind tunnel has the capability to adjust both temperature and pressure of the incoming flow. Focusing solely on temperature control, the dynamic pressure, which is required for trim analysis in ZEUS, was backed out from the Reynolds number. The process can be seen below. The equations for the Reynolds number, dynamic pressure, and Mach number are defined first.

$$Re = \frac{\rho V L}{\mu} \quad (3.20)$$

$$q_\infty = \frac{1}{2} \rho V^2 \quad (3.21)$$

$$M = \frac{V}{a} \quad (3.22)$$

where:

- ρ is the freestream density
- V is the freestream velocity
- L is the characteristic length (chord length)
- a is the speed of sound

Substituting equation 3.21 into 3.20 results in the following:

$$Re = \left(\frac{1}{2}\rho V^2\right)\left(\frac{2L}{V\mu}\right) = q_\infty\left(\frac{2L}{V\mu}\right) \quad (3.23)$$

Reynolds number can now be redefined by substituting equation 3.22 into equation 3.23.

$$Re = q_\infty \frac{2L}{(Ma)\mu} \quad (3.24)$$

Viscosity can be rewritten as a function of temperature by way of Sutherland's law. Speed of sound and viscosity are now both functions of temperature, resulting in a Reynolds number as a function of temperature. Equation 3.24 can be rewritten to find the unknown dynamic pressure as a function of temperature.

$$q_\infty = \frac{ReM}{2L} a\mu \quad (3.25)$$

$$a = \sqrt{\gamma RT} \quad (3.26)$$

$$\mu = \mu_0 \frac{T_0 + C}{T + C} \left(\frac{T}{T_0}\right)^{1.5} \quad (3.27)$$

where:

- a is the speed of sound
- γ is the ratio of specific heats
- R is the gas constant
- T is the freestream temperature
- μ_0 is the reference viscosity
- T_0 is the reference temperature
- C is Sutherland's constant, $C = 110.4$ K

A standard temperature of 25° C (298 K) was used to find the dynamic pressure based on a set Reynolds number and given Mach number.

3.3.2 Computational Model Design. The computational model was designed with the use of ZEUS. ZEUS takes the users input as a series of leading edge points and chord lengths to define a flat plate in the desired shape. Additional information such as airfoil shape is added onto the flat plate to create the final design as seen in Fig. 3.7. The strake section was built with a diamond shaped cord of 2.5 percent thickness located at 0.85 of the chord length. The strake was then linearly interpolated from the diamond shaped chord at the root to a NACA 64A204 airfoil section, which then connected seamlessly to the outer wing geometry. The outer wing section was entirely a NACA 64A204 airfoil section with 3 degrees of washout at the wing tip (-3° of incidence). The wind tunnel wall used in Cunningham’s test was simulated in ZEUS by defining symmetry along the X-Z plane of the model.

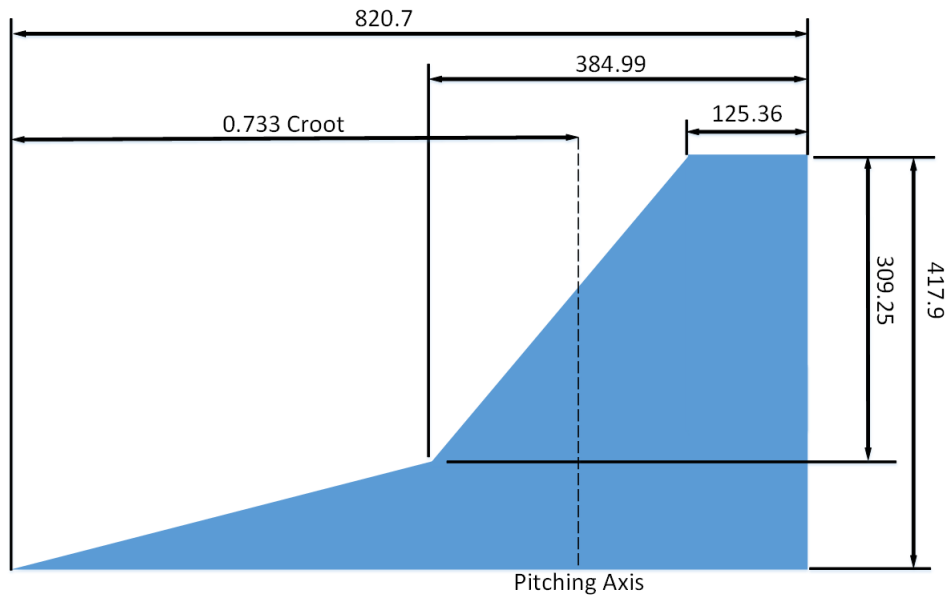


Figure 3.6: Dimensioned Top View of Wing. All dimensions on the drawing are in units of mm. Planform area is equal to 0.144 m². Chord length is 0.8207 m. Span is 0.435.8 m.

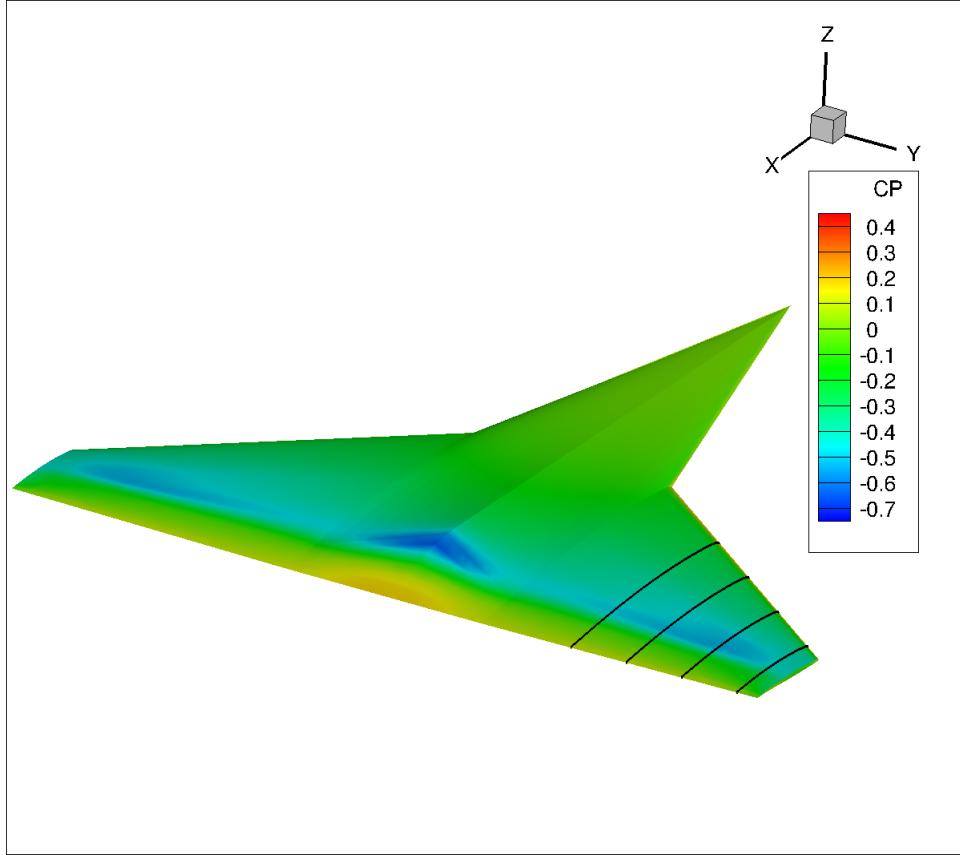


Figure 3.7: 3-D View of the computational SiS model at $\text{AoA} = 4^\circ$. The 4 black lines on the outer wing section indicate the locations along which C_p was evaluated. The locations denote C_{p1} , C_{p2} , C_{p3} and C_{p4} with the following physical locations: $y = 209$ mm, 274 mm, 336 mm and 395 mm from the centerline, respectively. C_{p1} is located most inboard and C_{p4} nearest the right wing tip.

Due to ZEUS specific geometry definitions, the SiS computational model was altered slightly from the wind tunnel model. The total span and chord length remained unchanged but the boundary between the strake and outer wing was pushed out 46.35 mm towards the wingtip. The change in the strake-wing interface location is due to constraints in the ZEUS geometry input. The total planform area of the computational model matches the wind tunnel model. Although the dimensions at the strake-wing intersection are altered slightly, the section of the wing of the most importance is the wingtip, for which the computational model matches the wind tunnel model closely. The 3-D model is not visually "watertight" and this is because

ZEUS uses a flat plate instead of a three dimensional wing with thickness to perform calculations. Once the run is complete, the data from the mesh is then superimposed onto the 3-D wing geometry.

3.3.3 Grid Sensitivity Study. A grid sensitivity study was conducted on the wing model to determine proper grid resolution. A trim case for $N_z = 1g$ was run with multiple wing models of varying grid density. The panels on the wing were created from divisions along the chordwise and spanwise length of the wing. The spanwise and chordwise divisions were linearly distributed so that the distance from one division cut to another in both directions was evenly spaced. Figure 3.8 displays the trim AoA solved by ZEUS for various grid configurations.

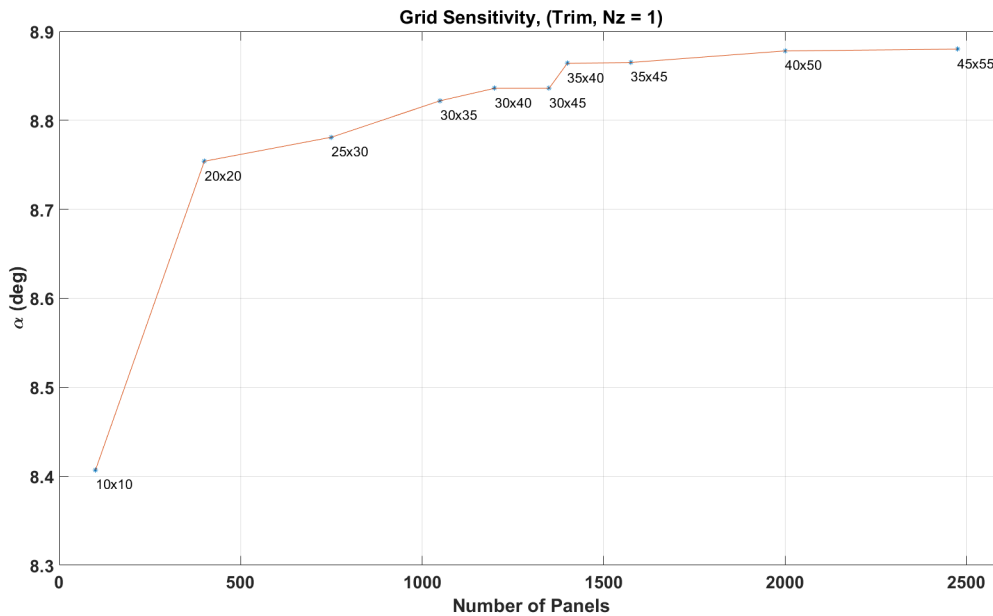


Figure 3.8: Grid Sensitivity. The plot depicts changes in the trim AoA as a function of panel density for a load factor of 1. The label below each point indicates the number of spanwise and chordwise distributions along the wing, respectively.

The final wing design was composed of 35 spanwise and 40 chordwise divisions, which created 1400 aerodynamic panels on the surface of the wing as seen in Fig. 3.9. ZEUS' automated mesh generator used the 2-D panel distribution to extrapolate a

3-D Cartesian computational mesh which was composed of over 83,000 cells. This panel density resulted in a trim AoA within 0.18% of the high panel density solution. For the various runs in Fig. 3.8, computational time was proportional to the number of panels used. For this reason, the lowest possible grid density which still provided an accurate result was used.

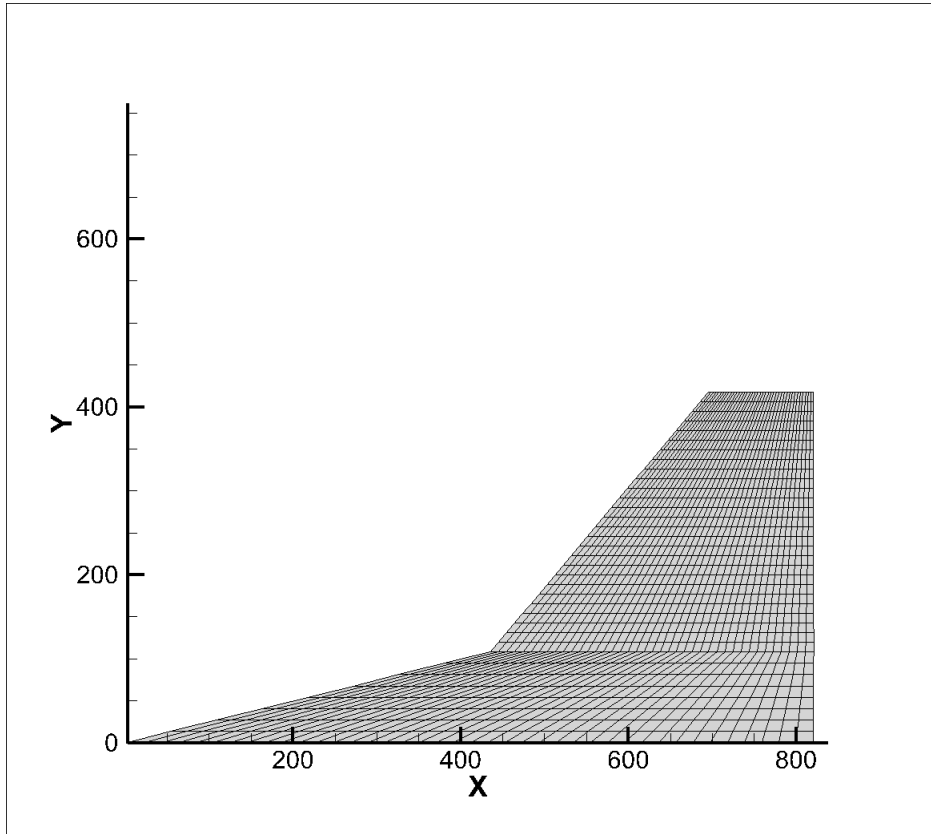


Figure 3.9: Aerodynamic Panels on Wing. 1400 panels were created from a distribution of 41 nodes along the chord and 36 nodes across the span of the Wing.

As seen in Fig. 3.9, the panels on the inboard strake section are highly skewed near the leading edge. Due to the automated mesh generation scheme based on the user defined wing surface panel density, ZEUS does not implement any sort of elliptical smoothing technique to refine the 3-D Cartesian Mesh. While the lack of elliptically smooth cells allows for the rapid generation of the cell mesh for complex aircraft

configurations, this lack of functionality may limit the ability of ZEUS to refine areas of high pressure gradients such as shocks.

3.4 Test Matrix

The SiS model was run for various combinations of Mach number, oscillation frequency, median AoA and oscillation amplitude to determine how these factors influence the migration of shocks when solved using ZEUS. The Mach number was tested at $M = 0.85, 0.90, 0.95$ to cover a range within the transonic region. The oscillation frequency was set to 5.7 Hz and 7.4 Hz. The median AoA (trim) was set at $4^\circ, 7^\circ$ and 10° . Although Cunningham’s report tested at trim angles of up to 30° , such results seem highly unlikely to occur in normal flight. In addition to feasibility, high AoAs will lead to separated flow which ZEUS may have more difficulty resolving. For these reasons, lower trim angles which are more likely to be seen during flight without extensive regions of separation were tested. All tests were oscillated at both $\pm 2^\circ$ and $\pm 4^\circ$. The table below shows the flight condition combinations used to produce a total of 32 unique tests.

Table 3.1: Test Matrix. The SiS model was run for various combinations of Mach, trim, oscillation amplitude and oscillation frequency. x and o indicate an oscillation frequency of 5.7 Hz and 7.4 Hz, respectively. I indicates a fully inviscid test case.

		Trim, (deg)		
		4	7	10
Mach	0.85	x	x	
	0.90	xoI	xoI	xoI
	0.95	xo	xo	x

Additional tests were run at Mach 0.9 with a frequency of 5.7 Hz with the boundary layer coupling turned off to determine the difference between the fully inviscid and boundary layer coupled solution.

3.4.1 Sinusoidal Transient Effects. Cunningham’s experiment rationalized the response to a sinusoidal input would be harmonic, thus the data collected from a

single cycle would be representative of all future cycles. For this reason, all data was collected from a single oscillatory input perturbing the wing from steady state. This method of data collection does not account for transient effects, if any such exist. In the case of the computational model, the wing was oscillated two cycles for which both the time accurate data and frequency domain data were collected from the response from the second cycle. Based on the time domain response, it was clear transient effects were present and ZEUS required a second cycle to reach a more harmonic response.

3.5 Post Processing of Data

For the time-accurate analysis, ZEUS provides pressure data in the form of the pressure coefficient on the wing's surface for each desired time step. While the primary intent of this data is to be viewed as a temporal three dimensional model in Tecplot, the data was additionally converted to a format that could be read into Matlab for further quantitative analysis. The four streamwise locations along the span of the SiS model for which the pressure data was analyzed are the same 4 locations used by Cunningham ($y = 209\text{mm}, 274\text{mm}, 336\text{mm}$ and 395mm).

IV. Results and Analysis

4.1 Introduction

This chapter presents the results from a time-accurate Euler code with boundary layer coupling performed with ZEUS. A cropped delta wing, referred to as the SiS model, with rigid body dynamics was oscillated in pitch along a specified axis of rotation. Pressure coefficient data was collected along the wing's upper surface and analyzed with both TecPlot and Matlab. All figures follow the same naming convention: MXXFXTXXDX where any X is a placeholder for each unique run.

1. MXX: Denotes the Mach number. MXX will be M85, M90 or M95 for Mach 0.85, 0.90 and 0.95, respectively.
2. FX: Denotes the oscillation frequency. FX will be F1 or F2 for an oscillation frequency of 5.7 Hz or 7.4 Hz.
3. TXX: Denotes the trim angle or median AoA. TXX will be T04, T07 or T10 for 4°, 7° and 10°, respectively.
4. DX: Denotes the oscillation amplitude or $\Delta\alpha$. DX will be D2 or D4 for an oscillation amplitude of 2° or 4°, respectively.
5. A subset of fully inviscid cases were run alongside the boundary layer coupled cases. The fully inviscid cases will be denoted with an "I" in front of the aforementioned naming procedure.

The following sections will cover the 31 unique test cases for a selection of the chordwise pressure data locations and compare the effects of various LCO simulated flow conditions. Figure 3.7 defines the location of the 4 chordwise pressure sections. A comprehensive collection of the pressure data for all 4 test locations on the wing's upper surface can be found in the appendix for further reference.

For each test case, a wing was sinusoidally oscillated in pitch for a total of two full cycles, with the data from the second cycle used for analysis. The wing began at some predefined trim angle (4°, 7°, or 10°), then perturbed "nose up" to some

maximum angle, perturbed "nose down" to some minimum angle, then returned to the original trim angle. This oscillation process occurred twice to account for transient effects present during the first oscillation cycle. The maximum and minimum angle was based on the original trim angle and the oscillation amplitude (either $\pm 2^\circ$ or $\pm 4^\circ$).

The oscillatory behavior of the shock during the simulated LCO can be characterized by following key features:

1. Distance of shock migration. The migration distance accounts for the transition from $\frac{x}{c}$ right before C_p drops due to the shock for the maximum and minimum C_p time trace.
2. Change in C_p from the maximum and minimum C_p time trace normalized by C_{p0} , the value of C_p right before the shock when $t^* = 0$.

Fig. 4.1 has key features indicated to provide a clearer understanding of the aforementioned points on interest. Each colored line indicates a chordwise time trace of the C_p along the wing's upper surface for various nondimensionalized times such that $t^* = t * frequency$. The time is nondimensionalized for a single cycle with $t^* = 0, 0.25, 0.75,$ and 1 referring to trim, peak nose up, peak nose down, and return to trim positions of the wing, respectively. All key points were chosen qualitatively as the "knee" of the shock. This point was the local maximum of the absolute value of C_p before the drop in C_p due to the pressure jump across the shock.

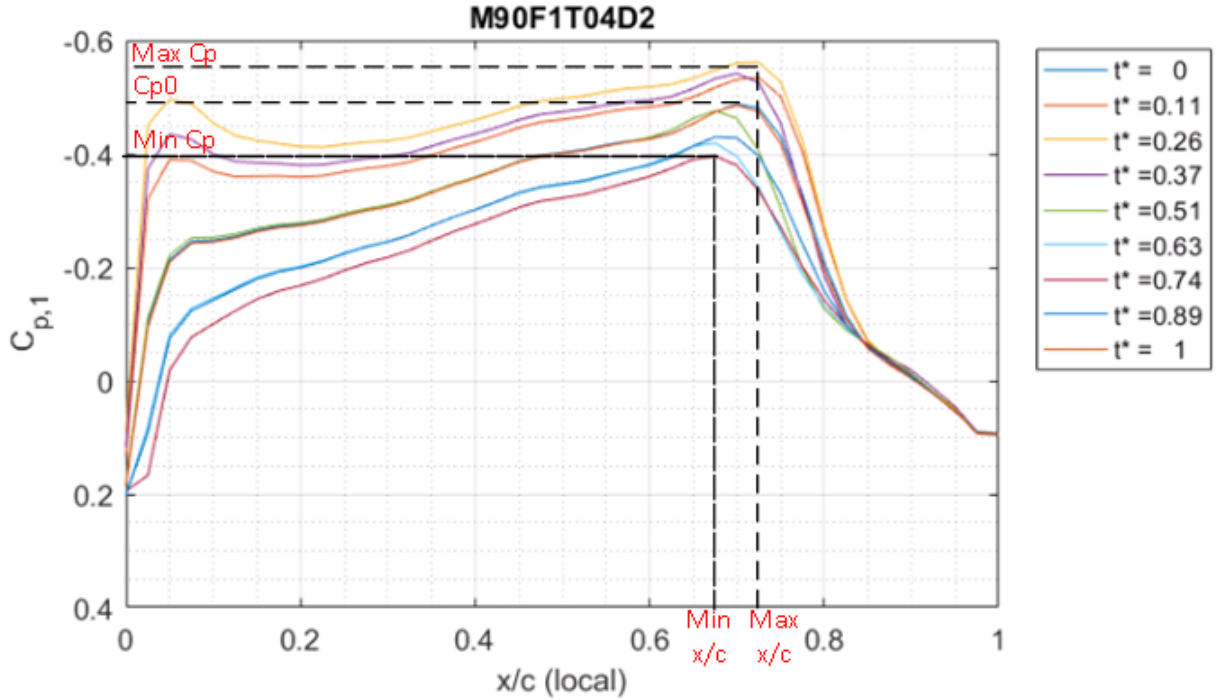


Figure 4.1: Example figure indicating the min and max C_p and $\frac{x}{c}$ as well as C_{p0} for the time trace of C_{p1} . $M = 0.9$, Frequency = 5.7 Hz, Trim = 4° , $\Delta\alpha = 4^\circ$.

4.2 Fully Inviscid and Boundary Layer Coupled Solution

Using the time-accurate solver in ZEUS, the pressure coefficients along the wing's surface were calculated. In addition to investigating the effects of various LCO parameters such as oscillation amplitude and frequency, the modeling of viscous effects was analyzed to determine what differences exist. As an Euler solver, ZEUS can predict shock waves in areas of relatively simple flow. For flows concerning shock boundary layer interactions (SBLI), the flow solution becomes more complex. The figures within this section will compare fully inviscid solutions to boundary layer coupled (BLC) solutions. Figures 4.2, 4.3 and 4.4 display the time trace of the BLC solution on the top row and the fully inviscid solution on the bottom row.

For the least aggressive solution seen in Fig. 4.2 ($M = 0.9$, Trim = 4°), C_{p1} for both the inviscid and BLC solution show good agreement with each other for the first 60% of the chord. After that point, the shock begins to form for the BLC case

and the two solutions diverge. The BLC solution predicts a shock around 0.7-0.75c while the inviscid solution predicts the shock to occur further aft on the wing around 0.75-0.8c. Additionally, the inviscid solution predicts a larger and steeper drop in C_p across the shock.

For the most aggressive solution seen in Fig. 4.3 ($M = 0.9$, $\text{Trim} = 10^\circ$), the solution for C_{p1} shows less agreement than the lower trim case. Solutions remain similar only up to 0.4c, after which the BLC solution predicts a shock to occur around 0.5-0.6c whereas the inviscid solution predicts the shock to occur further aft from 0.7-0.75c. Again, the drop in C_p is much larger and sharper for the inviscid case. For all cases of trim and oscillation amplitude for C_{p1} , the shock movement was predicted to be greater for the BLC case. While the inviscid solution sees shock movement, the range is anywhere from 30% to 50% that of the BLC case.

C_p locations 2 and 3 showed similar trends to location 1. C_{p4} , the location closest to the wingtip, showed the greatest difference between the viscous and inviscid solution. Agreement between the solutions occurred from only 0.05-0.4c with the most agreement at the lowest AoA and least agreement when $\text{trim} = 10^\circ$. Figure 4.4 compares the solution for $\text{trim} = 7^\circ$. For this case the inviscid and BLC solution are similar up to 0.3c with major differences occurring for the $\Delta\alpha = 4^\circ$ case.

In general, the fully inviscid solution predicted the shock to occur further aft on the wing, as well as a larger and steeper drop in C_p across the shock than the BLC solution. In addition to the location of the shock and shock strength, the inviscid solution showed reduced shock migration. The reduced shock strength for the BLC cases may be due to the influence from the boundary layer and resulting shock-boundary layer interactions. The increased shock migration for the BLC cases could be a result of changes in the boundary layer thickness, to include possible separation in the boundary layer aft of the shock. While ZEUS provides quasi-steady pressure data on the wing's surface, it was not possible to confirm the presence of separated flow. Inboard locations of the two solution methods had more similar results while

the most outboard location (C_{p4}) showed the greatest discrepancy between the BLC and inviscid solution. This is due to how close to the leading edge the shock occurred for the wingtip location, which resulted in solution divergence occurring much farther up the wing than the inboard locations.

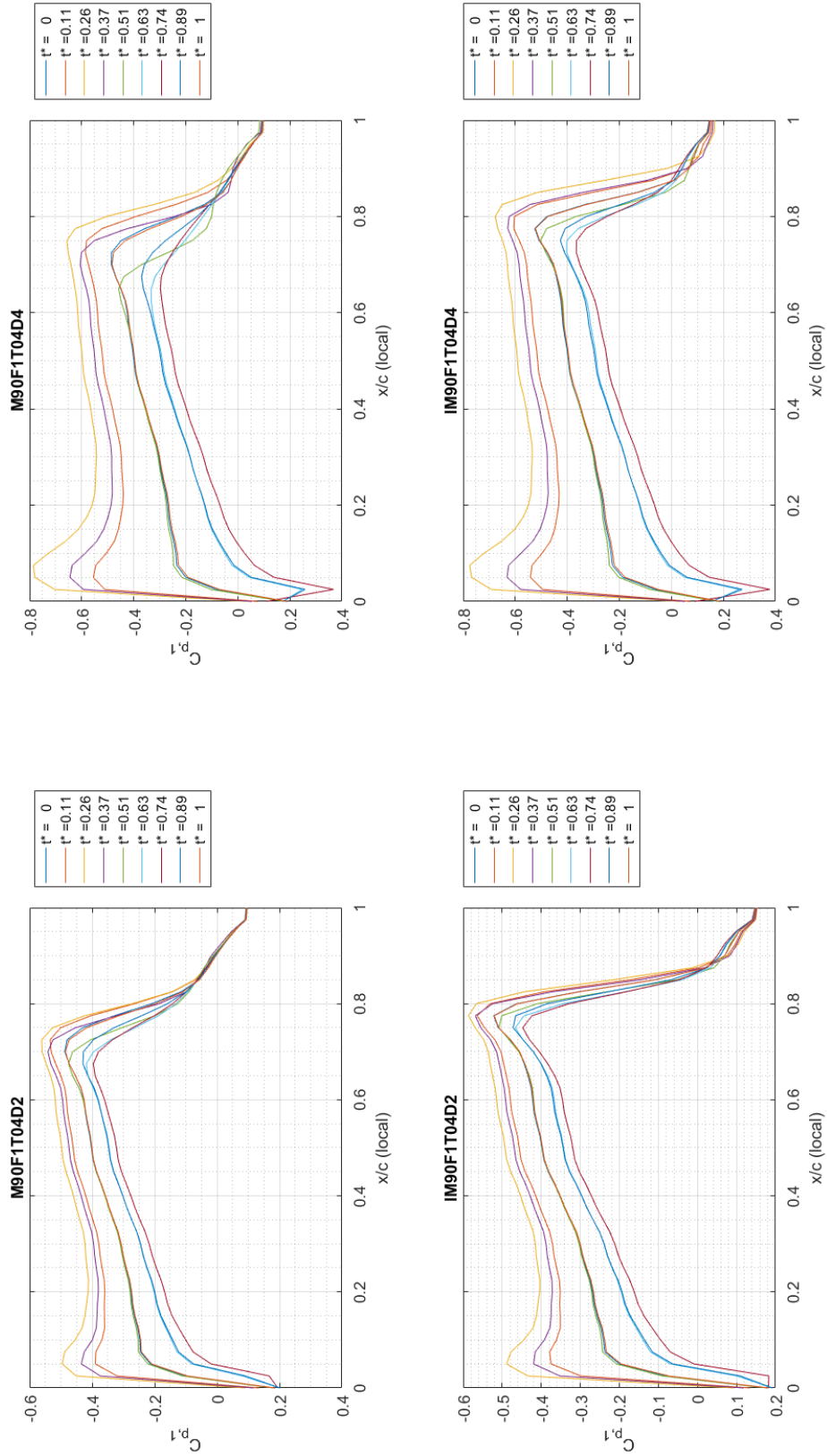


Figure 4.2: Inviscid/Viscous comparison for C_{p1} . $M = 0.9$, Frequency = 5.7 Hz, Trim $\alpha = 4^\circ$.

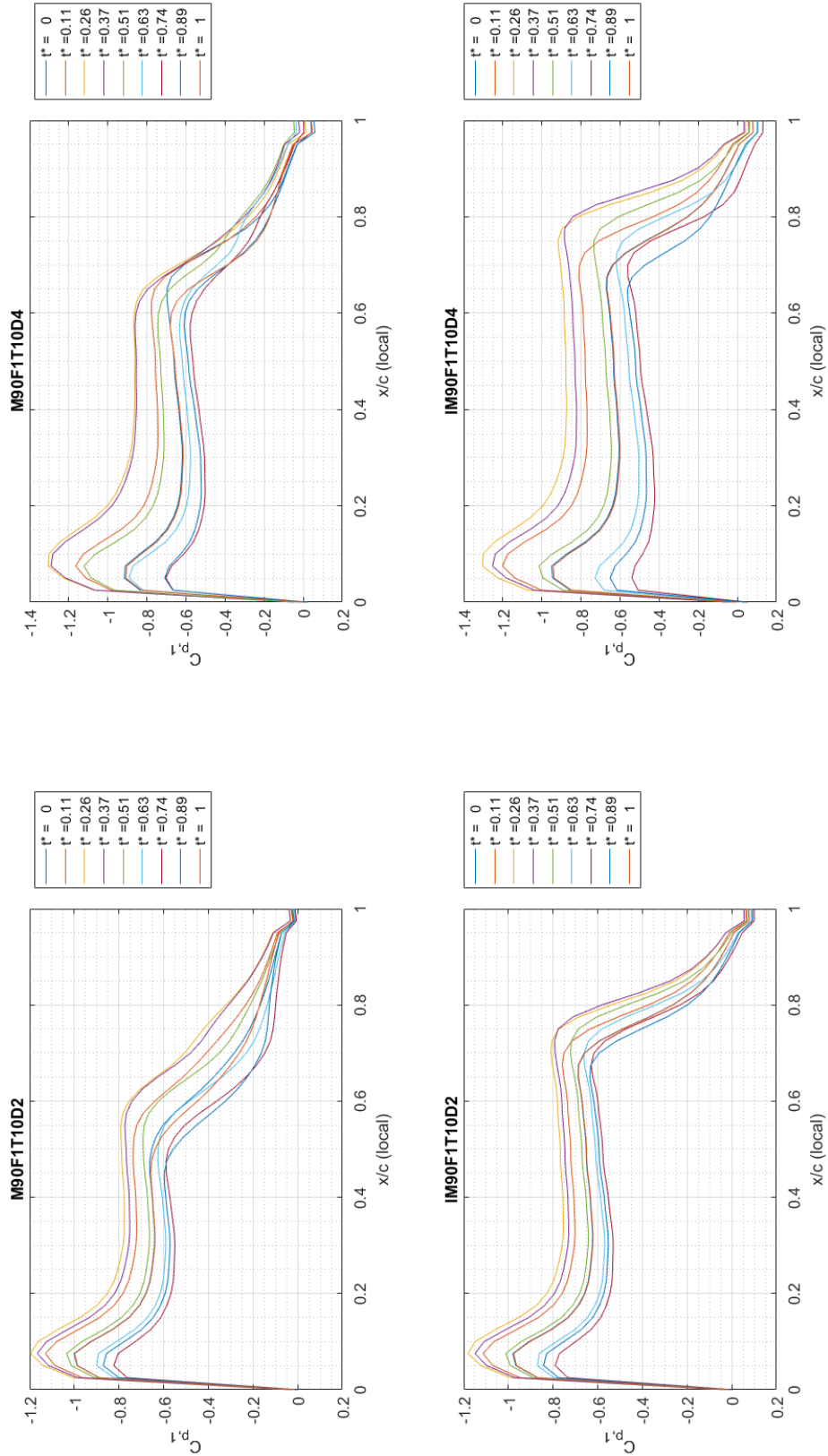


Figure 4.3: Inviscid/Viscous comparison for C_{p1} . $M = 0.9$, Frequency = 5.7 Hz, Trim $\alpha = 10^\circ$.

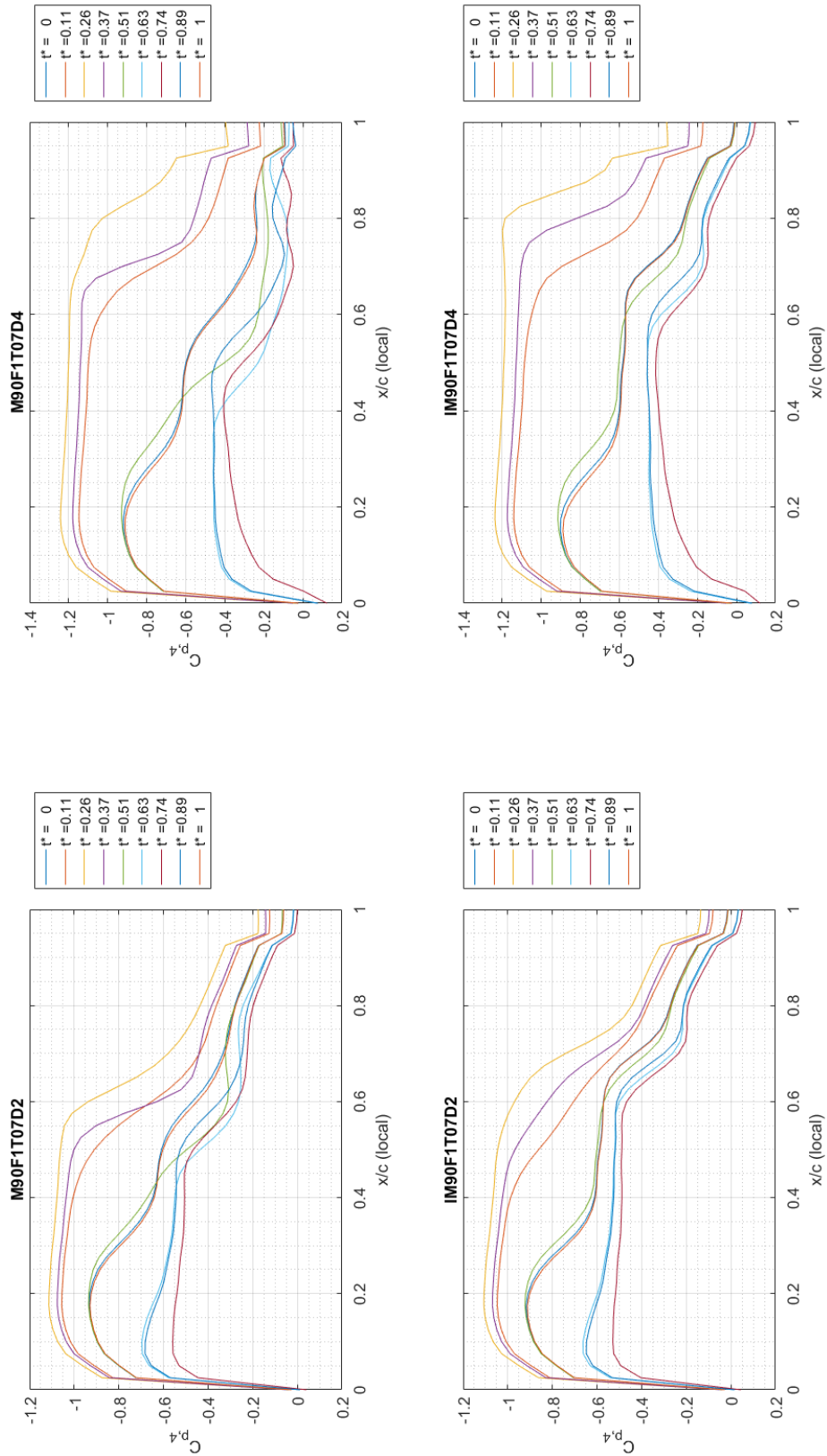


Figure 4.4: Inviscid/Viscous comparison for C_{p4} . $M = 0.9$, Frequency = 5.7 Hz, Trim $\alpha = 7^\circ$.

4.3 Effects of Median AoA and Oscillation Amplitude

This section serves to identify trends seen by altering the trim AoA and the oscillation amplitude. Cases were run for $M = 0.90, 0.95$ at trim = $4^\circ, 7^\circ, 10^\circ$ and $\Delta\alpha = \pm 2^\circ, \pm 4^\circ$. All cases can be seen in Figures 4.5 and 4.6.

For the $M = 0.9$ cases, increasing the trim AoA reduces the severity in the drop in C_p . For trim = 10° , there may not even be a shock present on the wing, although there is no quantitative data produced from the ZEUS solution to confirm or deny whether or not a shock is present. The reduced drop in C_p may be due to regions of separation which develop as the AoA increases. Increasing $\Delta\alpha$ primarily affects the range of observed shock migration. The higher oscillation amplitude results in a shock migration of about twice that of the lower oscillation amplitude. Similar trends can be seen for the $M = 0.95$ cases. The shock remains more coherent over the course of the wing oscillation, but again the higher amplitude oscillation produces a larger shock migration than the lower amplitude oscillation.

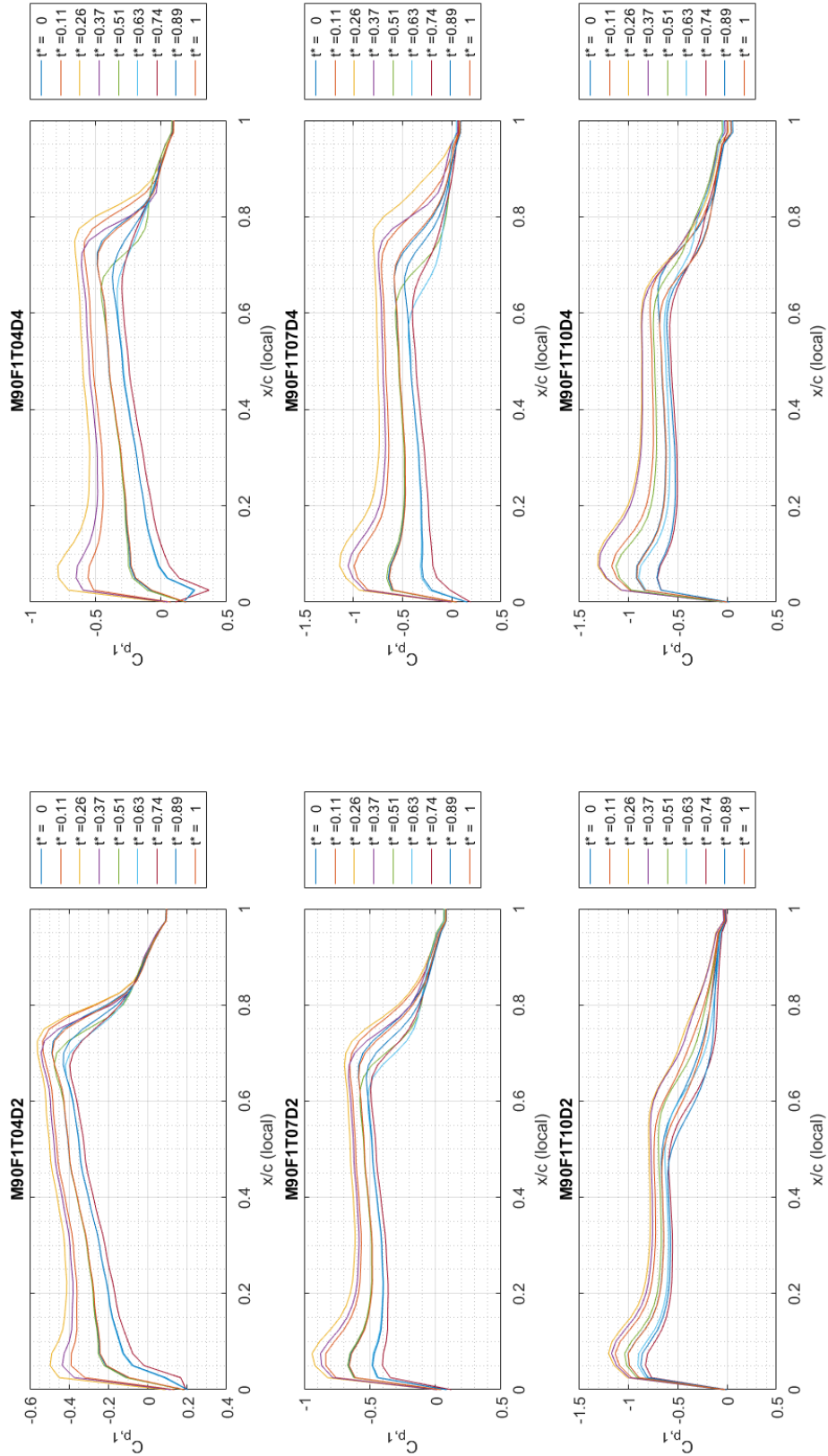


Figure 4.5: BLC trim and $\Delta\alpha$ comparison for C_{p1} . $M = 0.9$, Frequency = 5.7 Hz.

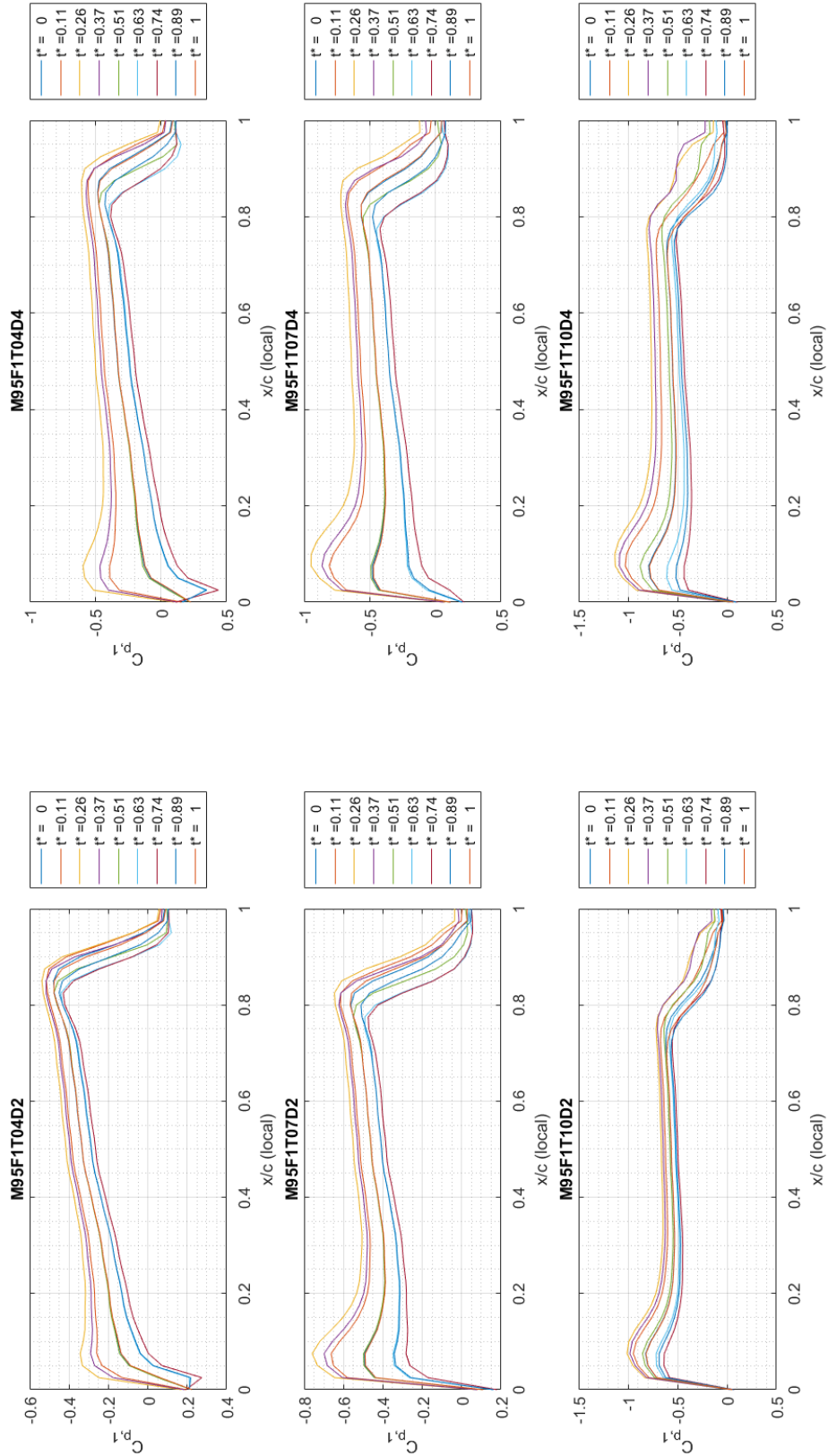


Figure 4.6: BLC trim and $\Delta\alpha$ comparison for C_{p1} . $M = 0.95$, Frequency = 5.7 Hz.

4.4 Frequency Comparison

Another parameter of LCO is the frequency at which the oscillations occur. The oscillation frequencies were chosen as 5.7 Hz and 7.4 Hz, both of which were picked to match the reduced frequencies used in Cunningham's experiment. In regards to extrapolating this information to real world flight test, the absolute value of the oscillation frequency is not as important as their relative values in reference to each other. Namely, the wing was oscillated at a baseline frequency (5.7 Hz), then the oscillation frequency was increased by 30% (7.4 Hz).

Trends were similar for all 4 C_p locations at both $M = 0.9$ and $M = 0.95$ with position 4 showing the greatest variance. For position 1 as seen in Fig. 4.7, plots of the time trace of C_p for the lower oscillation frequency are located along the top row with the corresponding high frequency test case shown immediately below. Five time stamps are shown to indicate the beginning, middle, end, peak nose up and peak nose down positions of the wing. Both frequencies have almost identical results with the exception of $t^* = 0.5$. The middle time step shows that the higher frequency oscillation produces greater a lag in the development of C_p along the wing's surface when compared the the lower frequency. All 4 test cases for all 4 positions indicate the same result. Interestingly, both the peak nose up and peak nose down time trace for both frequencies are nearly identical. This shows that the shock movement and change in C_p are independent of the two frequencies tested.

For C_{p4} seen in Fig. 4.8, the same trends are present for both oscillation frequencies. The peak nose up and nose down time traces show very little difference across the frequency range while the $t^* = 0.5$ time trace indicates a more pronounced lag for the higher frequency cases. The trim C_p lines ($t^* = 0.0, 1.0$) are of lower magnitude for all higher frequency cases. While all other LCO conditions are kept constant and only oscillation frequency changes, the flow at the median AoA develops slightly differently for each frequency while the peak values remain the same.

Fig. 4.9 plots the value of C_p with respect to time for three points along the chord of position 1. The six plots cover each test case for $M = 0.9$, frequency = 5.7 Hz. The solid purple line provides a reference to the rotation of the wing about the rotation axis, indicating a pitch doublet. The magnitude of the input was scaled to the maximum value of C_p at 0.25c and given the same initial value of C_p as the quarter-chord. The quarter-chord and half-chord data points show a smooth change in C_p that follows the oscillation of the wing. The 0.75c point provides the most interesting data. For the trim = 4° , $\Delta\alpha = 2^\circ$ case, C_p is a smooth sinusoid similar to the other points on the wing. For the trim = $4^\circ, 7^\circ$, $\Delta\alpha = 2^\circ$ cases, C_p dives down around $t^* = 0.4$. This sharp change in C_p is due to the shock transition moving across this point. As the wing begins to nose down from the peak AoA, the shock migrates forward on the wing. As the shock passes across the 0.75c point at position 1, the C_p drops dramatically. For both of the trim = 10° cases, C_p at point 0.75c is dramatically lower than the lower trim cases because the shock remains forward of this point during the entirety of the oscillation.

Similar results can be seen in Fig. 4.10. These cases were run at $M = 0.95$ which resulted in the shock positioned further aft on the wing than the lower Mach cases. For the trim = 4° , $\Delta\alpha = \pm 2^\circ, \pm 4^\circ$ cases, the characteristic dip in C_p at position 0.85c indicates the shock has transitioned across that point during the oscillation of the wing.

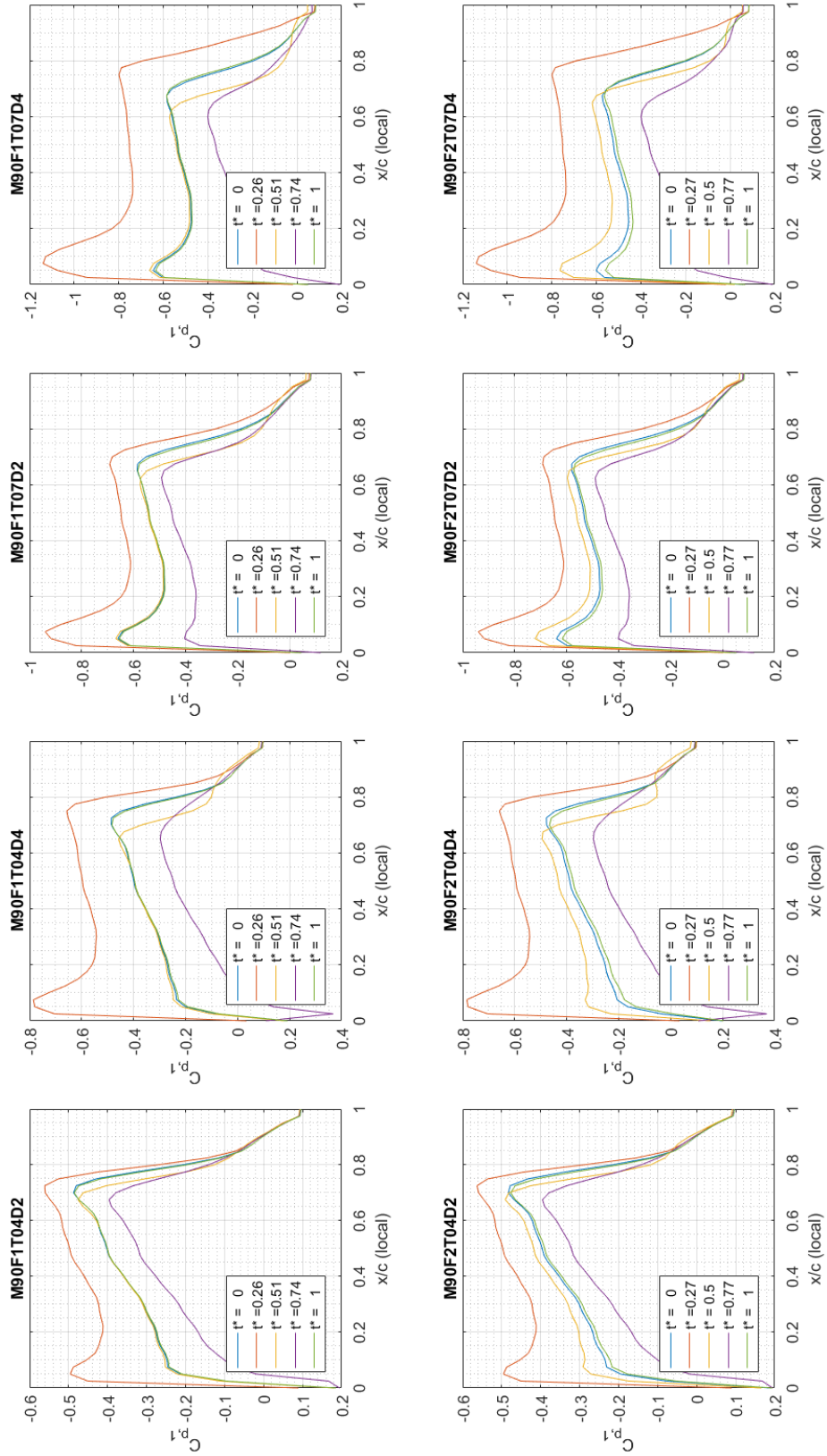


Figure 4.7: BLC frequency comparison for C_{p1} . $M = 0.9$, Frequency = 5.7/7.4 Hz.

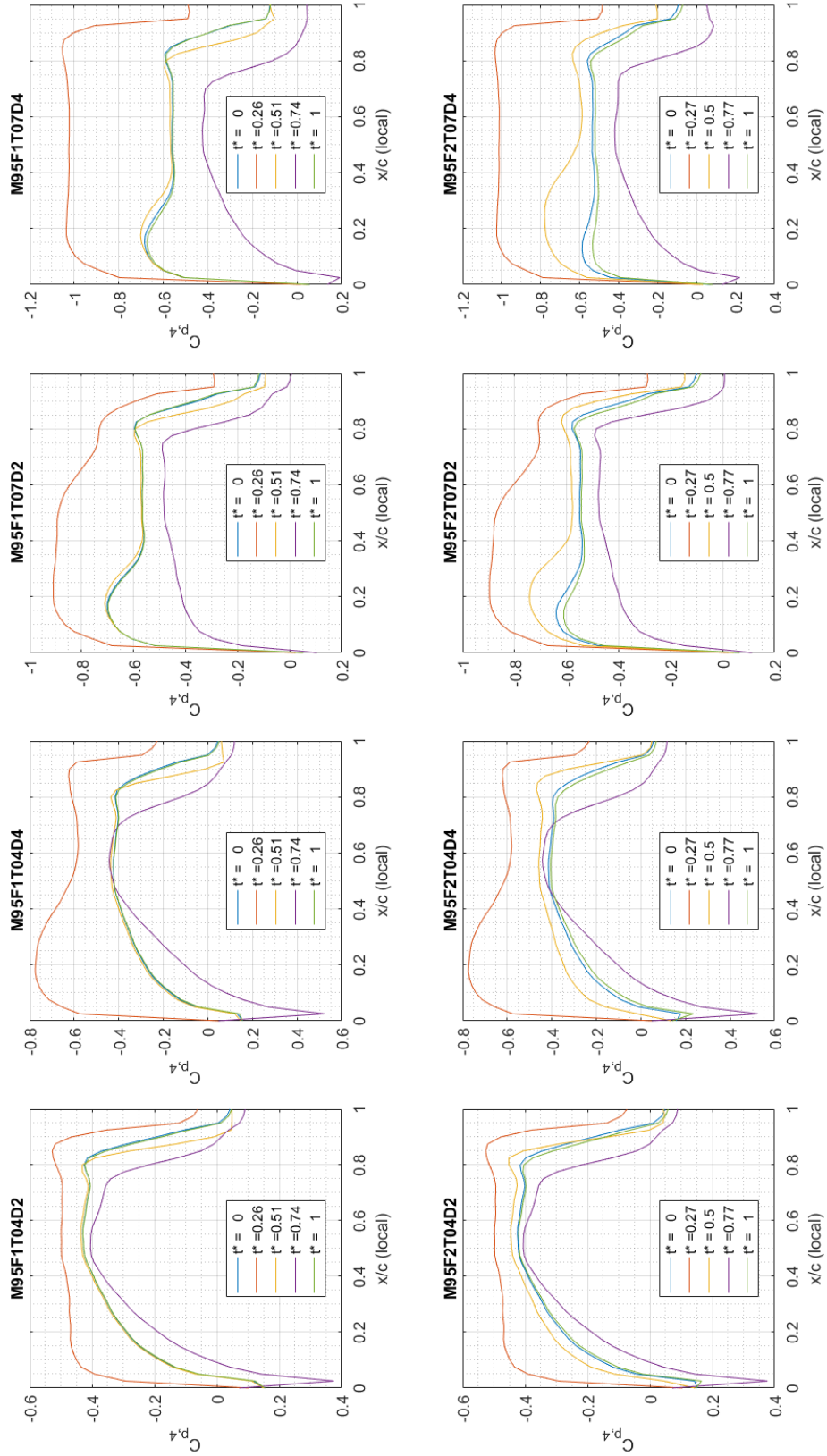


Figure 4.8: BLC frequency comparison for C_{p4} . $M = 0.95$, Frequency = 5.7/7.4 Hz.

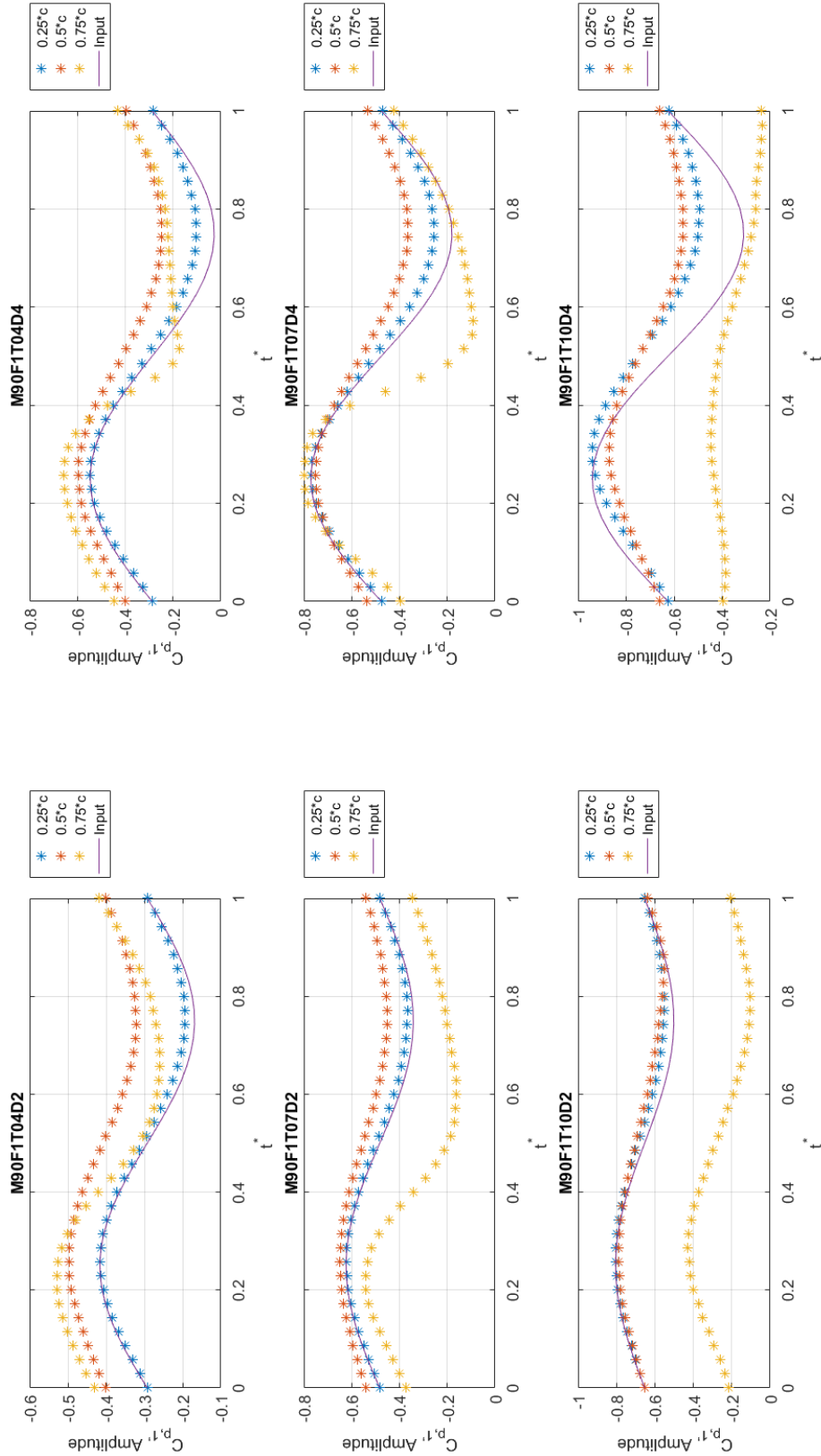


Figure 4.9: Time history of C_p for three points along the chord of position 1. $M = 0.9$, Frequency = 5.7 Hz.

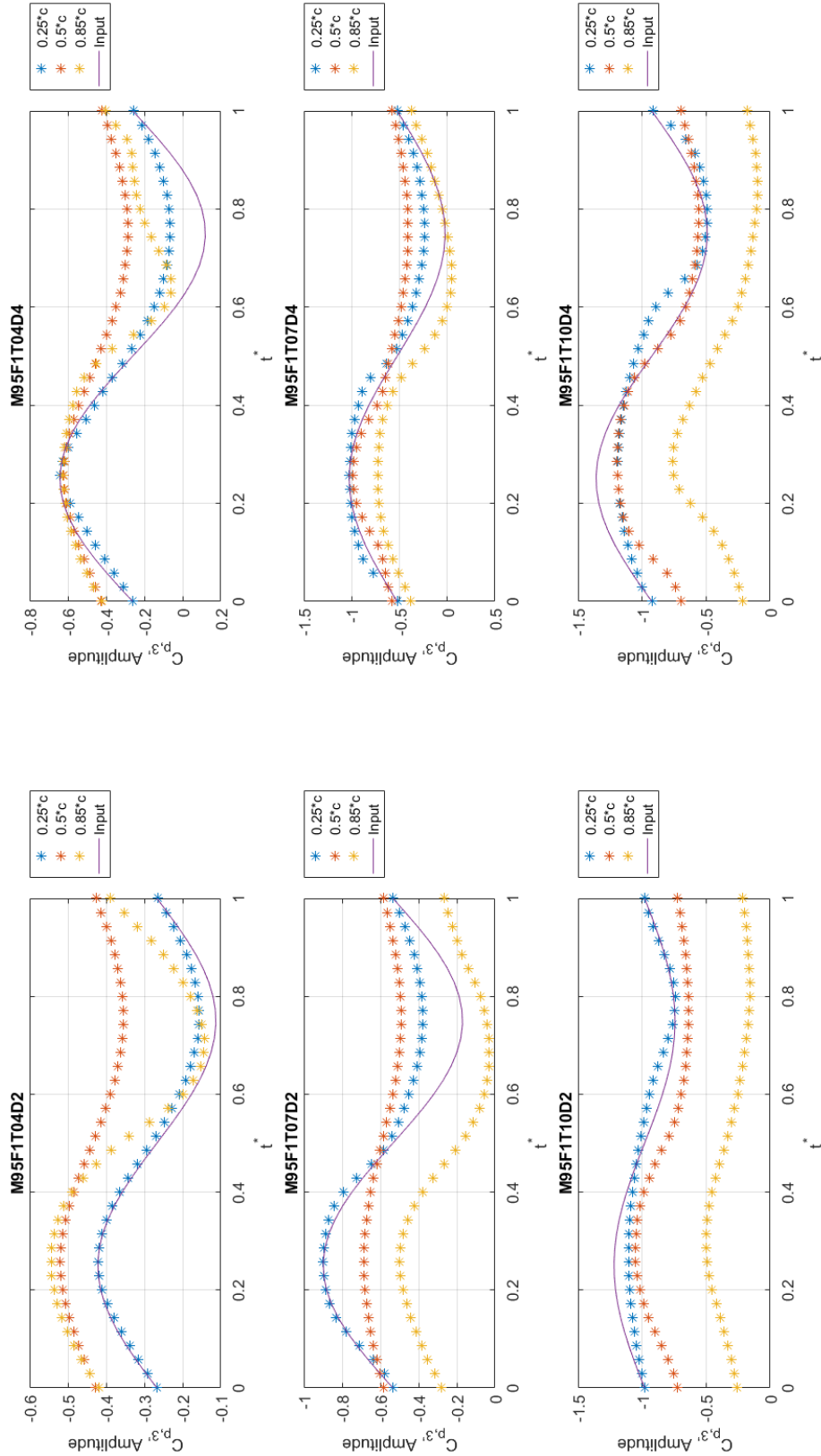


Figure 4.10: Time history of C_p for three points along the chord of position 3. $M = 0.95$, Frequency = 5.7 Hz.

4.5 Comparison of Shock Migration at Various Spanwise Locations

Up until this point, all of the results for each of the 4 spanwise locations along the wing have been presented independent of one another. This section serves to provide the reader with some context as to how the C_p at each location developed over the course of the oscillation. Figure 4.11 shows all four spanwise locations for selected times during the oscillation. At the initial median AoA position ($t^* = 0$), the shock remains nearly orthogonal to the root chord, indicated by the proximity of the shock for all 4 positions. As the wing is oscillated to the peak amplitude ($\alpha = 6^\circ$), slight shock movement aft can be seen on C_{p4} . As time progresses, the shock remains relatively close along the span. For the most part, the shock location remains in the same vicinity for all 4 spanwise positions.

Fig. 4.12 tells a different story. At $t^* = 0$, the shock location remains essentially constant for each position. As the wing is oscillated to the peak amplitude at $t^* = 0.23$ ($\alpha = 11^\circ$), the shock can be seen much further aft for position 4 while the shock remains coalesced for the other 3 wing stations. As the wing oscillates back down in pitch at $t^* = 0.49$ the shock at position 4 moves back to the group and falls in line with the other stations when $t^* = 0.74$. Figure 4.12 shows that for this slightly more aggressive simulated LCO case, C_{p4} experiences more shock movement than the other inboard positions. Figures 4.13 through 4.16 present the pressure data along the wing's surface for the 4 discrete time steps shown in Fig. 4.12.

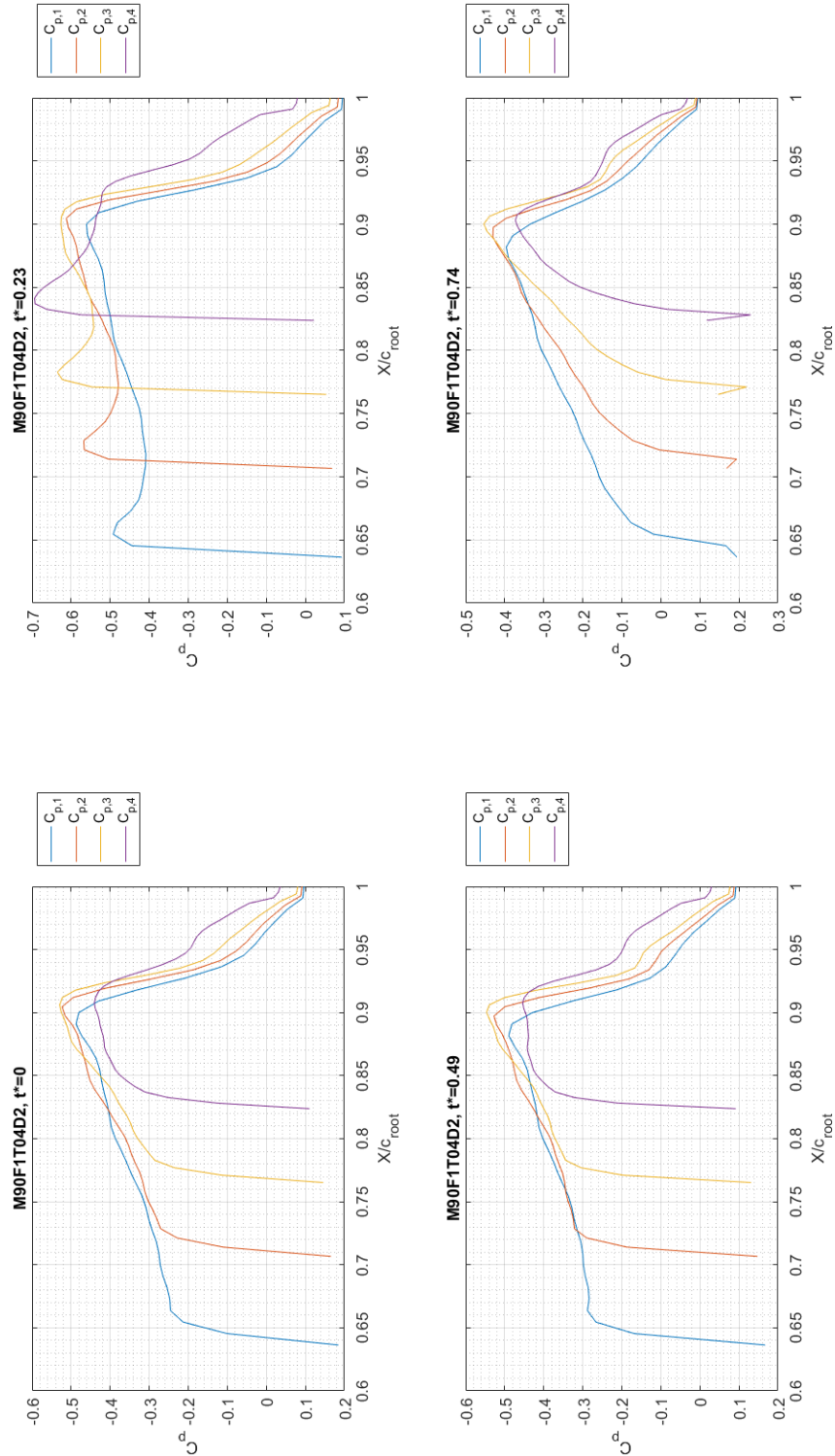


Figure 4.11: Time history of C_p for all 4 positions along the wing. The chordwise position, X , has been normalized by the root chord to retain each position's relative distance to one another. $t^* = 0.23, 0.74$ indicate peak nose up and nose down of the wing, respectively. $M = 0.9$, Frequency = 5.7 Hz, Trim = 4° , $\Delta\alpha = 2^\circ$.

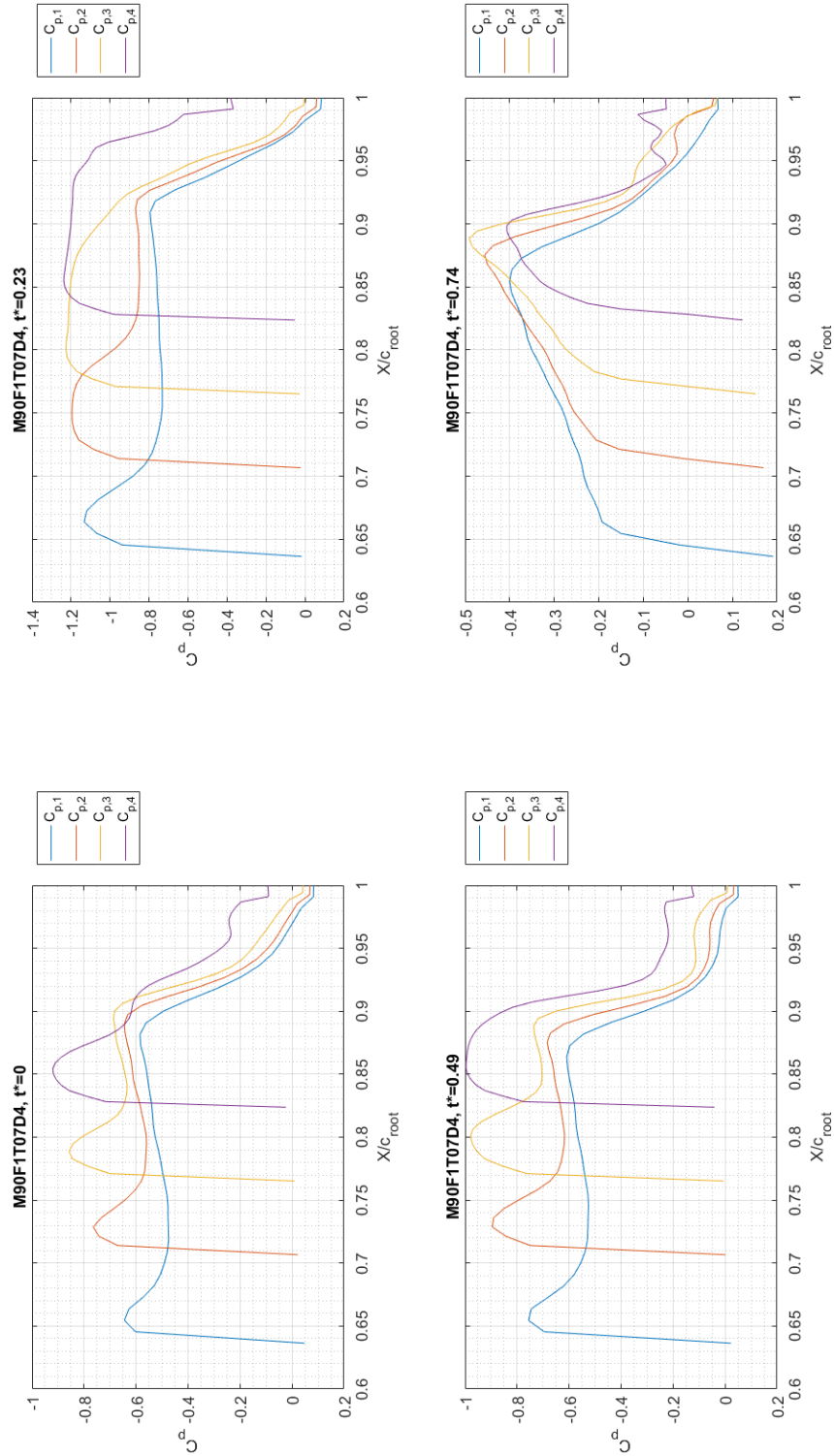


Figure 4.12: Time history of C_p for all 4 positions along the wing. The chordwise position, X , has been normalized by the root chord to retain each position's relative distance to one another. $t^* = 0.23, 0.74$ indicate peak nose up and nose down of the wing, respectively. $M = 0.9$, Frequency = 5.7 Hz, Trim = 7° , $\Delta\alpha = 4^\circ$.

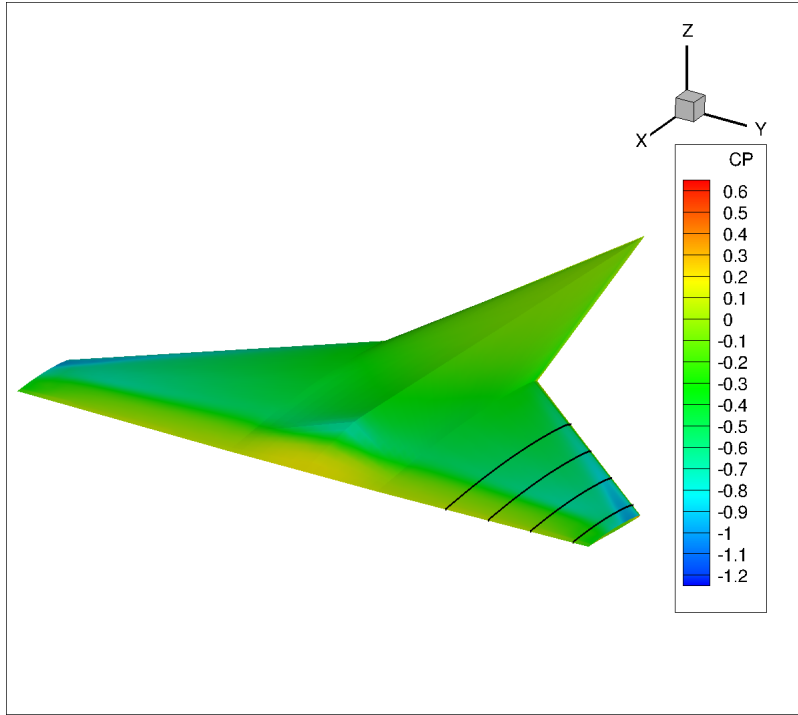


Figure 4.13: Time stamp of C_p when $t^* = 0.0$ indicating trimmed position. $M = 0.9$, Frequency = 5.7 Hz, Trim = 7° , $\Delta\alpha = 4^\circ$.

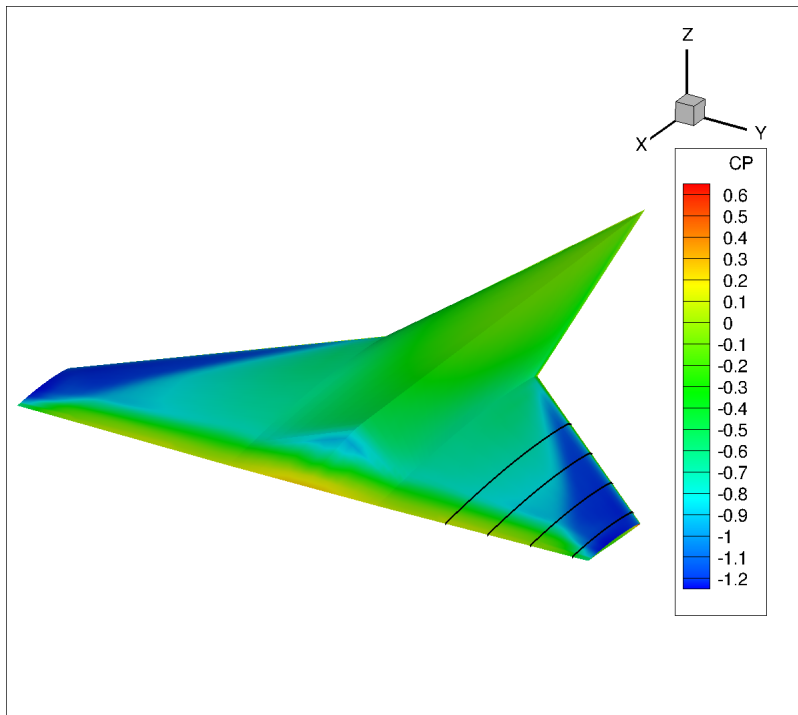


Figure 4.14: Time stamp of C_p when $t^* = 0.0$ indicating peak nose up position. $M = 0.9$, Frequency = 5.7 Hz, Trim = 7° , $\Delta\alpha = 4^\circ$.

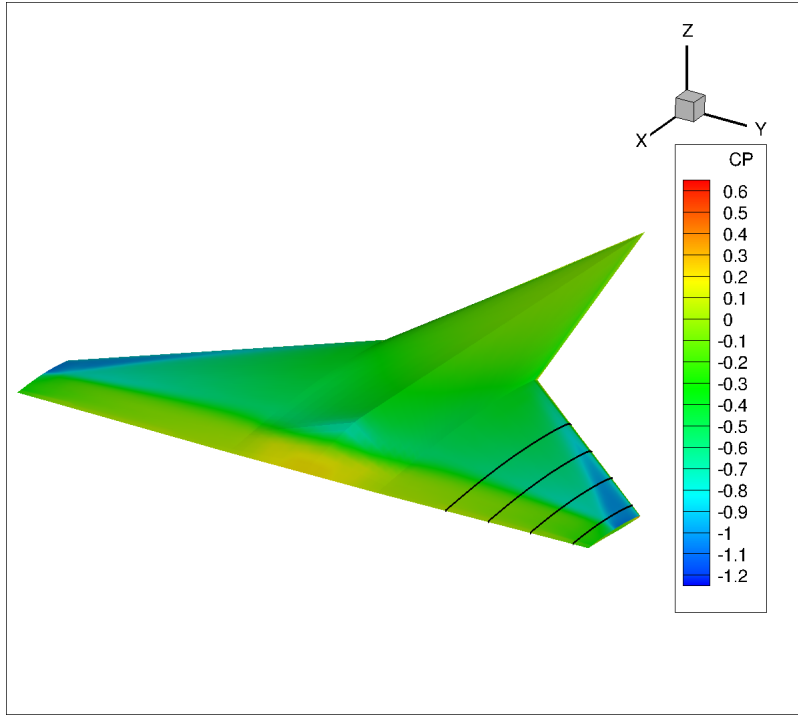


Figure 4.15: Time stamp of C_p when $t^* = 0.0$ indicating oscillating nose down past trim. $M = 0.9$, Frequency = 5.7 Hz, Trim = 7° , $\Delta\alpha = 4^\circ$.

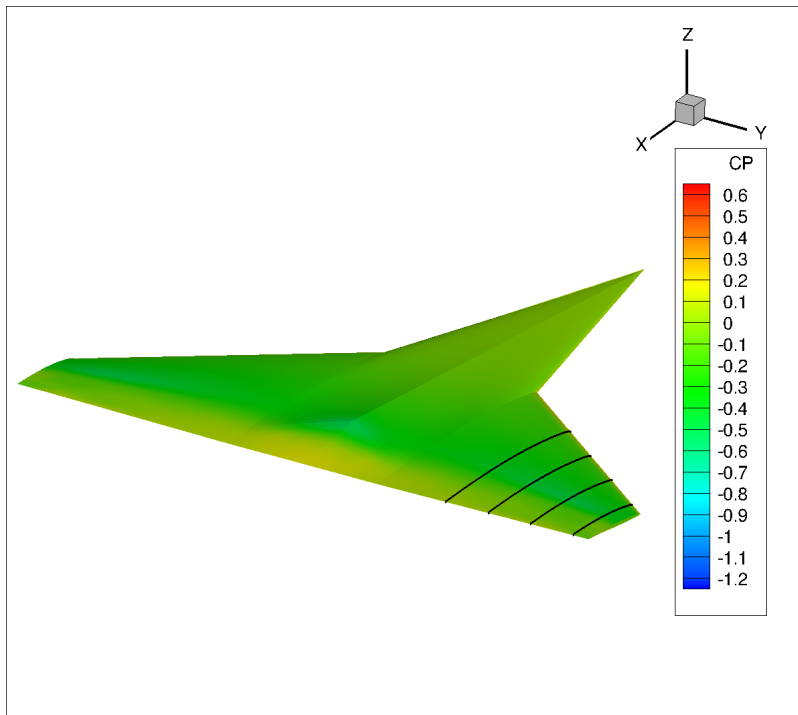


Figure 4.16: Time stamp of C_p when $t^* = 0.0$ indicating peak nose down position. $M = 0.9$, Frequency = 5.7 Hz, Trim = 7° , $\Delta\alpha = 4^\circ$.

4.6 *Variation in Moment Coefficient*

The following Figs. 4.17 through 4.19 present the change in the quarter-chord pitching moment coefficient ($C_{m,\frac{\epsilon}{4}}$) during the wing's oscillation. All inviscid cases along with their analogous BLC counterparts are presented to show the differences in the two methods as well as how the moment at all 4 wing stations varied over the course of the oscillation.

For all test cases, $C_{m,\frac{\epsilon}{4}}$ for stations 1, 2 and 3 remain coalesced with no major deviations while $C_{m,\frac{\epsilon}{4}}$ at station 4 is much more sporadic. Again, due to station 4's proximity to the wingtip, vortices may play a role in the observed behavior at this station. The basic shape for the variation in $C_{m,\frac{\epsilon}{4}}$ for all 4 stations resembles a sinusoidal wave, although with a much flatter peak across the second half of the oscillation, which may be due to aerodynamic lag in the development of the flow along the wing's surface.

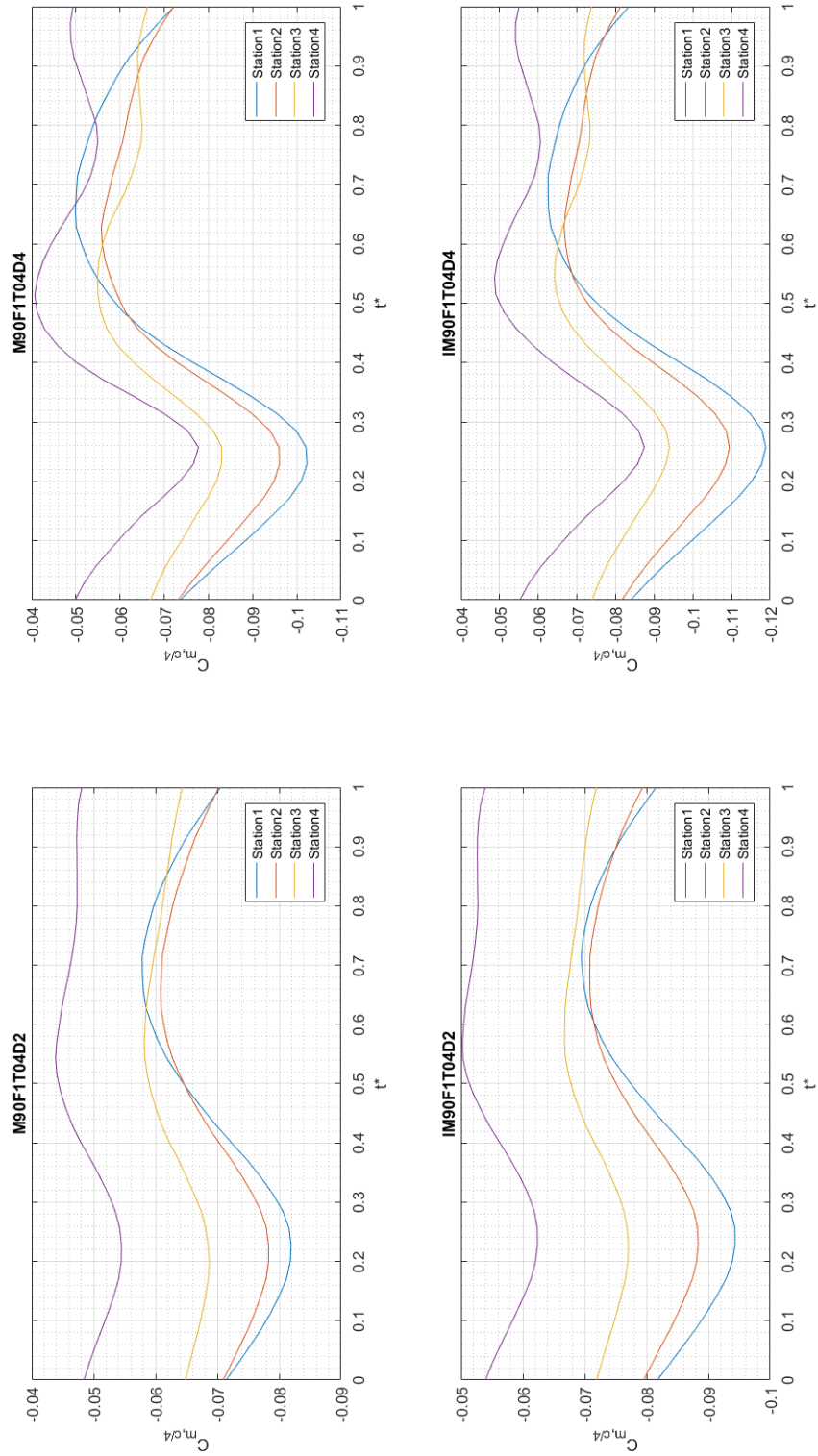


Figure 4.17: Variation in the pitching moment coefficient about the quarter-chord for each wing station over the course of a single oscillation. $M = 0.9$, Frequency = 5.7 Hz, Trim = 04° , $\Delta\alpha = \pm 2^\circ, \pm 4^\circ$, BLC and Inviscid.

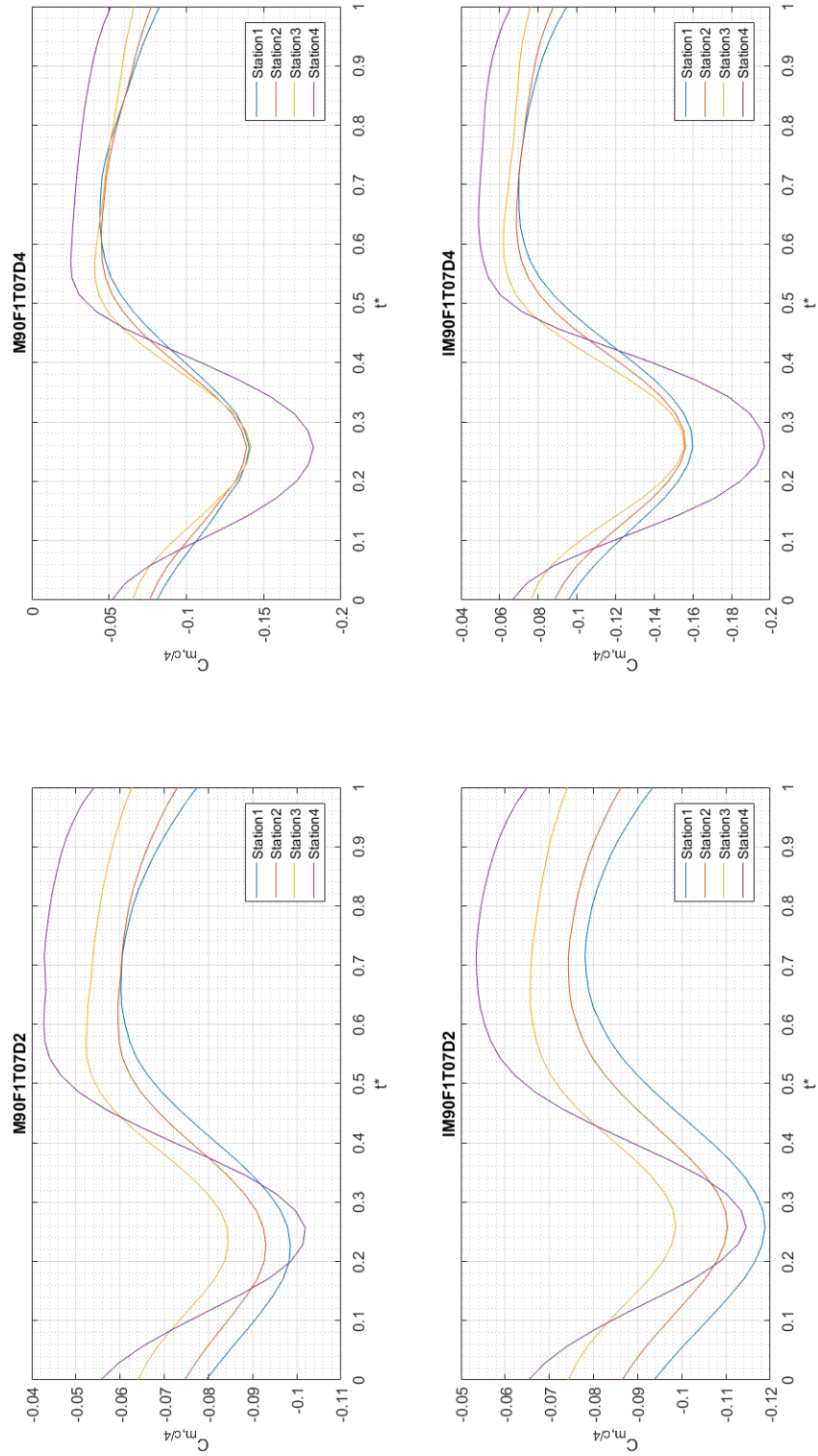


Figure 4.18: Variation in the pitching moment coefficient about the quarter-chord for each wing station over the course of a single oscillation. $M = 0.9$, Frequency = 5.7 Hz, Trim = 07° , $\Delta\alpha = \pm 2^\circ, \pm 4^\circ$, BLC and Inviscid.

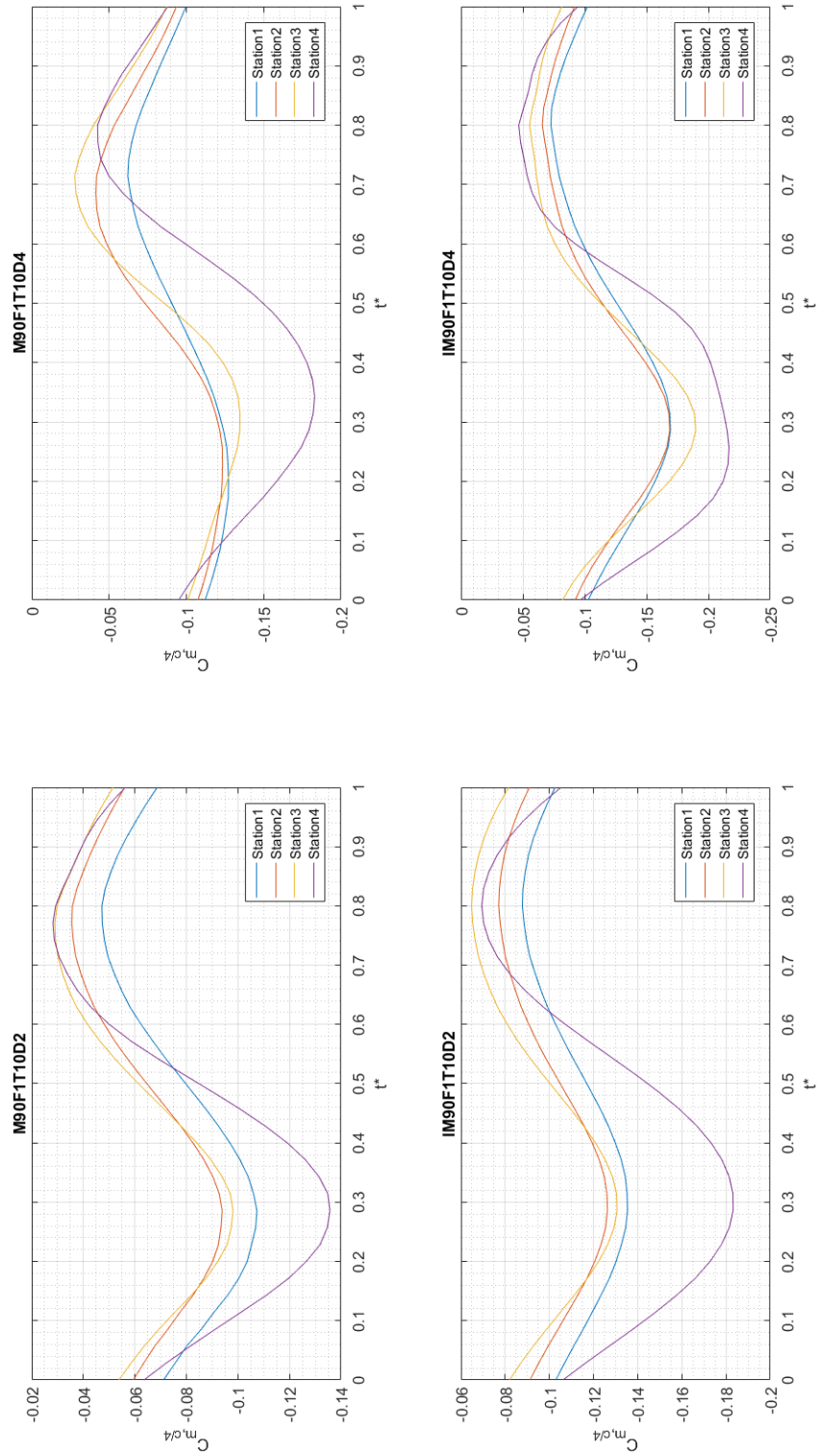


Figure 4.19: Variation in the pitching moment coefficient about the quarter-chord for each wing station over the course of a single oscillation. $M = 0.9$, Frequency = 5.7 Hz, Trim = 10° , $\Delta\alpha = \pm 2^\circ, \pm 4^\circ$, BLC and Inviscid.

4.7 Summary of Results

The following parameters were adjusted to determine their effect on possible shock migration during simulated LCO:

1. Mach number
2. Trim AoA
3. $\Delta\alpha$
4. Oscillation frequency
5. Fully inviscid solution vs BLC

This section contains an itemized table for the various LCO conditions with the above parameters varied at station 1 on the wing. Stations 2 and 3 show similar trends to station 1. Station 4 experienced much more variability due to its proximity to the wingtip and thus it was difficult to qualitatively assess the shock migration with consistency. The foremost and aftmost shock position as well as their associated peak C_p value are tabulated on the next page in Table 4.1. The peak value of C_p before the shock while the wing is at trim, C_{p0} , has also been recorded and used to normalize the percent change in C_p as the wing oscillates.

Table 4.1: Tabulated Results for cases of interest for position 1 on the wing. The shock movement is reported in percent of local chord. The percent change in C_p from the shock migration is reported as $(C_{p,max} - C_{p,min})/C_{p0}$

				Frequency = 5.7 Hz		Frequency = 7.4 Hz	
Mach	ω	Trim	$\Delta\alpha$	% Movement	% Cp change	% Movement	% Cp change
0.9	5.7/7.4	4	2	5.0%	35%	5.0%	35%
0.9	5.7/7.4	4	4	7.5%	79%	7.5%	76%
0.9	5.7/7.4	7	2	7.5%	33%	7.5%	34%
0.9	5.7/7.4	7	4	15.0%	67%	15.0%	71%

				M = 0.90		M = 0.95	
Mach	ω	Trim	$\Delta\alpha$	% Movement	% Cp change	% Movement	% Cp change
0.9/0.95	5.7	4	2	5.0%	35%	5.0%	23%
0.9/0.95	5.7	4	4	7.5%	79%	10.0%	38%
0.9/0.95	5.7	7	2	7.5%	33%	5.0%	30%
0.9/0.95	5.7	7	4	15.0%	67%	7.5%	53%
0.9/0.95	5.7	10	2	10.0%	31%	5.0%	23%
0.9/0.95	5.7	10	4	2.5%	41%	5.0%	43%

				M = 0.90, BLC		M = 0.9, Inviscid	
Mach	ω	Trim	$\Delta\alpha$	% Movement	% Cp change	% Movement	% Cp change
0.9	5.7	4	2	5.0%	35%	2.5%	27%
0.9	5.7	4	4	7.5%	79%	5.0%	60%
0.9	5.7	7	2	7.5%	33%	2.5%	30%
0.9	5.7	7	4	15.0%	67%	7.5%	57%
0.9	5.7	10	2	10.0%	31%	5.0%	23%
0.9	5.7	10	4	2.5%	41%	7.5%	54%

V. Conclusions and Recommendations

This research sought to replicate simulated LCO motion of a straked delta wing design. A rigid wing was oscillated in pitch for various flight conditions with the use of ZEUS, a commercial Euler-based CFD program.

5.1 Shock Migration and Variable Shock Strength during LCO

LCO parameters such as median AoA, oscillation amplitude, oscillation frequency and Mach number were varied as well as the type of numerical solver used in order to observe potential shock migration due to nonlinear aerodynamic flow on the wing.

5.1.1 Shock Migration. Both the baseline frequency (5.7 Hz) and the 30% elevated frequency (7.4 Hz) experience the same amount of shock migration and no noticeable differences were observed. For the Mach comparison the wing was trimmed at all three AoAs (4° , 7° and 10°) and both $\Delta\alpha$ s ($\pm 2^\circ$, $\pm 4^\circ$). For 5 of the 6 cases, $M = 0.90$ experienced the same or more shock movement than $M = 0.95$. For all $M = 0.90$ and $M = 0.95$ cases, increasing the oscillation amplitude from 2° to 4° increased the total shock migration. For the $M = 0.90$, increasing the trim while holding the oscillation amplitude constant lead to increased shock migration. For the $M = 0.95$ cases, increasing the trim for $\Delta\alpha = 2^\circ$ resulted in the same percent shock movement for all three cases while increasing the trim for $\Delta\alpha = 4^\circ$ actually reduced the percent shock movement. When comparing the fully inviscid solution to the boundary layer coupled (BLC) solution, the BLC solution saw 2-3 times greater range of shock movement as the inviscid solution.

5.1.2 Change in C_p during Oscillation. Both the baseline frequency (5.7 Hz) and the 30% elevated frequency (7.4 Hz) experience the same percent change in C_p and no noticeable differences were observed. For the Mach comparison, the lower Mach number ($M = 0.90$) experienced larger changes in percent C_p (3-41%) than that of the $M = 0.95$ cases. For both Mach numbers, increasing the oscillation amplitude

from 2° to 4° led to much more drastic percent change in C_p (10-45% greater). While the BLC solution experienced a larger percent change in C_p when compared to the inviscid solution for all cases, the difference was not as drastic as the trends seen in the shock migration. Additionally, the percent change in C_p does not tell the fully story as the drop in C_p across the shock was much more significant in the inviscid cases. The total drop in C_p was greater as well as the rate at which the C_p dropped.

In reference to Tauer's flight test results [28] regarding SITES as a aerodynamic phenomena associated with transonic LCO of the F-16, he did not see any shock movement in response to the pitching/plunging of the wing during LCO. Despite the lack of oscillatory shock behavior, Taur's flight test consisted of examining a small region of the wing near the wingtip. As seen in Fig. 4.12, the shock behavior near the wingtip may not be indicative of the shock movement for sections of the wing located further inboard. A time-accurate aeroelastic analysis of the full F-16 computational model in ZEUS would allow for better insight to oscillatory shock migration: if shock migration should be expected to occur based on the flight conditions and where along the span of the wing it should occur. A supplemental flight test to Taur's initial findings based on the results of the full F-16 model would provide more definitive evidence to SITES' role in LCO.

5.2 Future Research Areas

While this thesis identified several characteristics observed during simulated LCO, validation of these results is needed to confirm the feasibility of the boundary layer coupled Euler method (ZEUS). In addition to validation, an analogous Navier-Stokes solution would provide another source which to compare results against.

5.2.1 Validation of ZEUS results. A time accurate analysis of a straked delta wing design oscillated in pitch was conducted to replicate unsteady wind tunnel tests conducted by Cunningham in 1993. While a database of unsteady results for the wind tunnel data can be found, it is unclear to as how the unsteady coefficients

for the harmonic motion of the wing was obtained. Once the method of unsteady calculations is determined, the time accurate data presented in the current study can be compared to the wind tunnel data and provide validation for the use of ZEUS.

5.2.2 Replicate Experiment with a Navier-Stokes Solver. Comparison of the BLC solution to unsteady Navier-Stokes results would provide insight to the importance of viscous models when simulating LCO. A NS solution would account for large regions of separation if they are present and their contribution to shock migration on an oscillating wing. As seen in an experiment by Nikbay [24], the BLC solution had a tendency to both overpredict the shock strength and position the shock further aft on the wing than the wind tunnel results. The NS solver used by Nikbay (FUN3D) had the same trends as the BLC solution, although to a lesser degree. A comparison of the results within the current investigation to a NS solution would highlight any discrepancies between the two methods and further demonstrate the trade-off between solution time and solution accuracy.

Appendix A. C_p Data for Wing Station 1

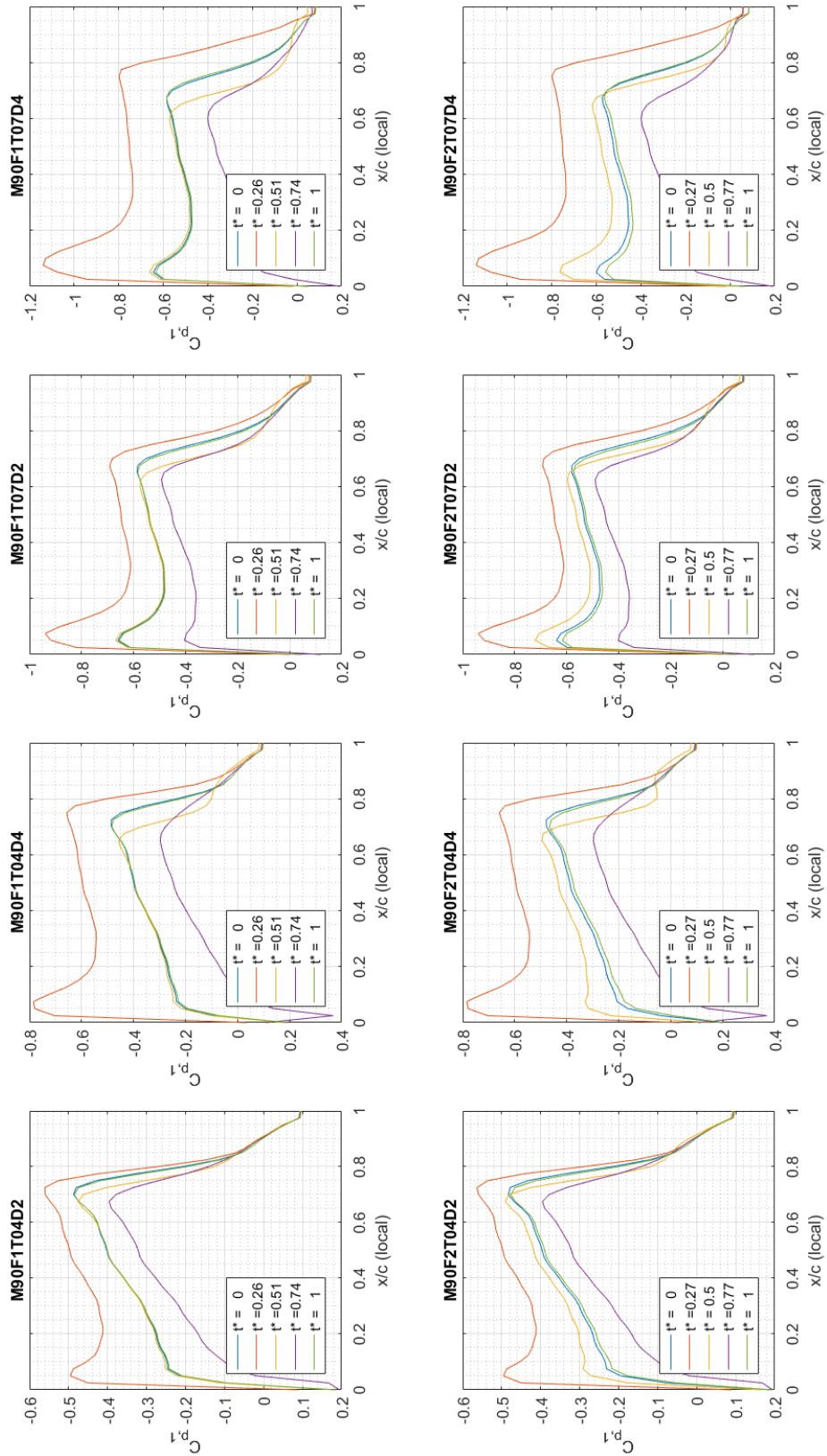


Figure A.1: Frequency Comparison. Time history of C_p for $M = 0.90$, Frequency = 5.7 Hz.

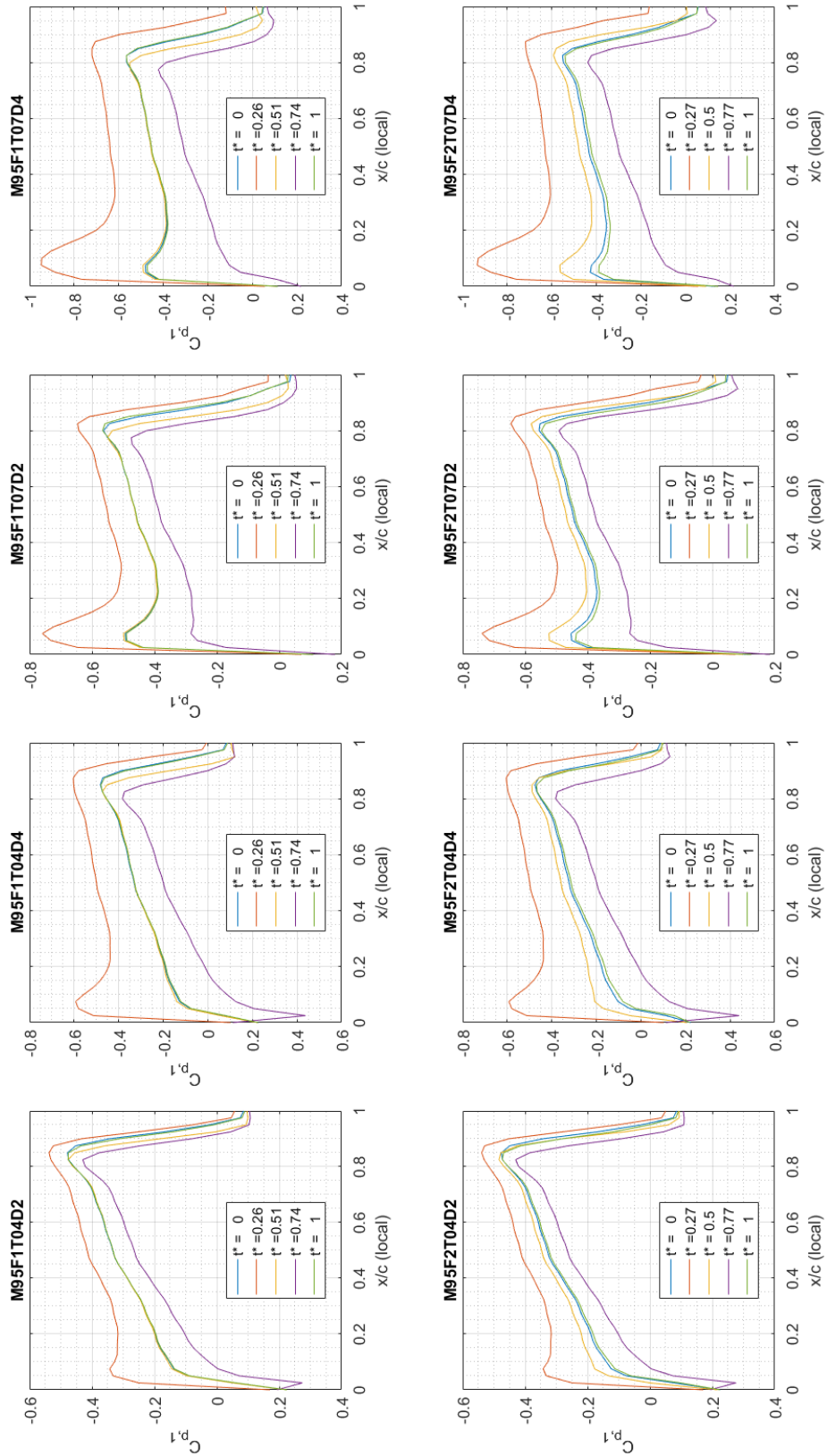


Figure A.2: Frequency Comparison. Time history of C_p for $M = 0.90$, Frequency = 7.4 Hz.

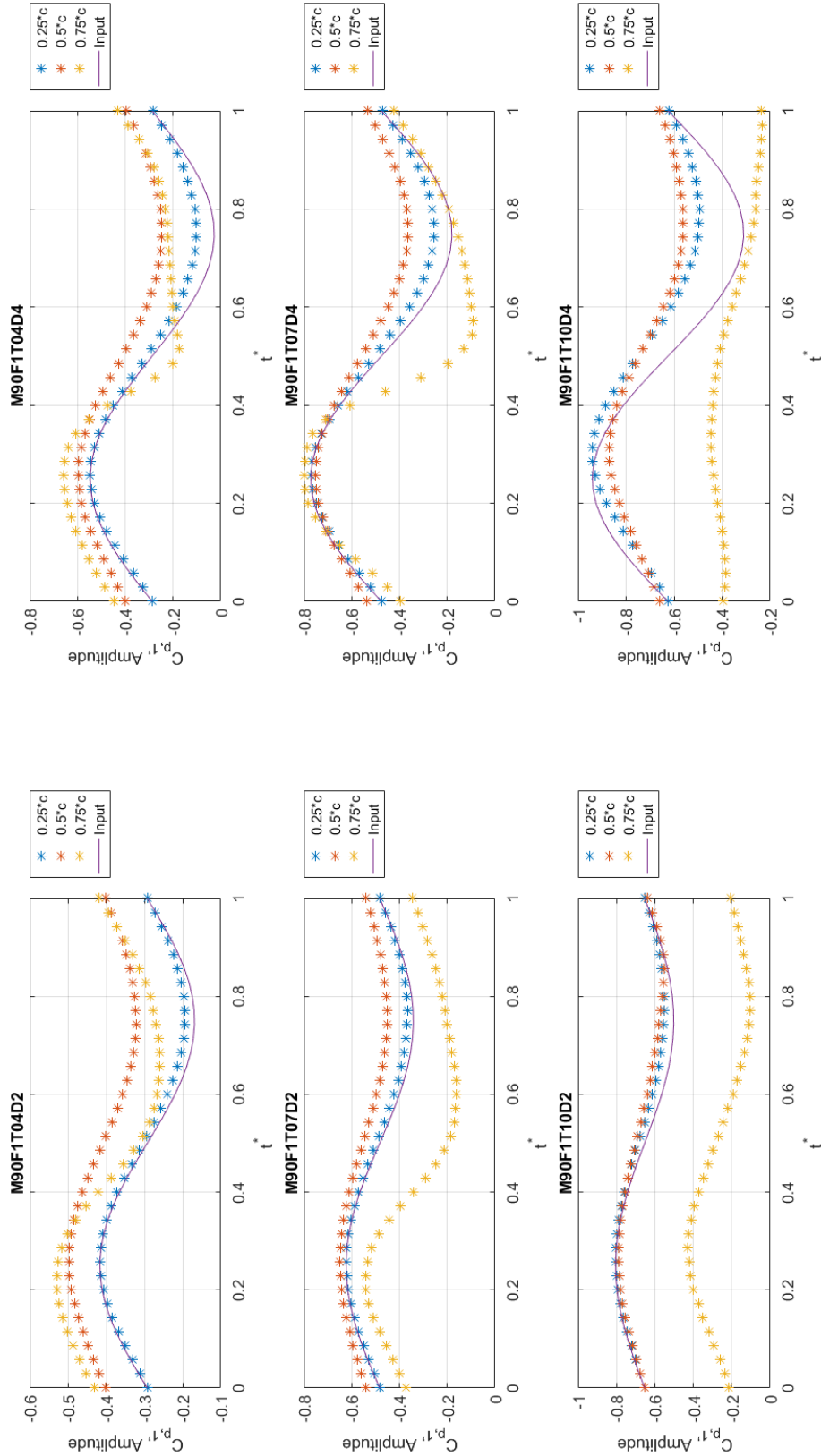


Figure A.3: Time history of C_p for for three points along the chord of station 1. $M = 0.90$, Frequency = 5.7 Hz.

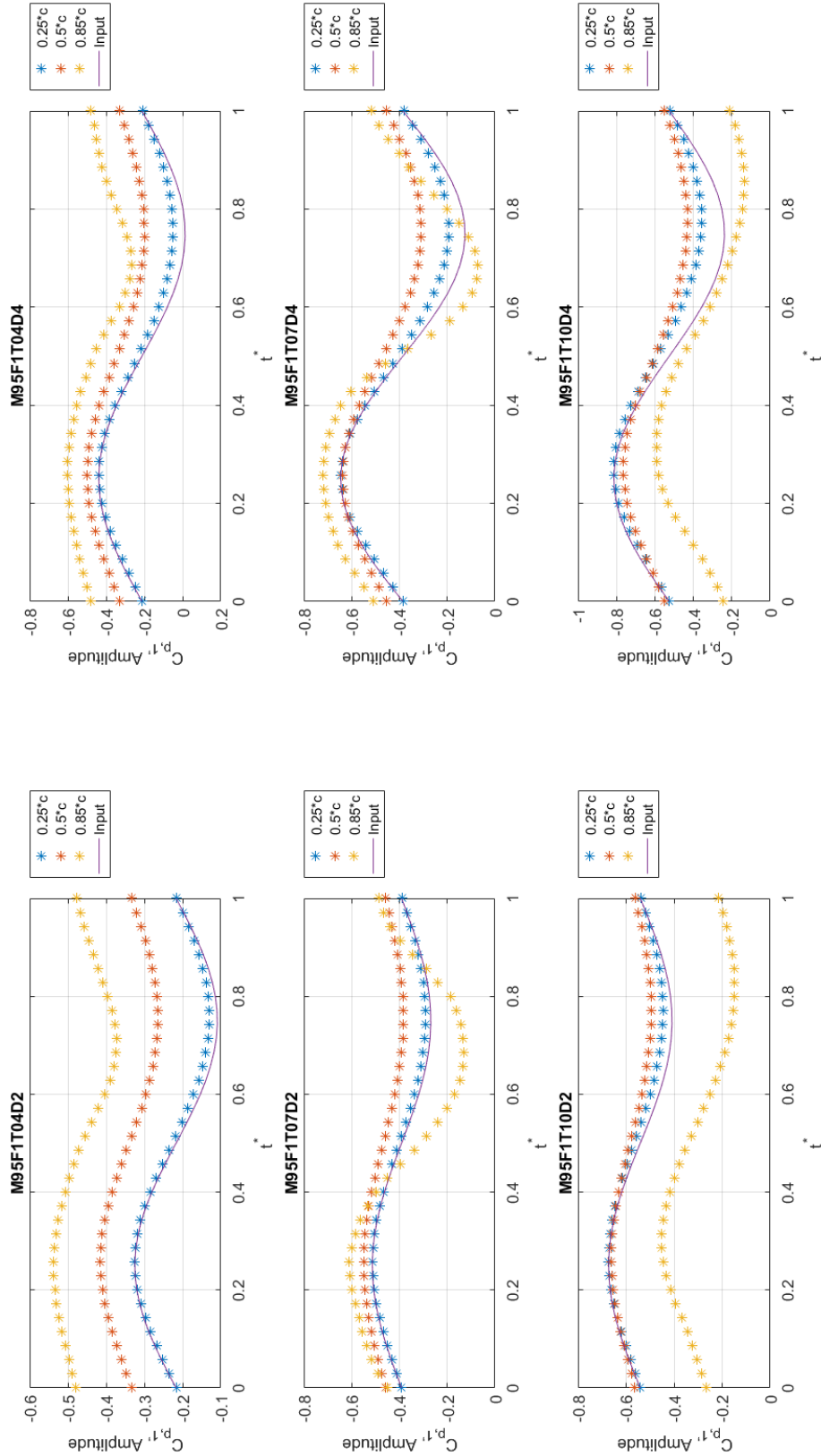


Figure A.4: Time history of C_p for for three points along the chord of station 1. $M = 0.95$, Frequency = 5.7 Hz.

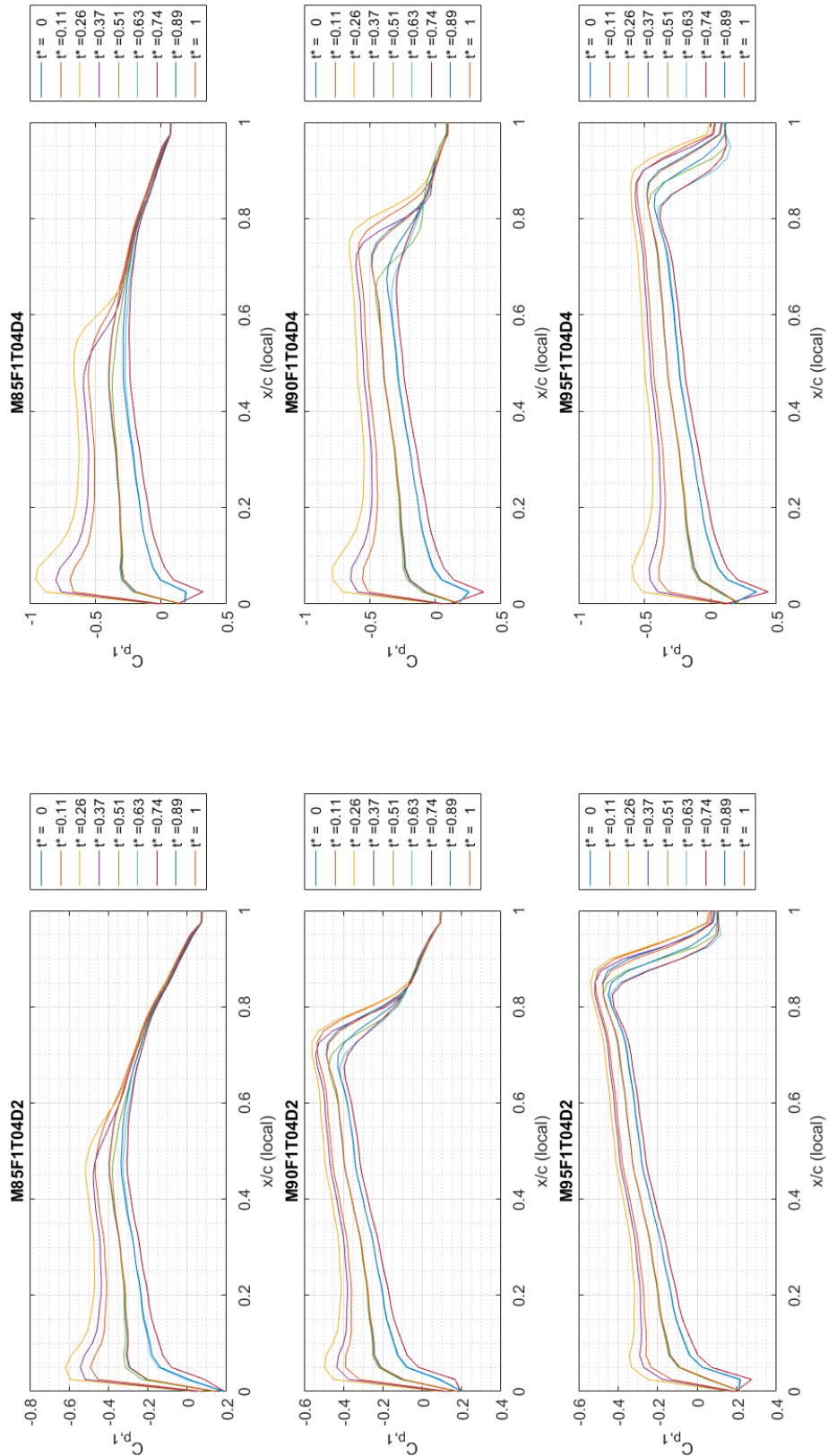


Figure A.5: Mach Comparison. Time history of C_p varying Mach number down the column. Frequency = 5.7 Hz, Trim = 4° .

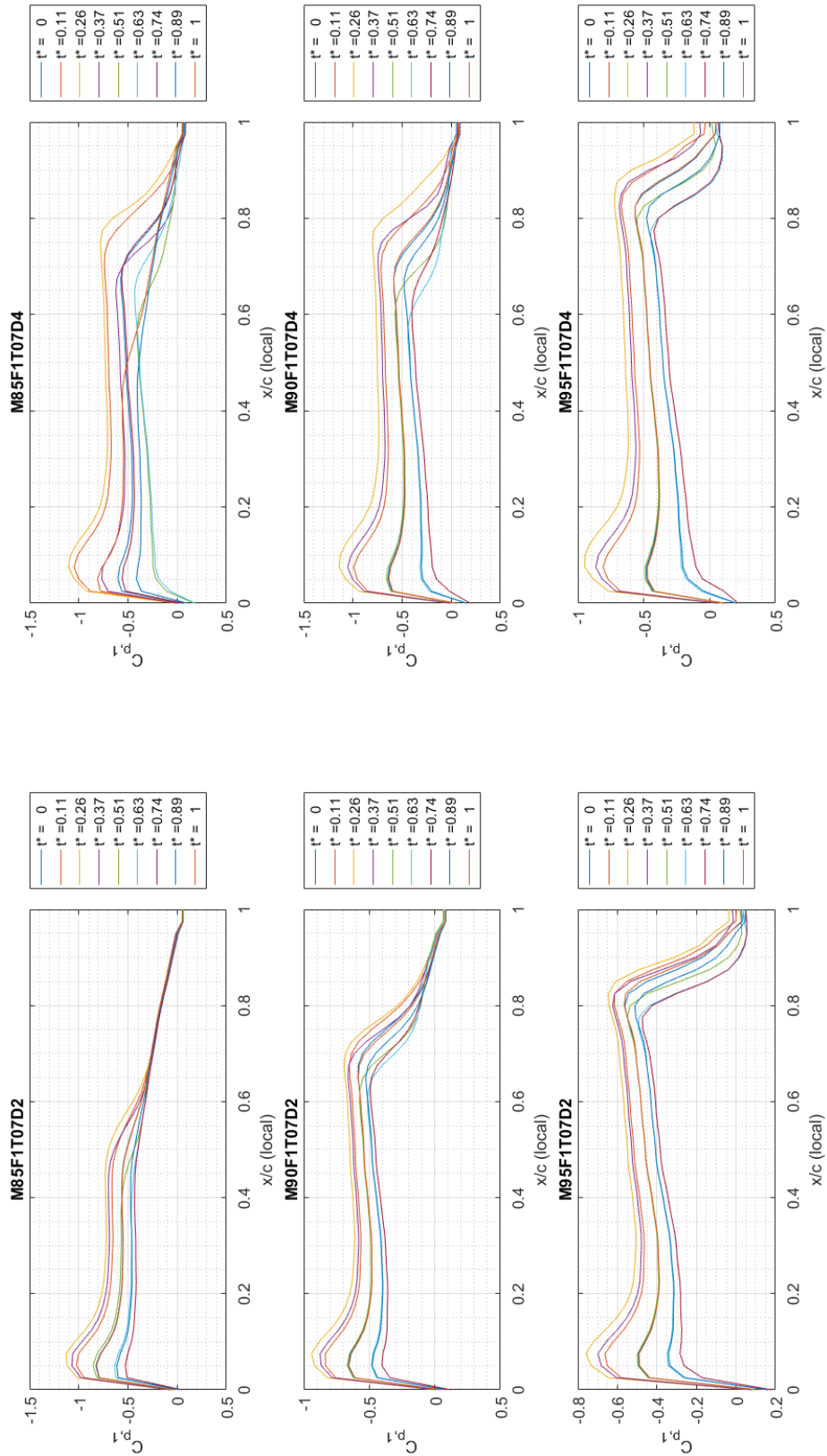


Figure A.6: Mach Comparison. Time history of C_p varying Mach number down the column. Frequency = 5.7 Hz, Trim = 7° .

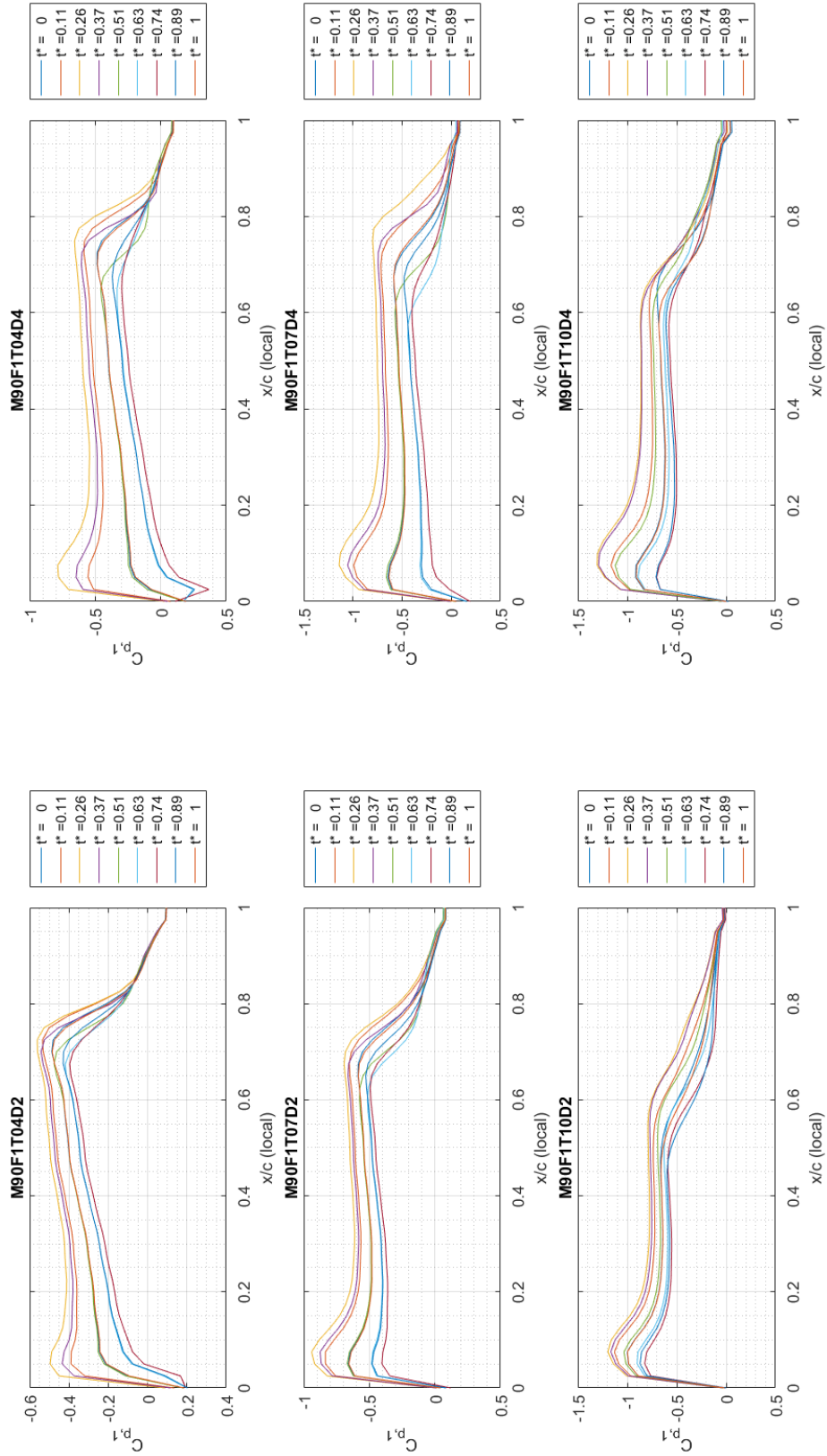


Figure A.7: BLC trim and $\Delta\alpha$ comparison of C_p . $M = 0.9$, Frequency = 5.7 Hz.

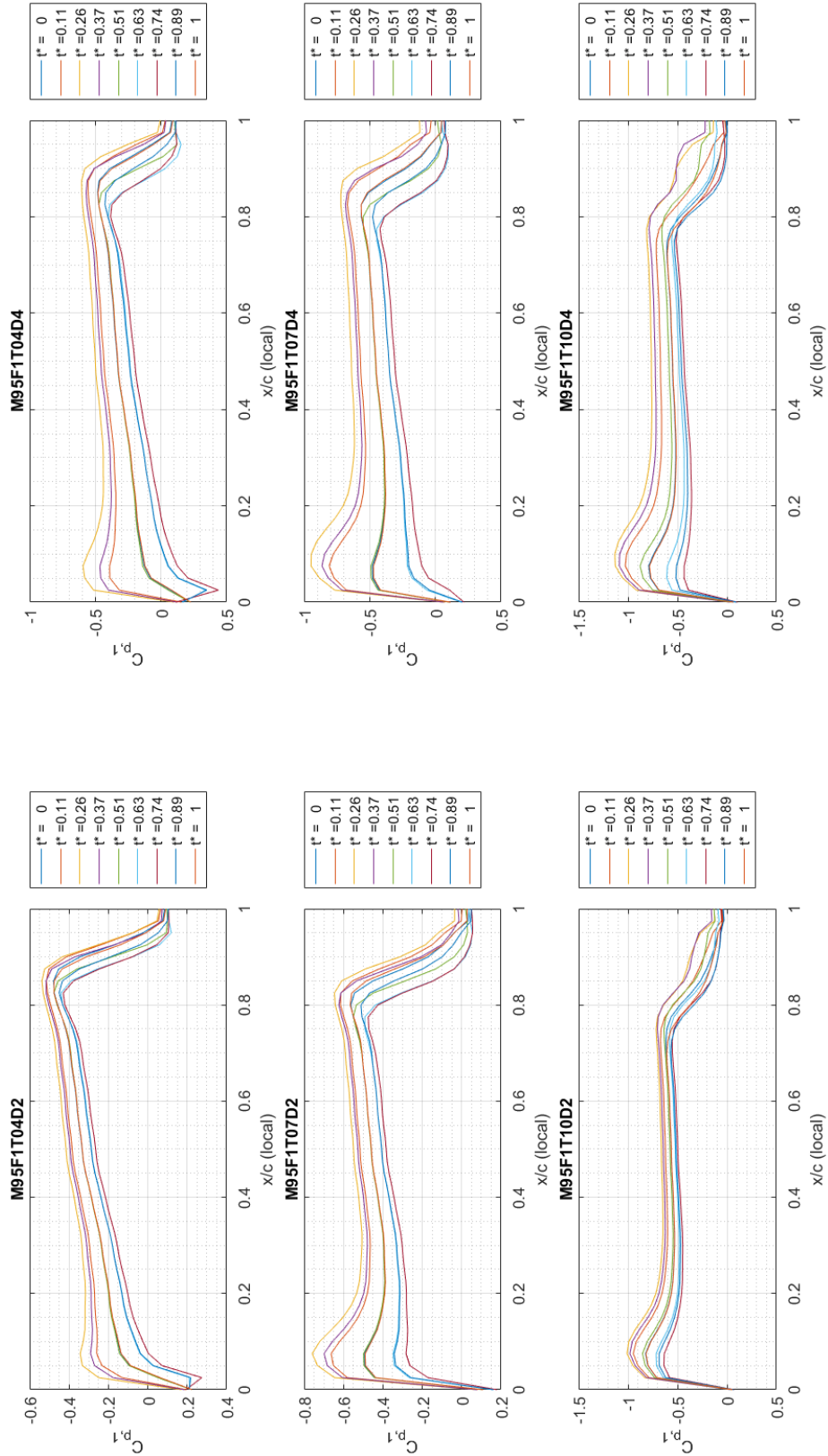


Figure A.8: BLC trim and $\Delta\alpha$ comparison of C_p . $M = 0.95$, Frequency = 5.7 Hz.

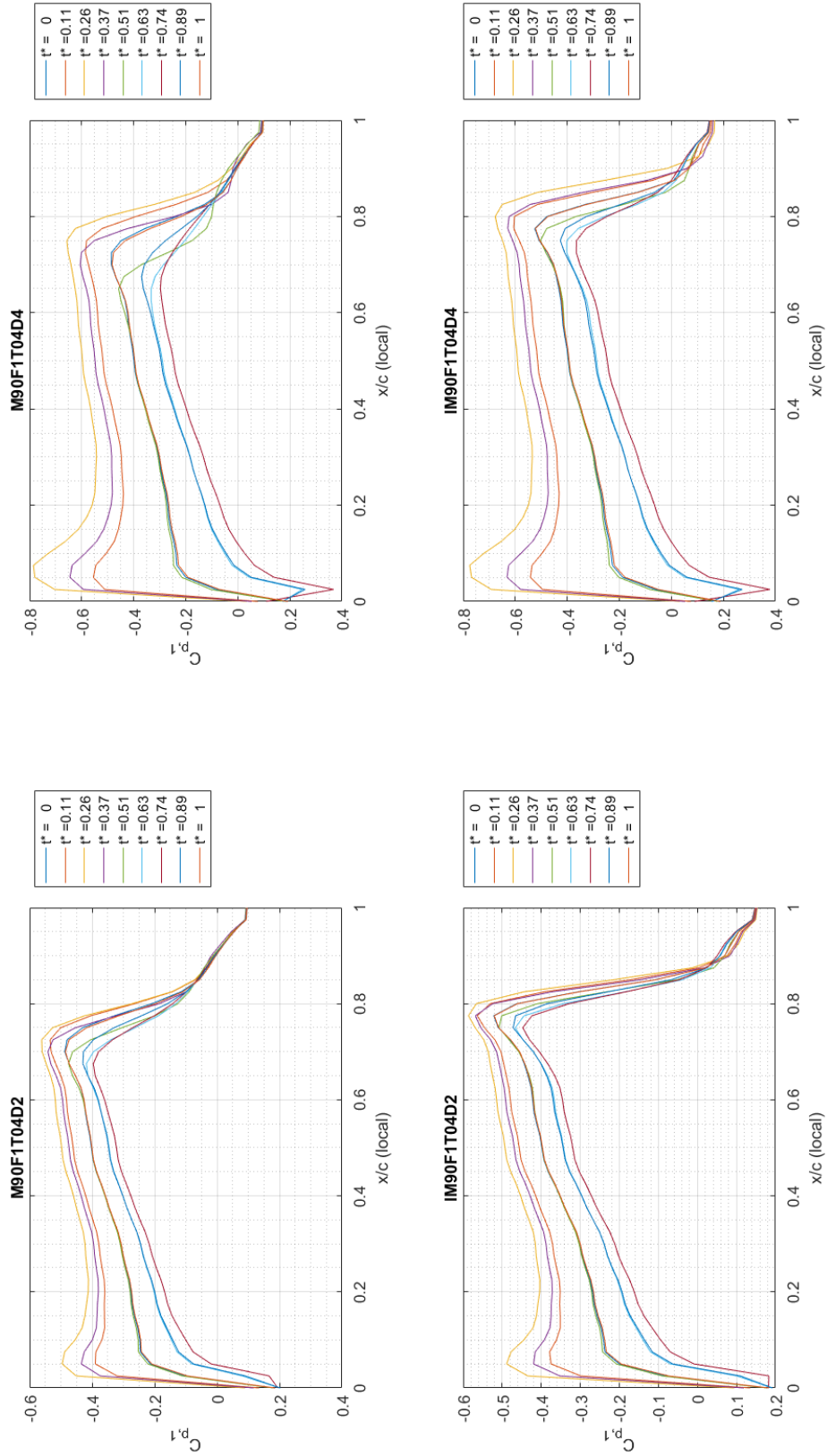


Figure A.9: Inviscid/Viscous comparison of C_p . $M = 0.9$, Frequency = 5.7 Hz, Trim $\alpha = 4^\circ$.

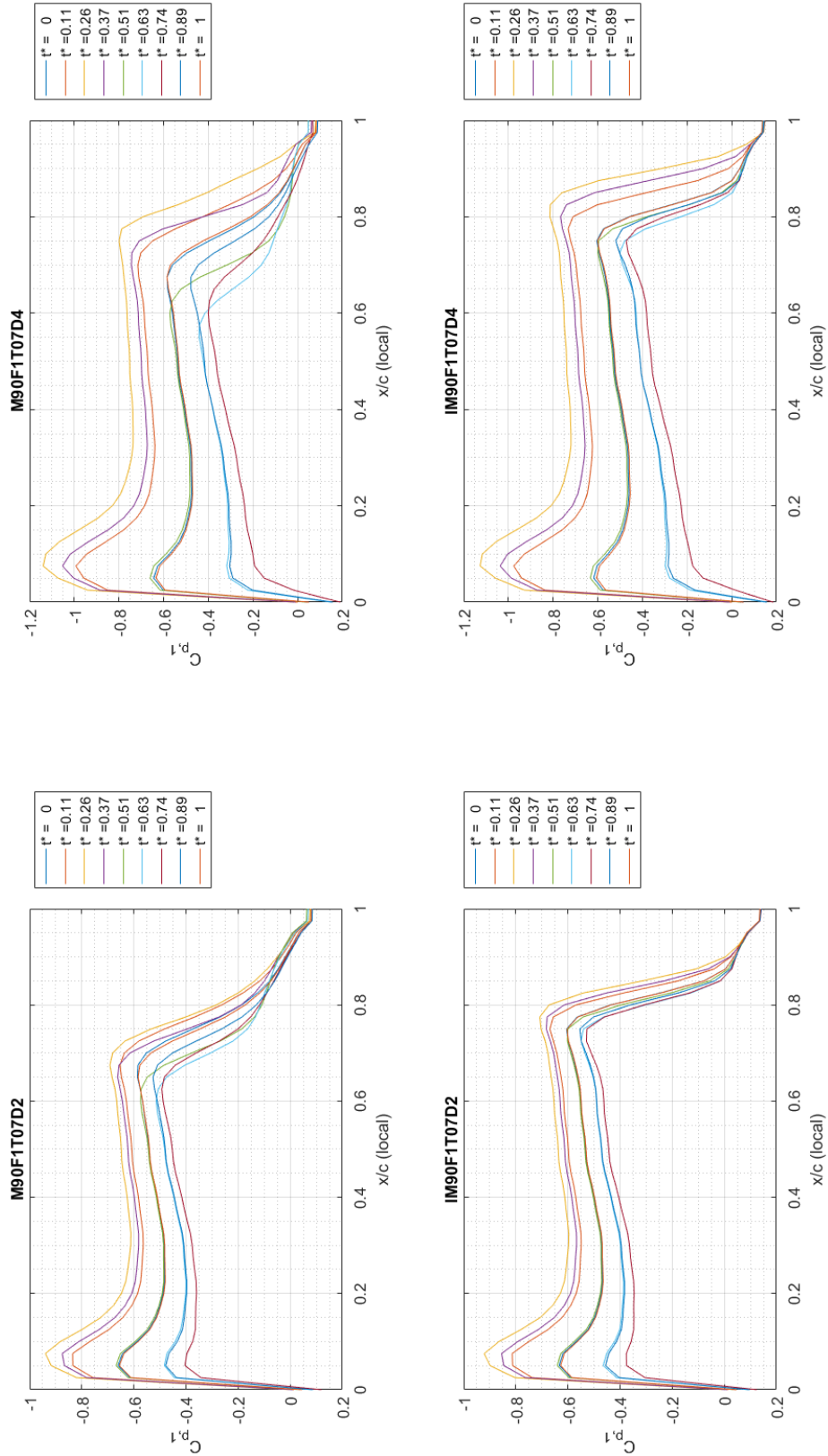


Figure A.10: Inviscid/Viscous comparison of C_p . $M = 0.9$, Frequency = 5.7 Hz, Trim $\alpha = 7^\circ$.

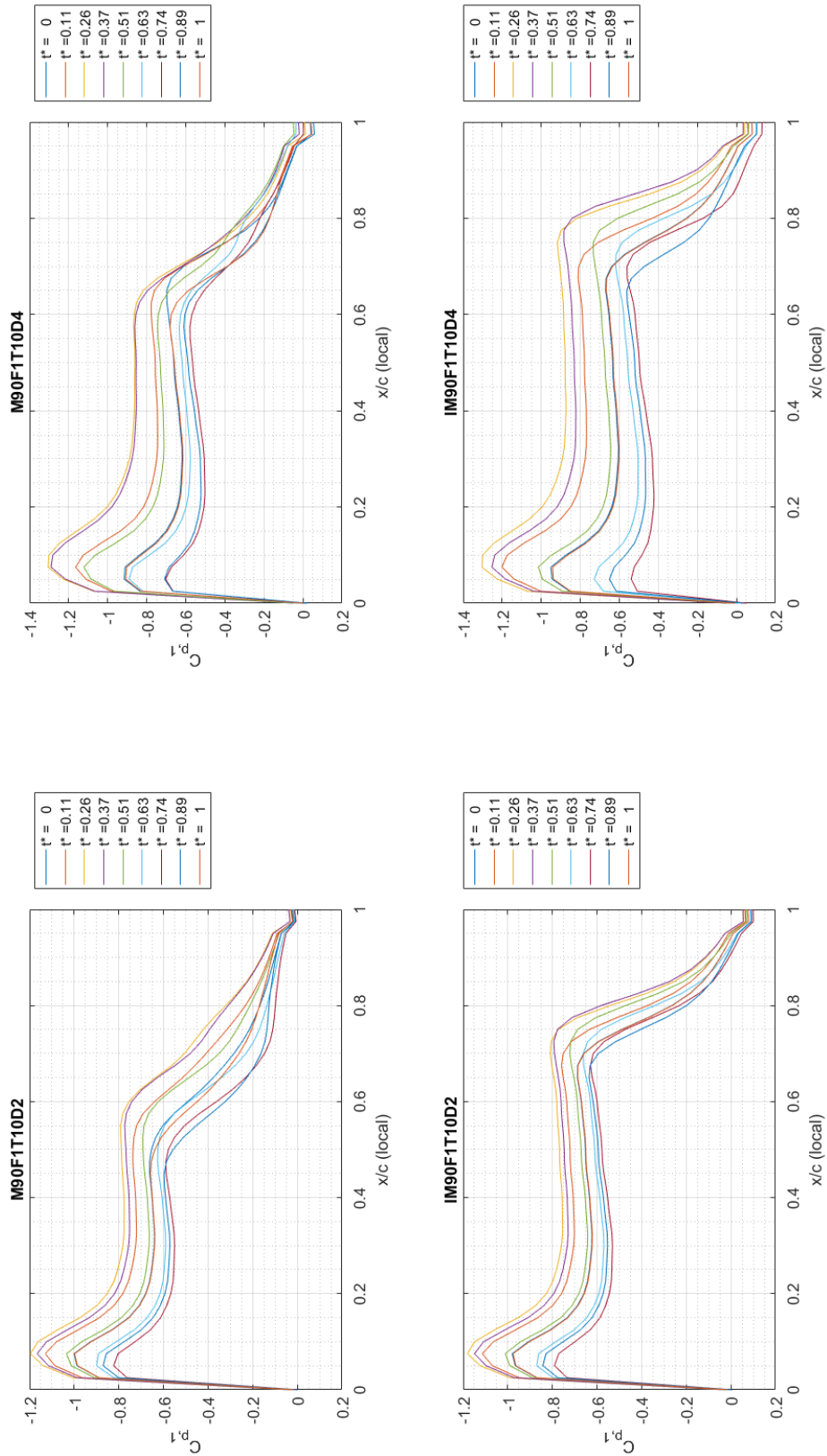


Figure A.11: Inviscid/Viscous comparison of C_p . $M = 0.9$, Frequency = 5.7 Hz, Trim = 10° .

Appendix B. C_p Data for Wing Station 2

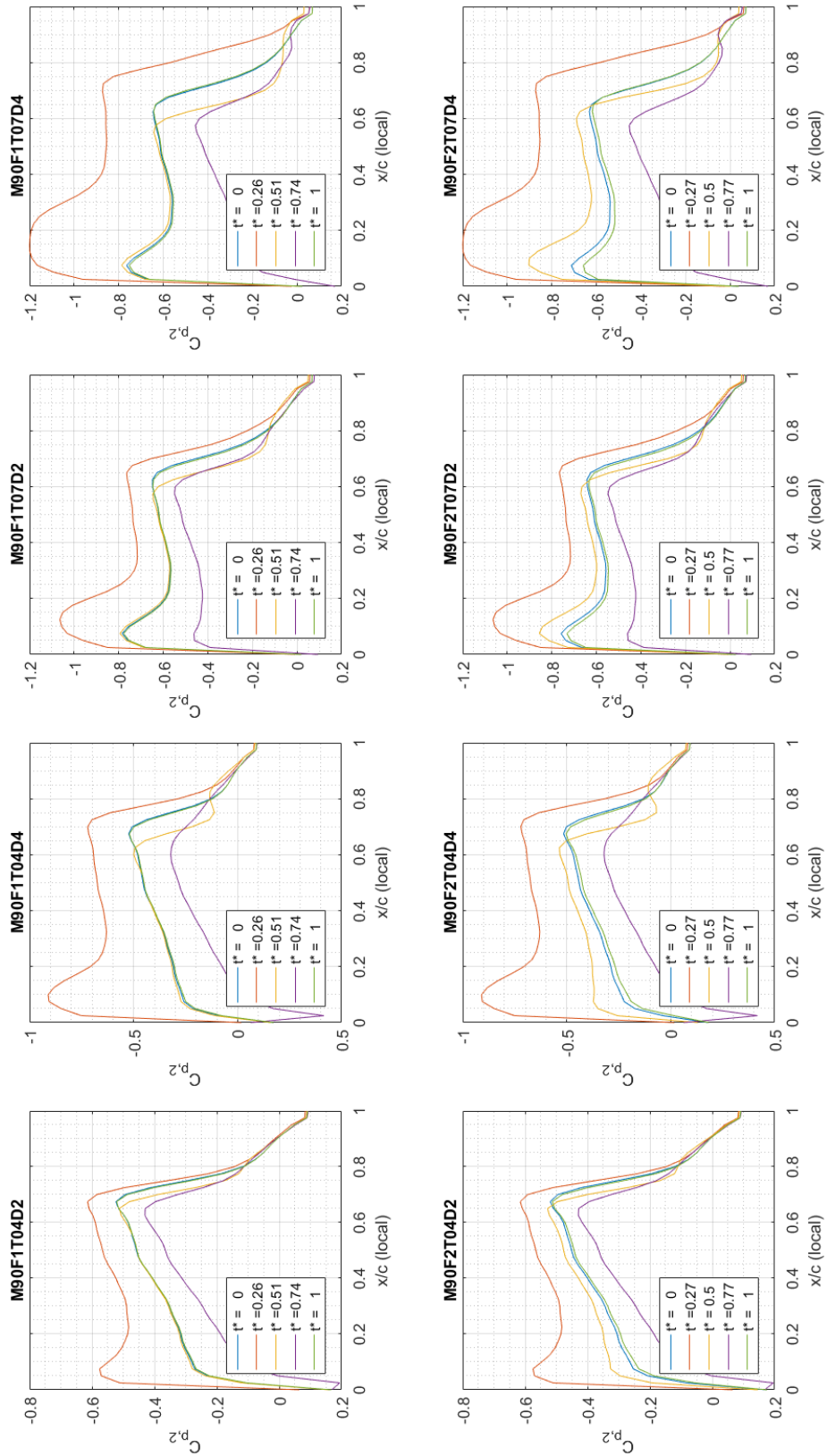


Figure B.1: Frequency Comparison. Time history of C_p for $M = 0.90$, Frequency = 5.7 Hz.

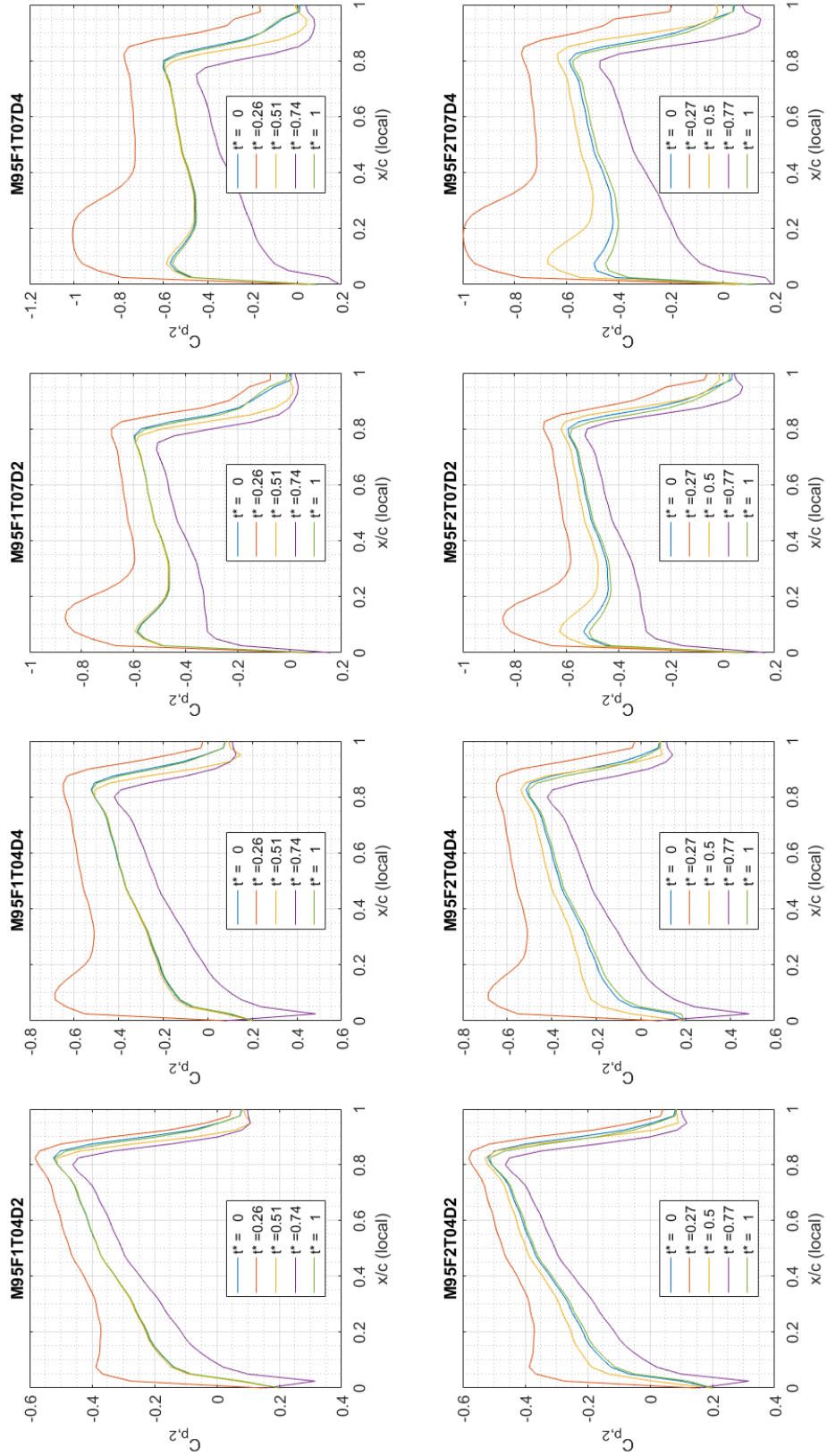


Figure B.2: Frequency Comparison. Time history of C_p for $M = 0.90$, Frequency = 7.4 Hz.

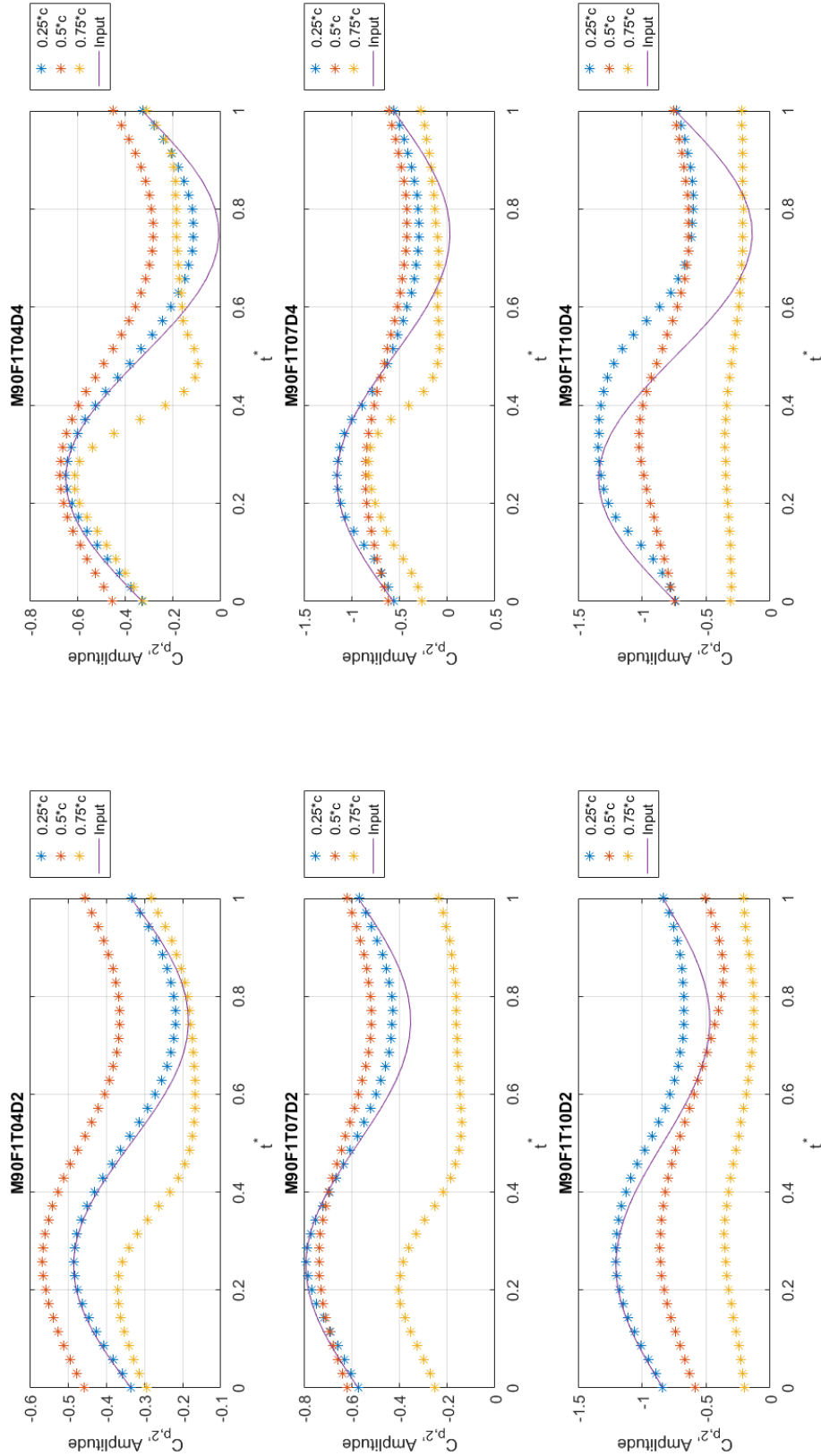


Figure B.3: Time history of C_p for for three points along the chord of station 2. $M = 0.90$, Frequency = 5.7 Hz.

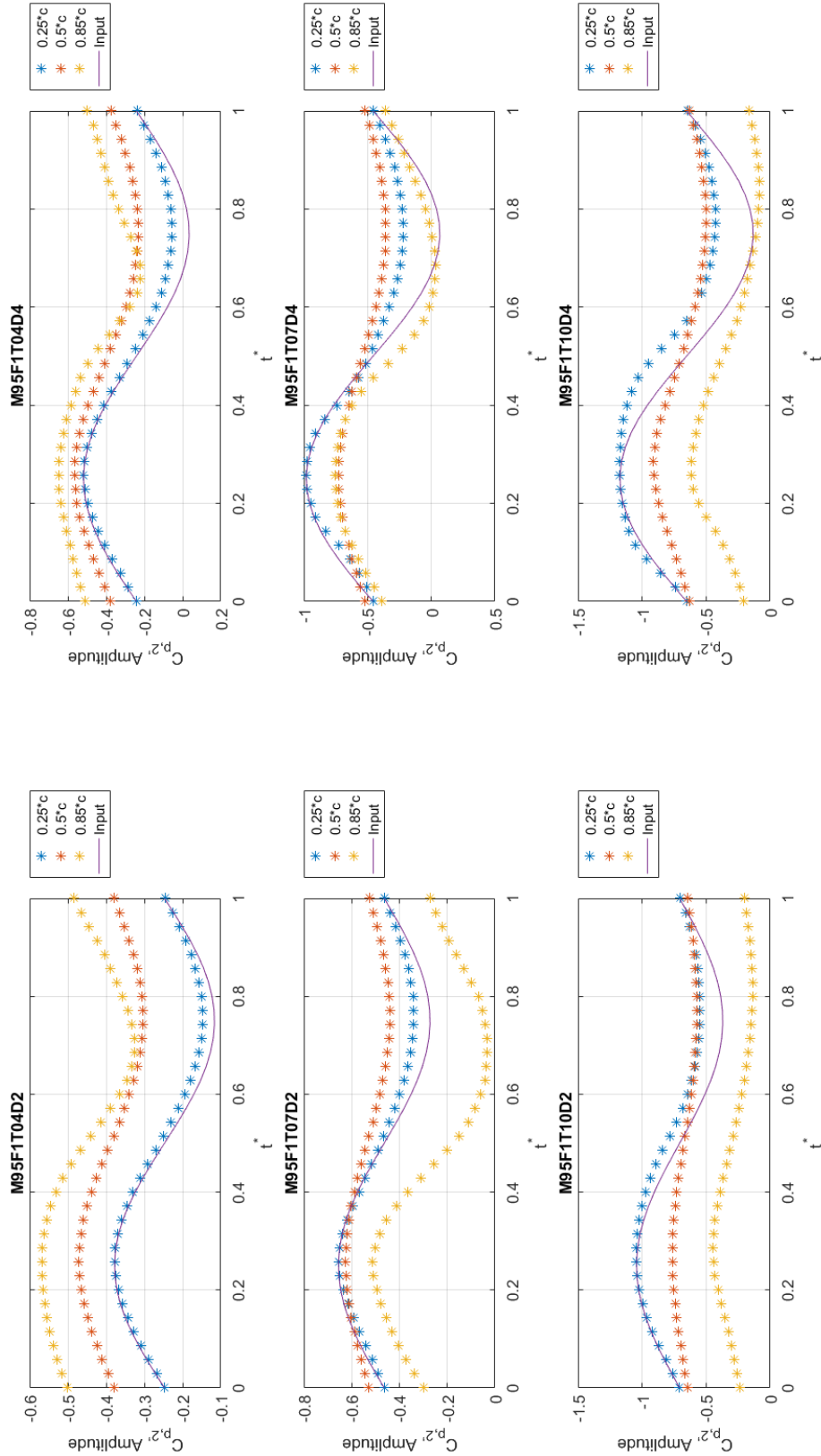


Figure B.4: Time history of C_p for for three points along the chord of station 2. $M = 0.95$, Frequency = 5.7 Hz.

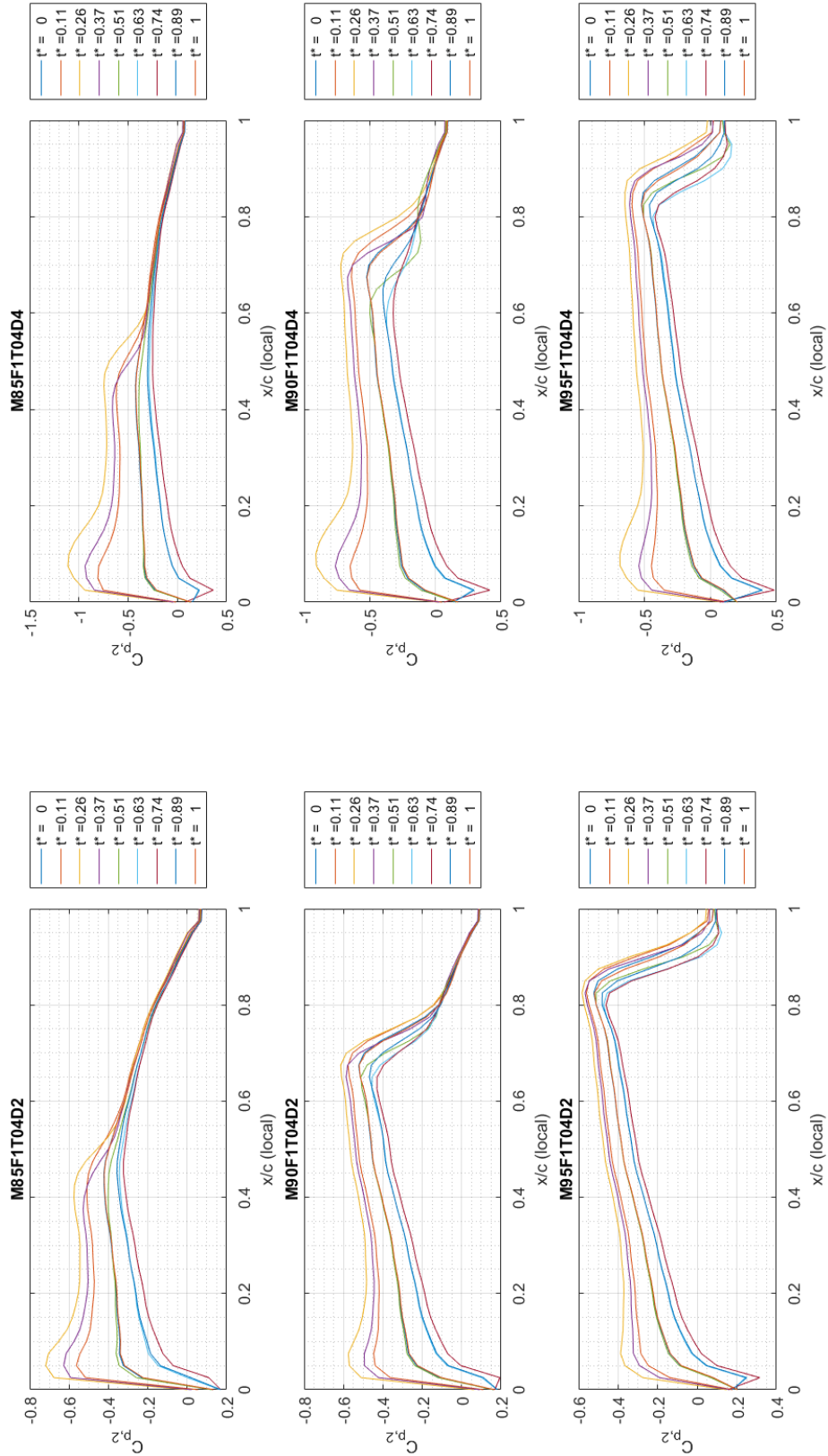


Figure B.5: Mach Comparison. Time history of C_p varying Mach number down the column. Frequency = 5.7 Hz, Trim = 4° .

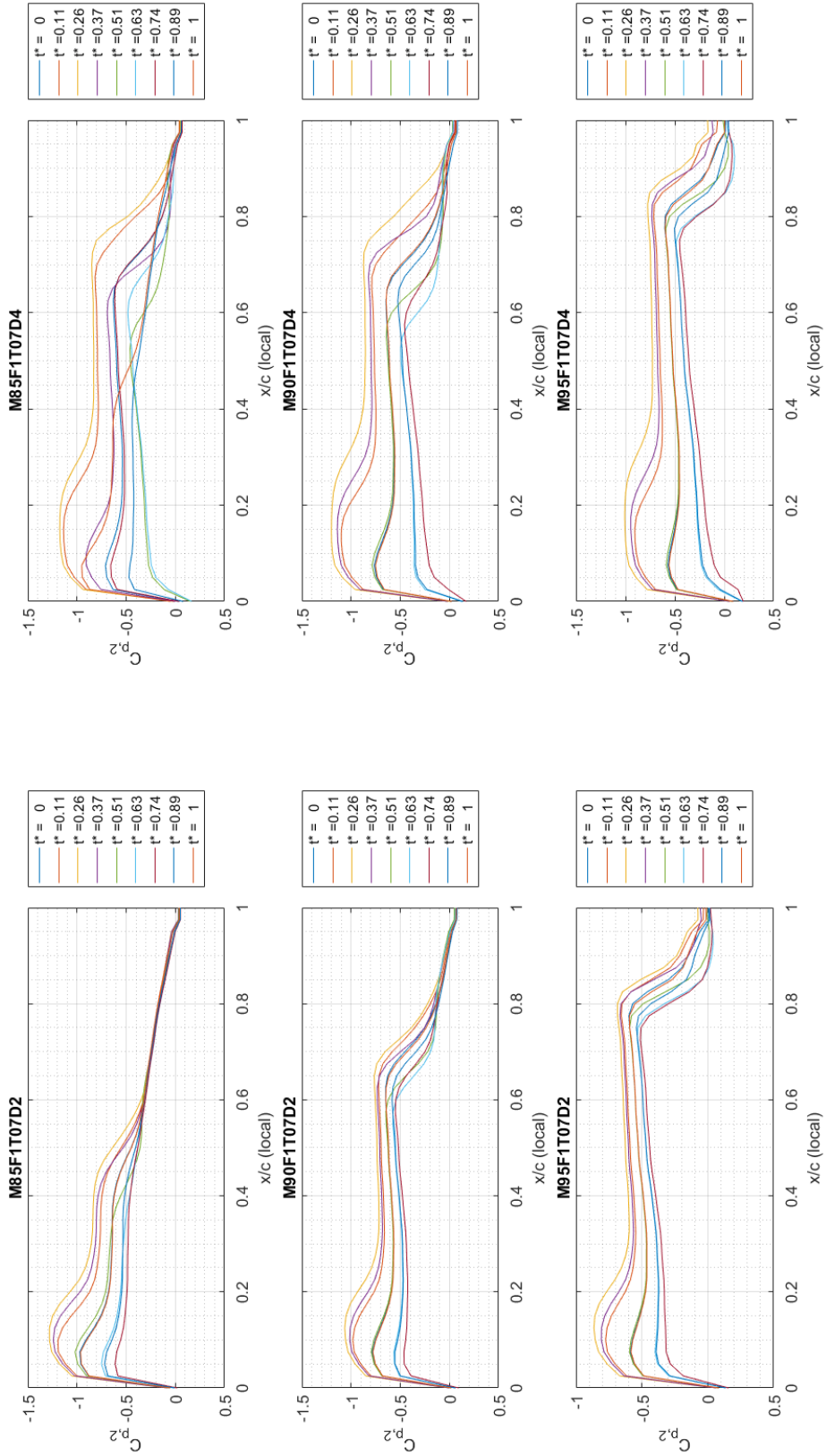


Figure B.6: Mach Comparison. Time history of C_p varying Mach number down the column. Frequency = 5.7 Hz, Trim = 7°.

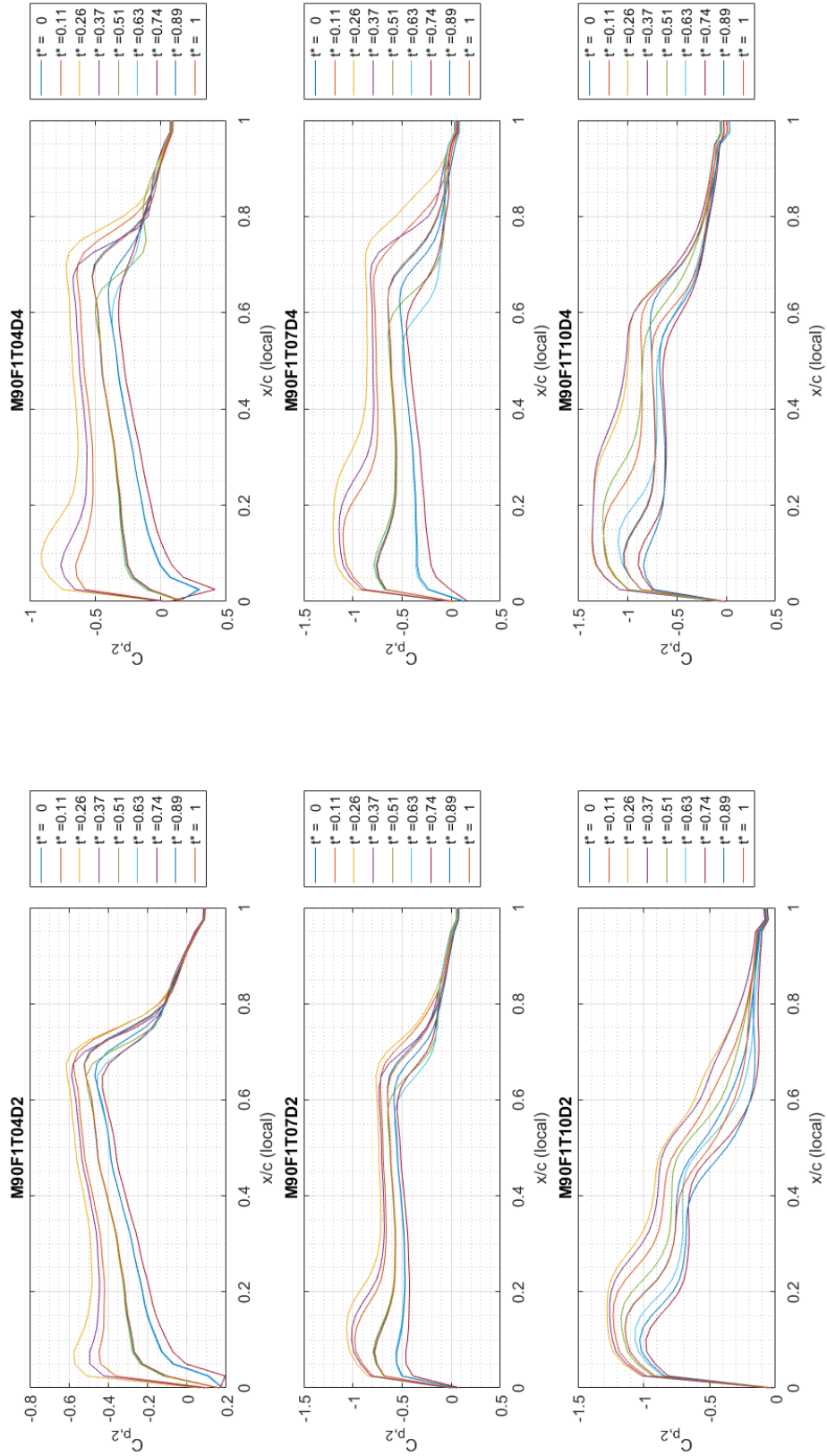


Figure B.7: BLC trim and $\Delta\alpha$ comparison of C_p . $M = 0.9$, Frequency = 5.7 Hz.

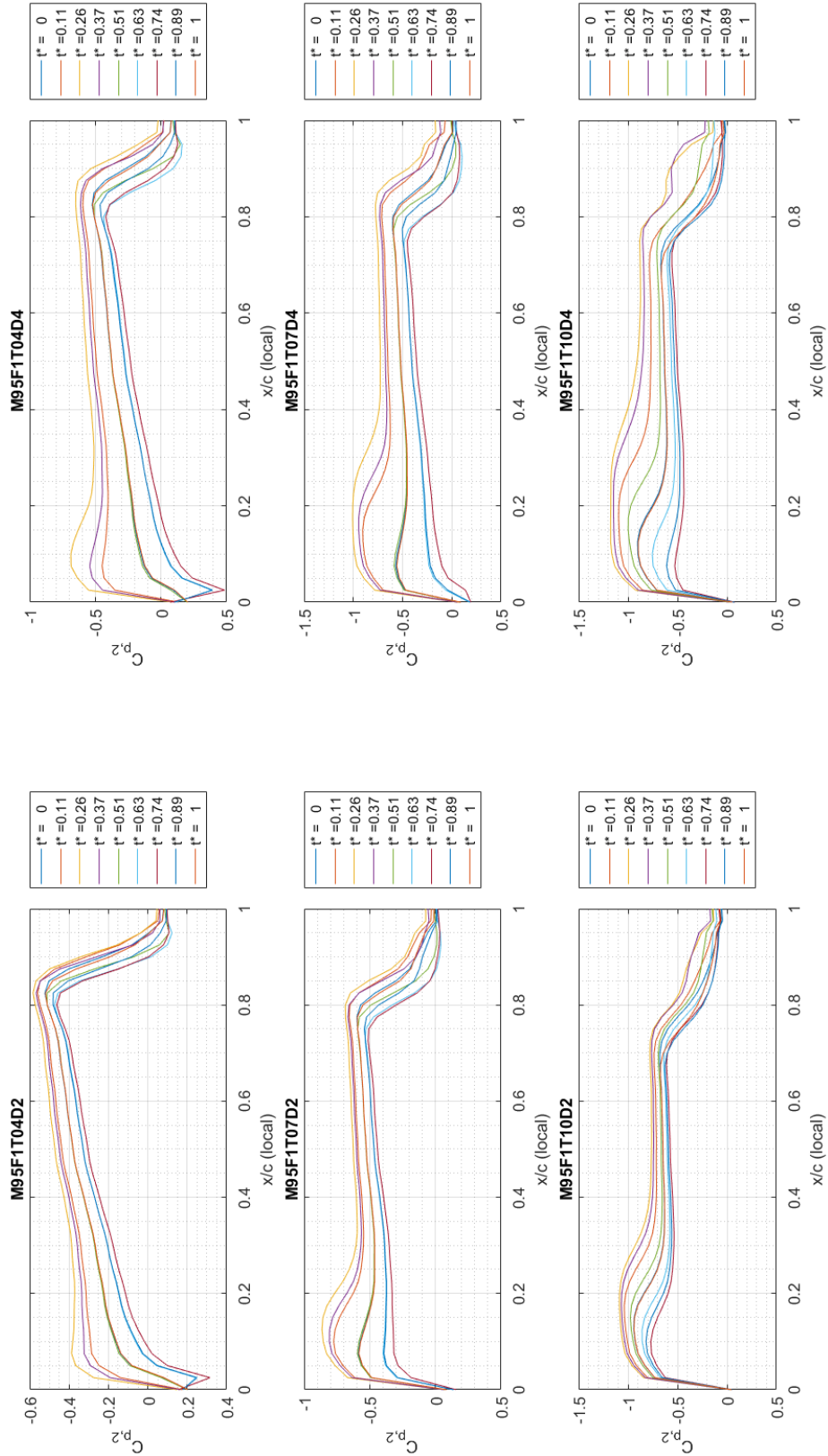


Figure B.8: BLC trim and $\Delta\alpha$ comparison of C_p . $M = 0.95$, Frequency = 5.7 Hz.

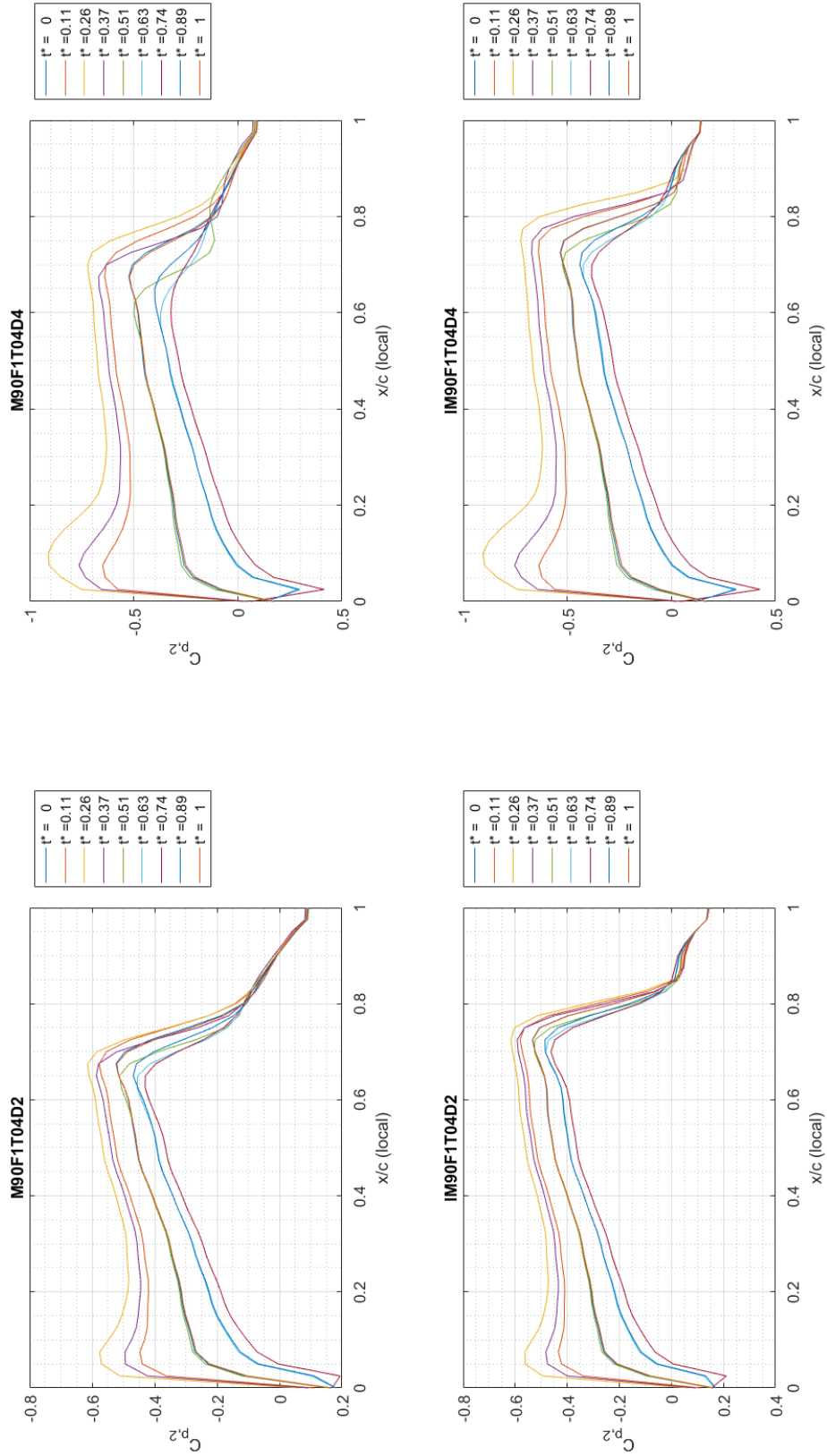


Figure B.9: Inviscid/Viscous comparison of C_p . $M = 0.9$, Frequency = 5.7 Hz, Trim $\alpha = 4^\circ$.

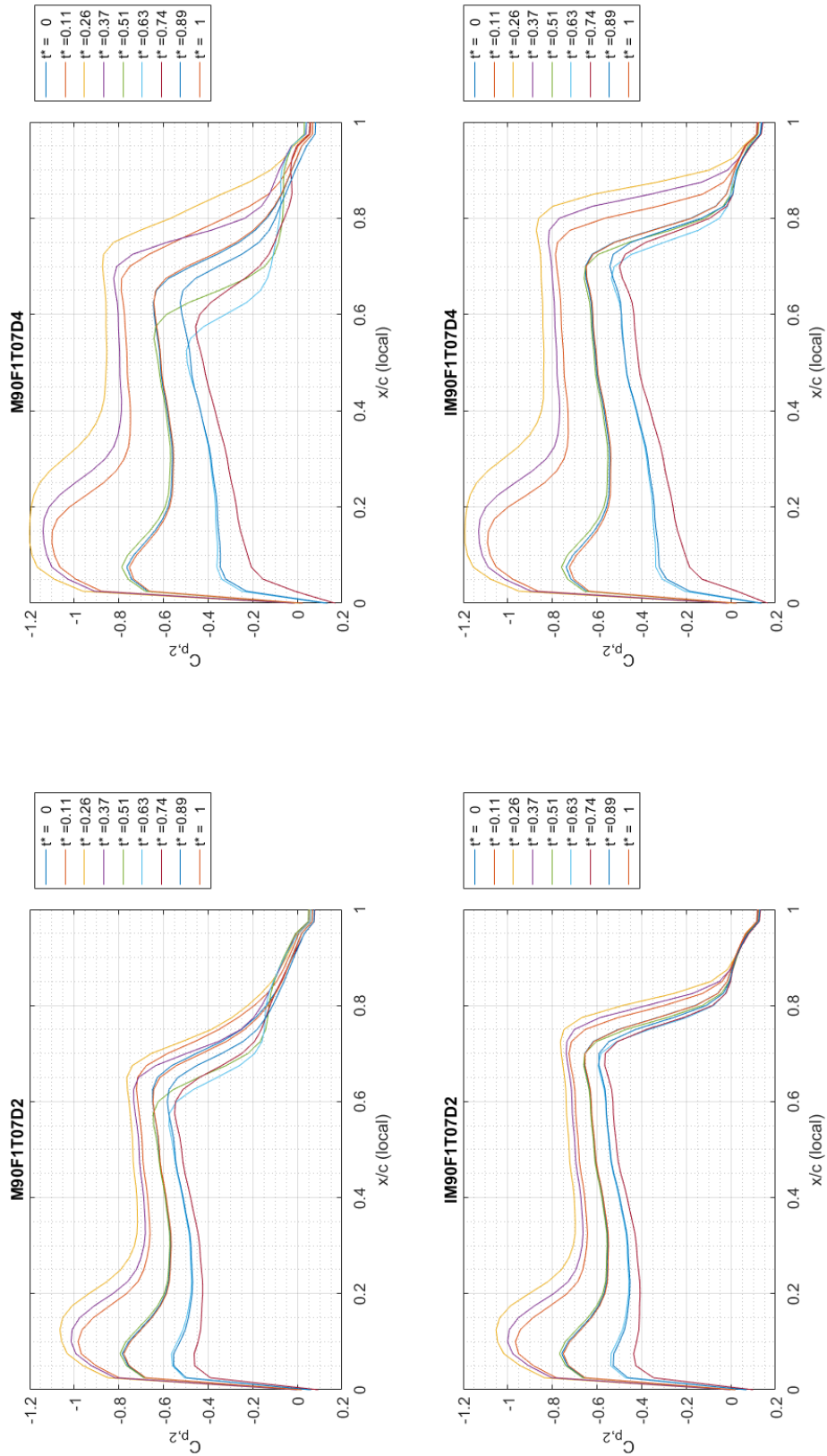


Figure B.10: Inviscid/Viscous comparison of C_p . $M = 0.9$, Frequency = 5.7 Hz, Trim $\alpha = 7^\circ$.

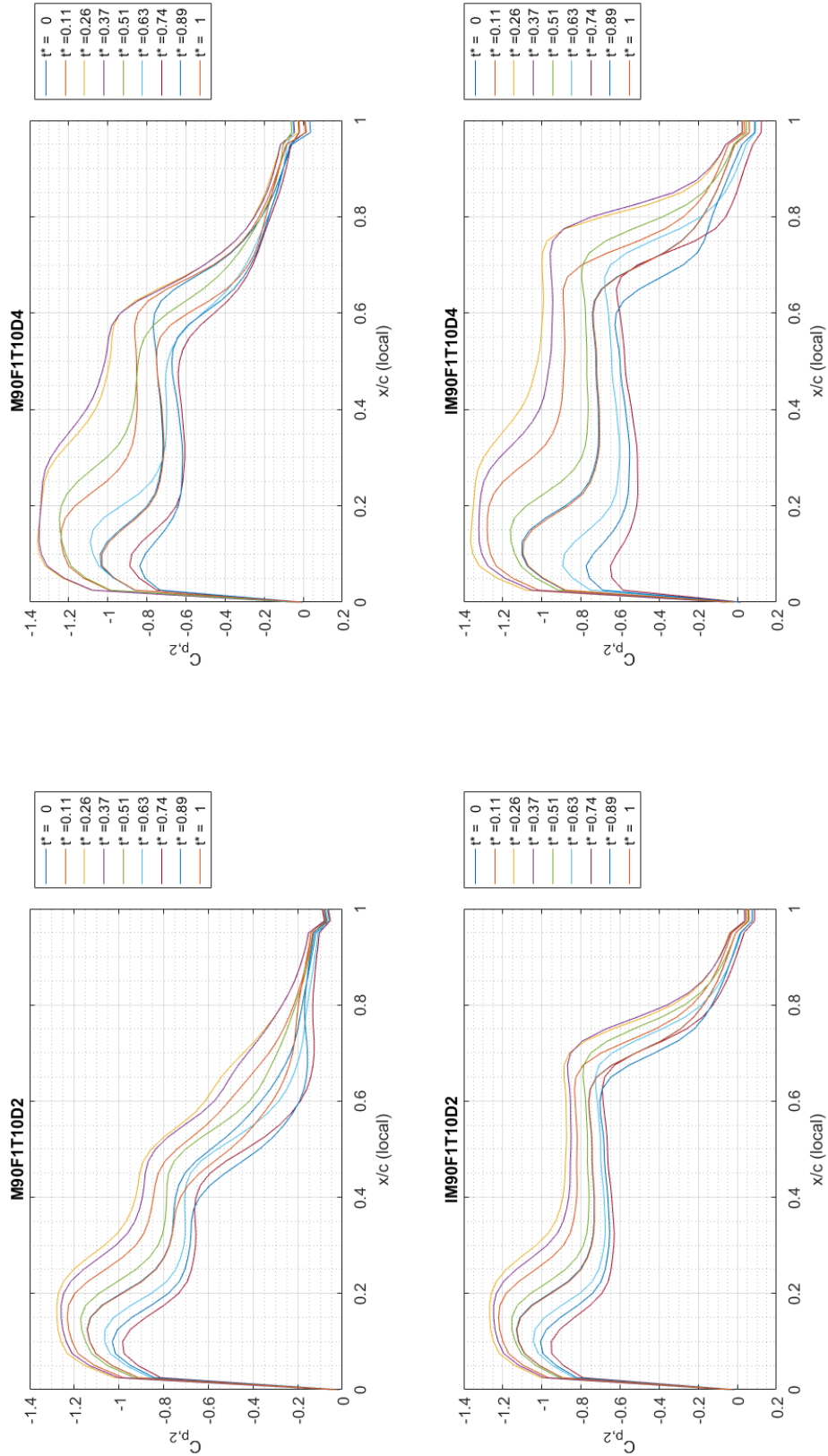


Figure B.11: Inviscid/Viscous comparison of C_p . $M = 0.9$, Frequency = 5.7 Hz, Trim $\alpha = 10^\circ$.

Appendix C. C_p Data for Wing Station 3

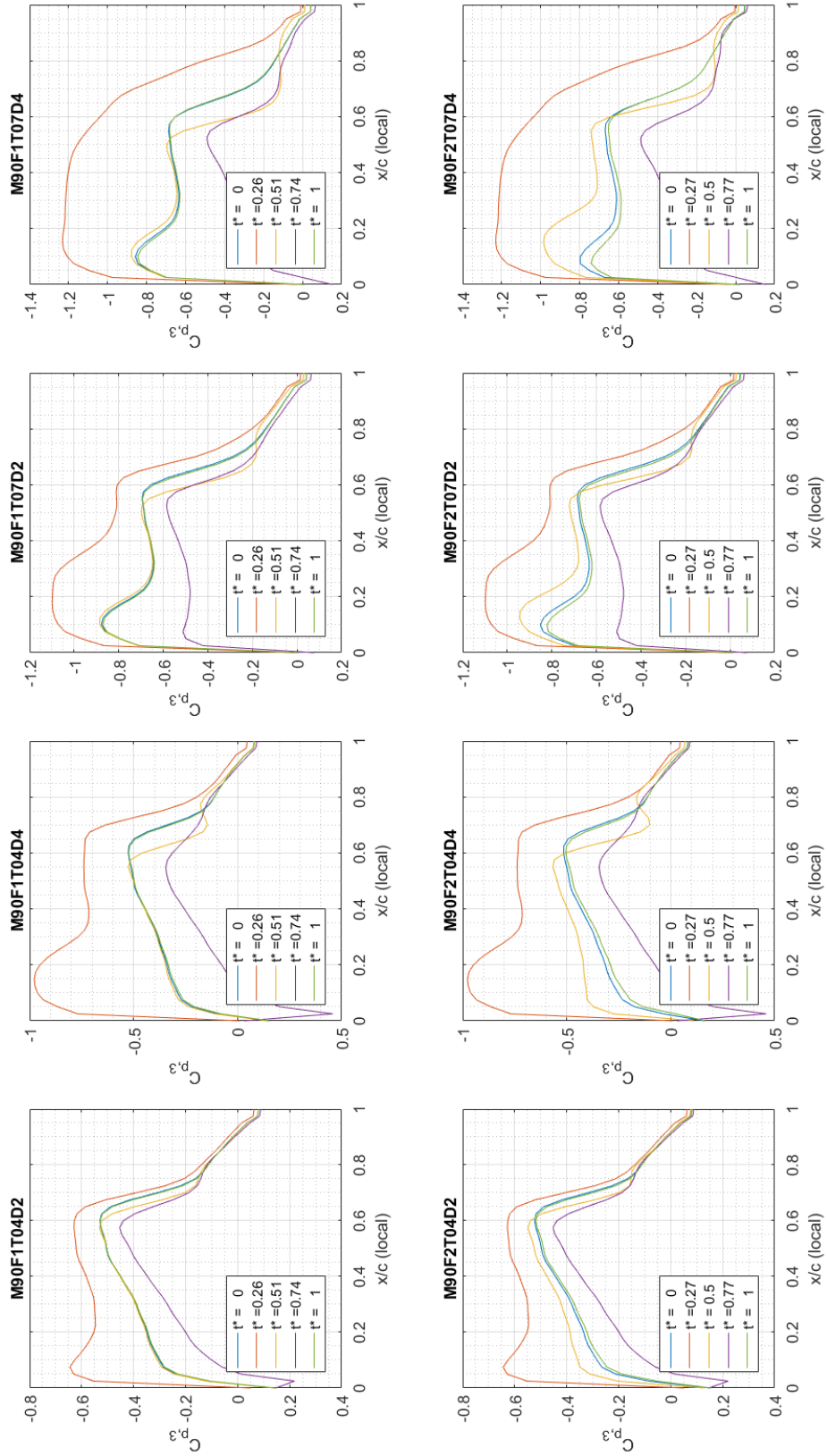


Figure C.1: Frequency Comparison. Time history of C_p for $M = 0.90$, Frequency = 5.7 Hz.

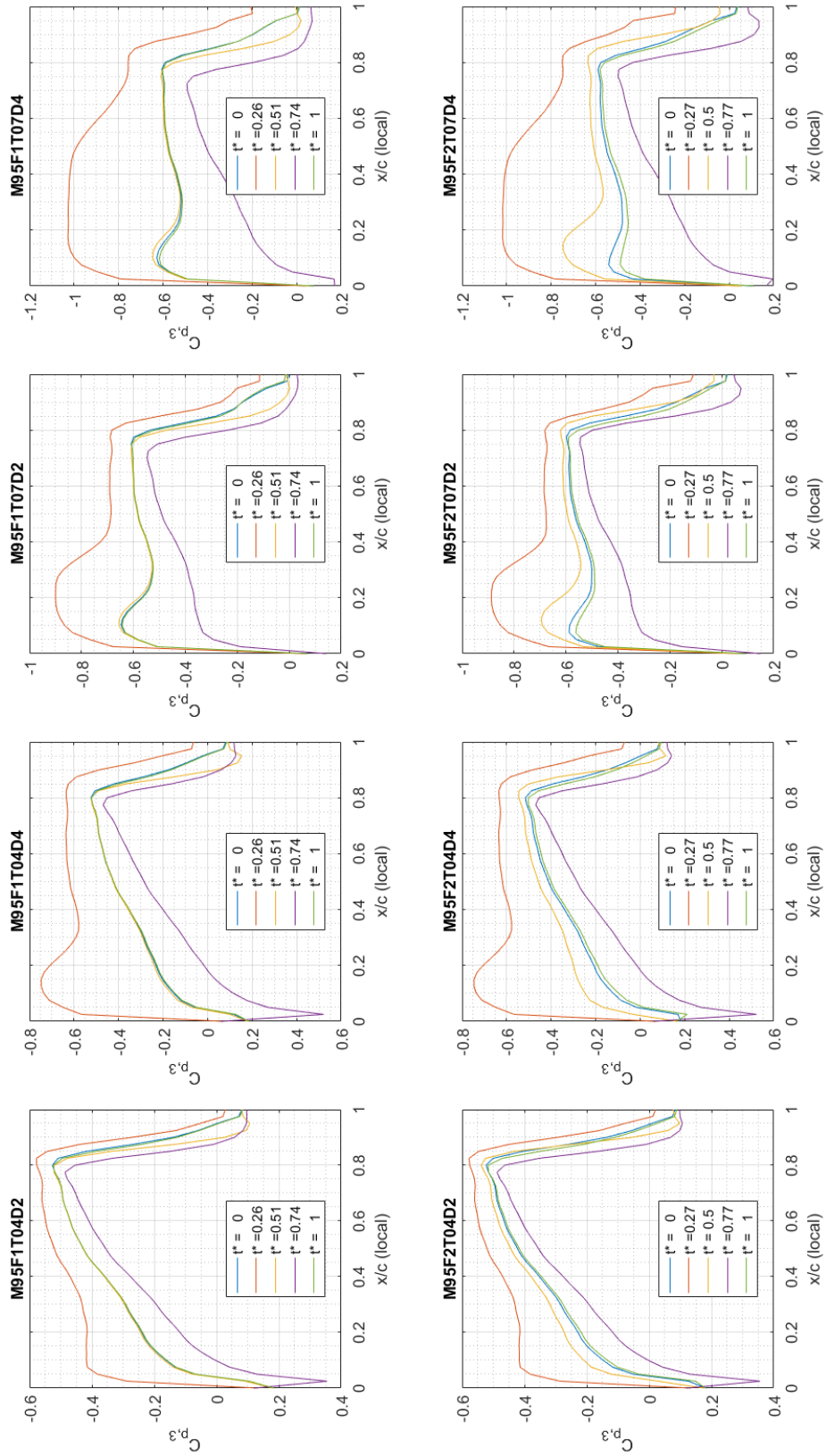


Figure C.2: Frequency Comparison. Time history of C_p for $M = 0.90$, Frequency = 7.4 Hz.

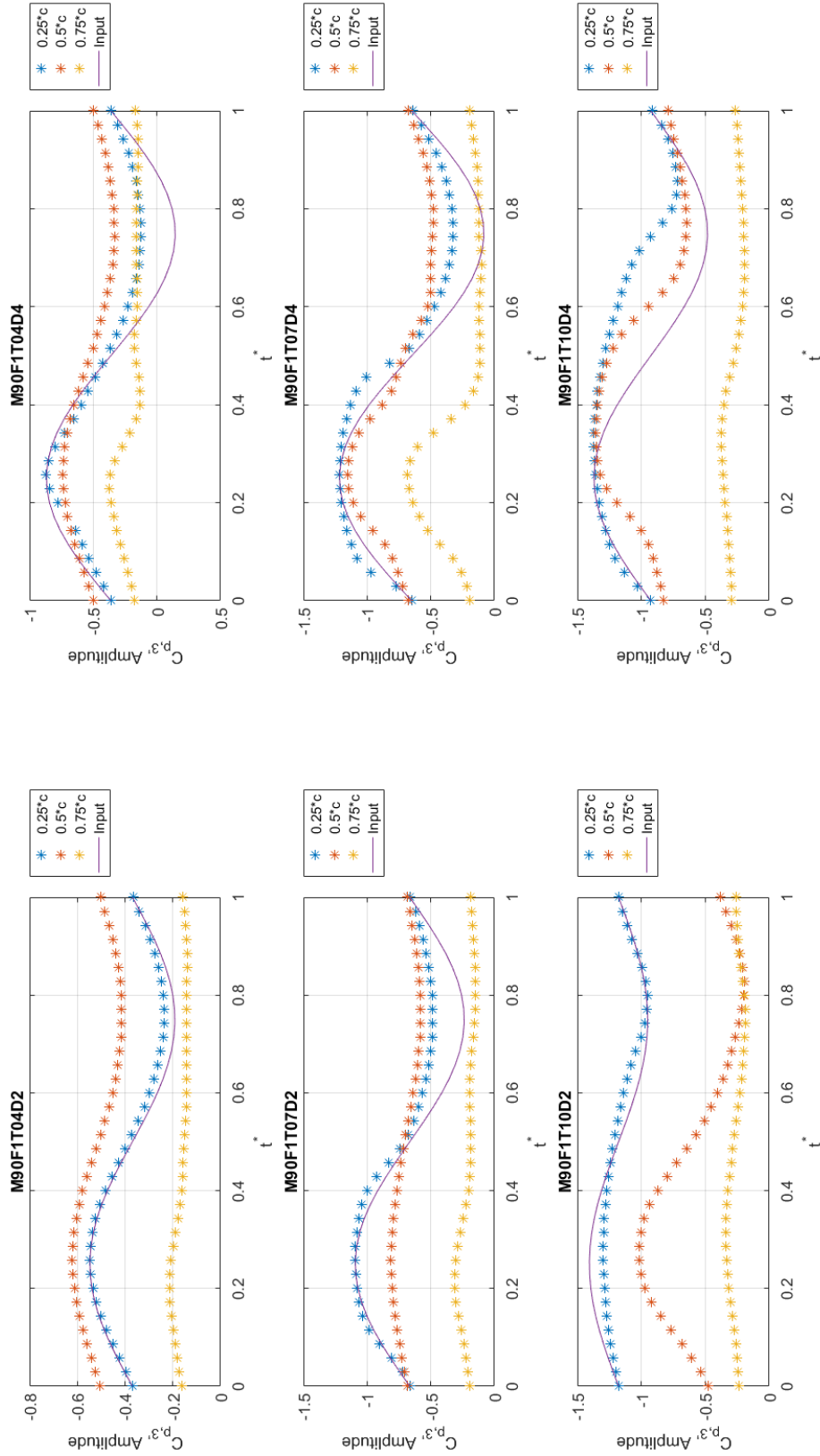


Figure C.3: Time history of C_p for for three points along the chord of station 3. $M = 0.90$, Frequency = 5.7 Hz.

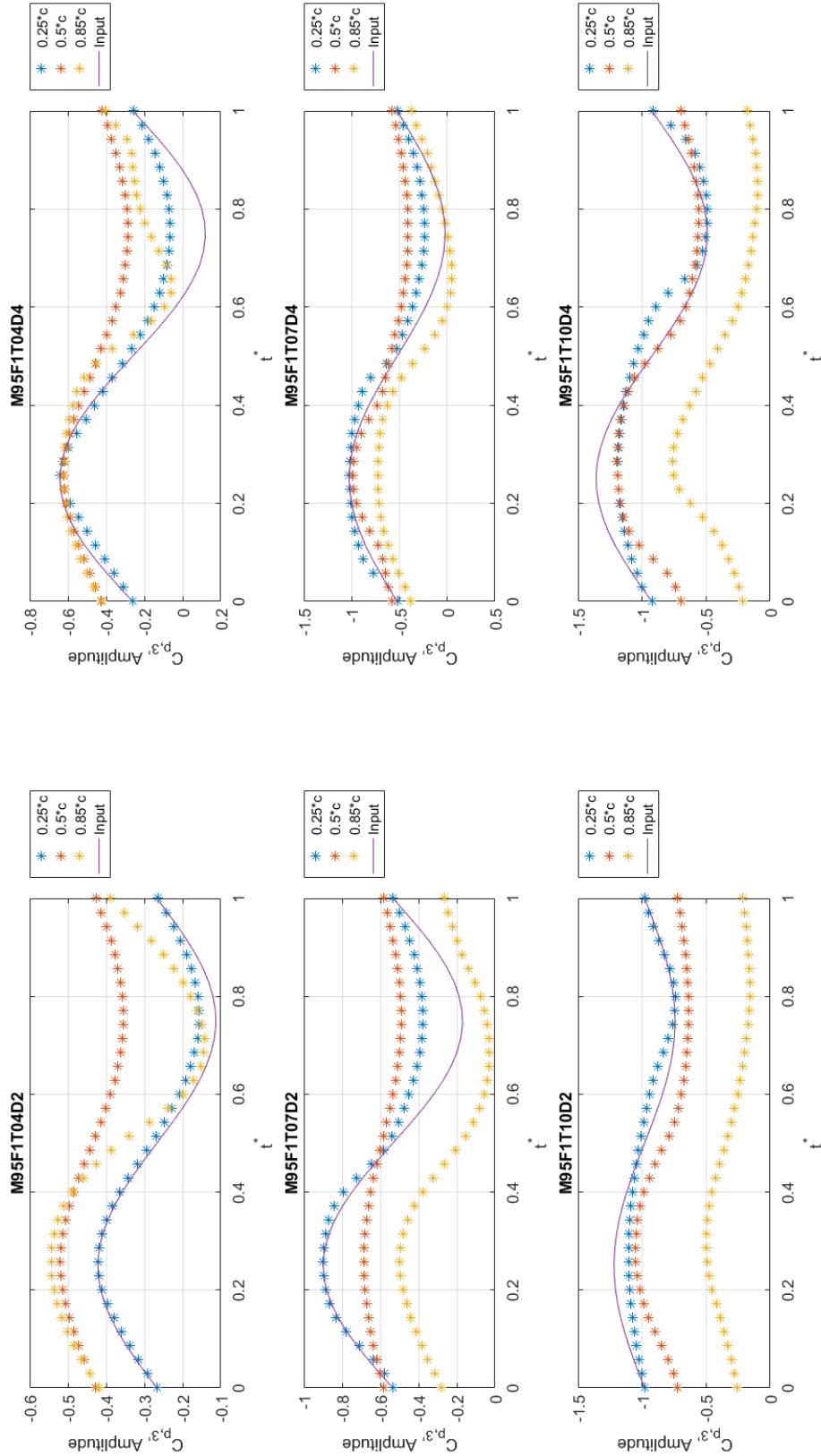


Figure C.4: Time history of C_p for for three points along the chord of station 3. $M = 0.95$, Frequency = 5.7 Hz.

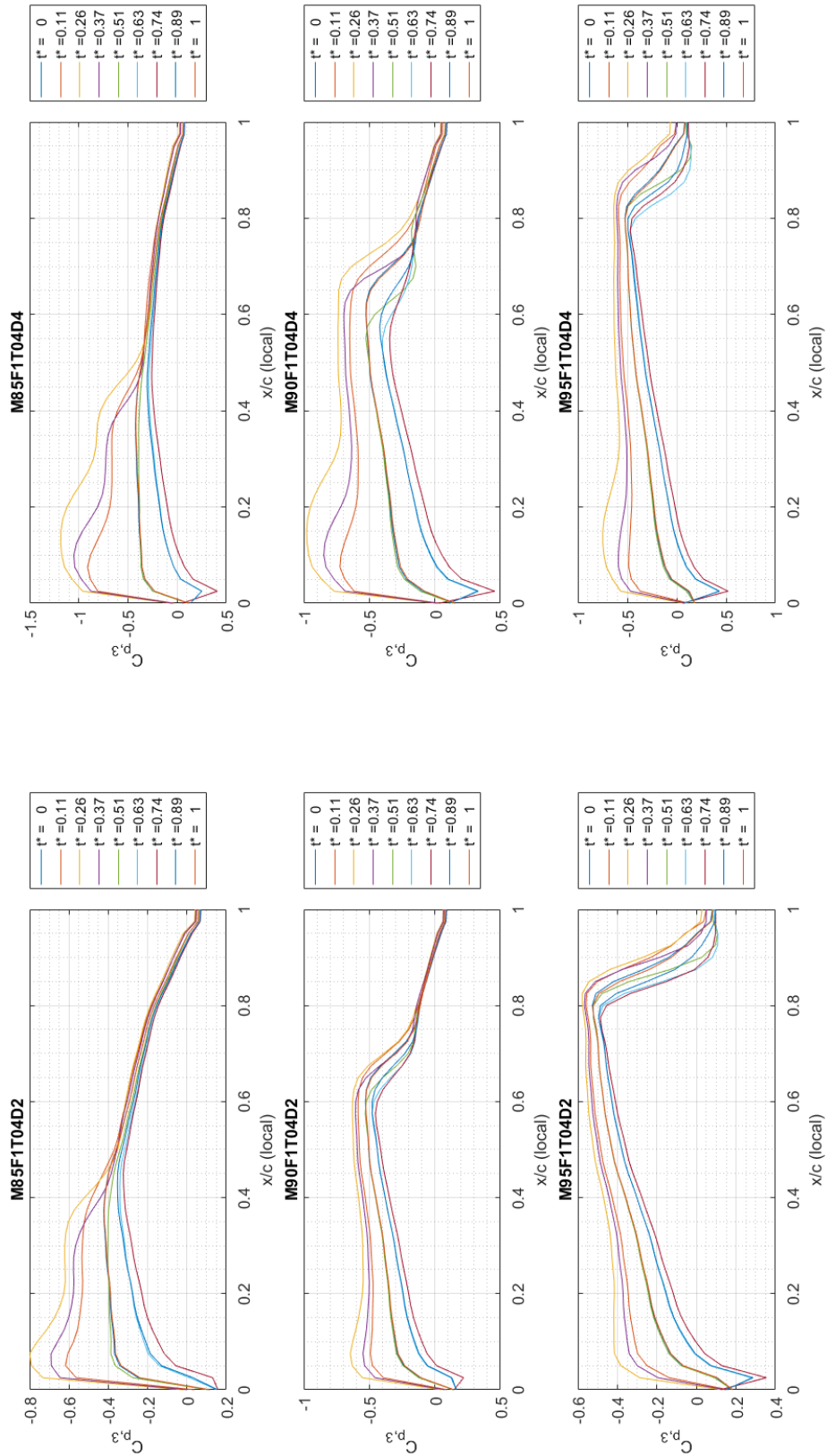


Figure C.5: Mach Comparison. Time history of C_p varying Mach number down the column. Frequency = 5.7 Hz, Trim = 4° .

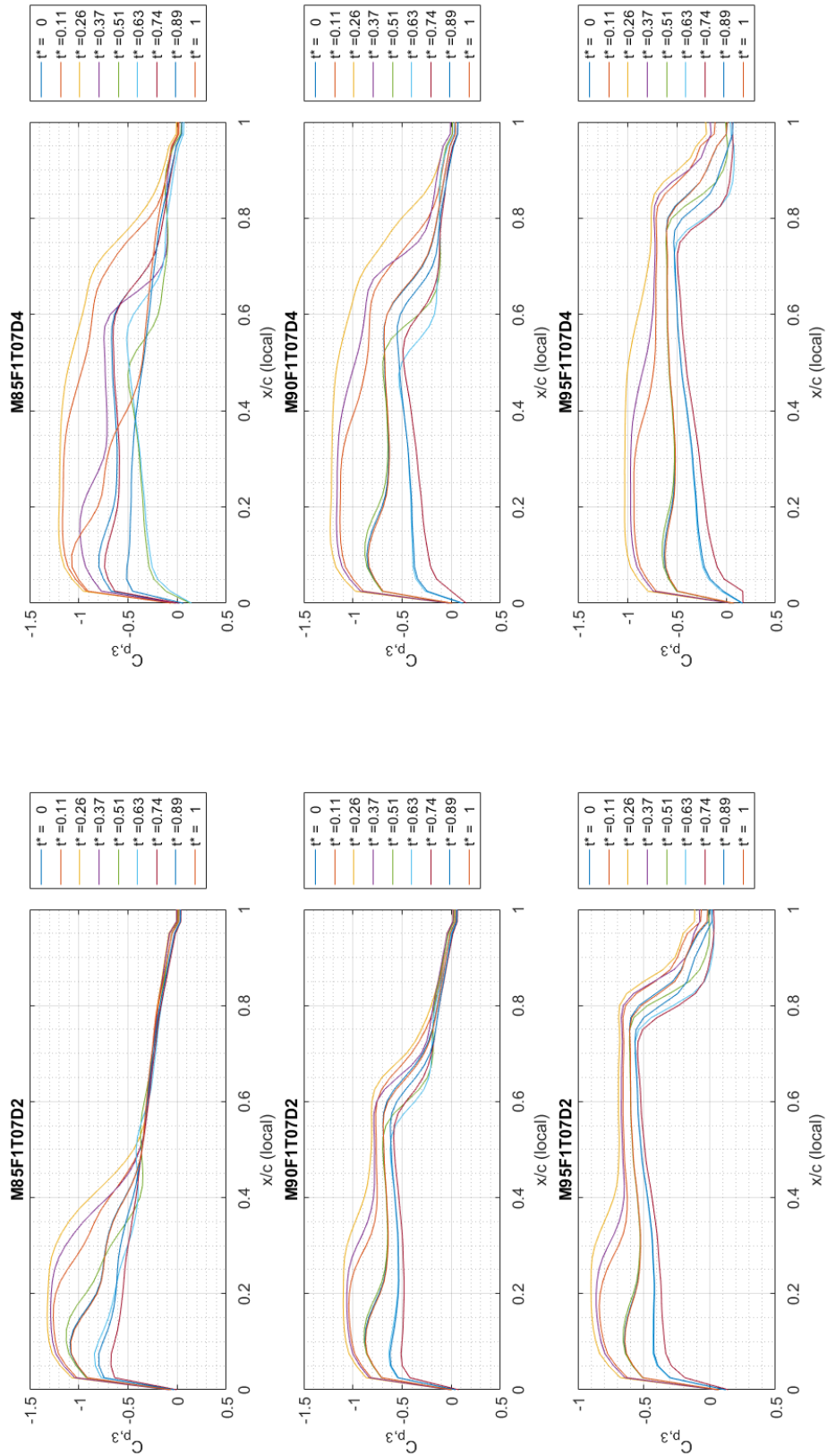


Figure C.6: Mach Comparison. Time history of C_p varying Mach number down the column. Frequency = 5.7 Hz, Trim = 7° .

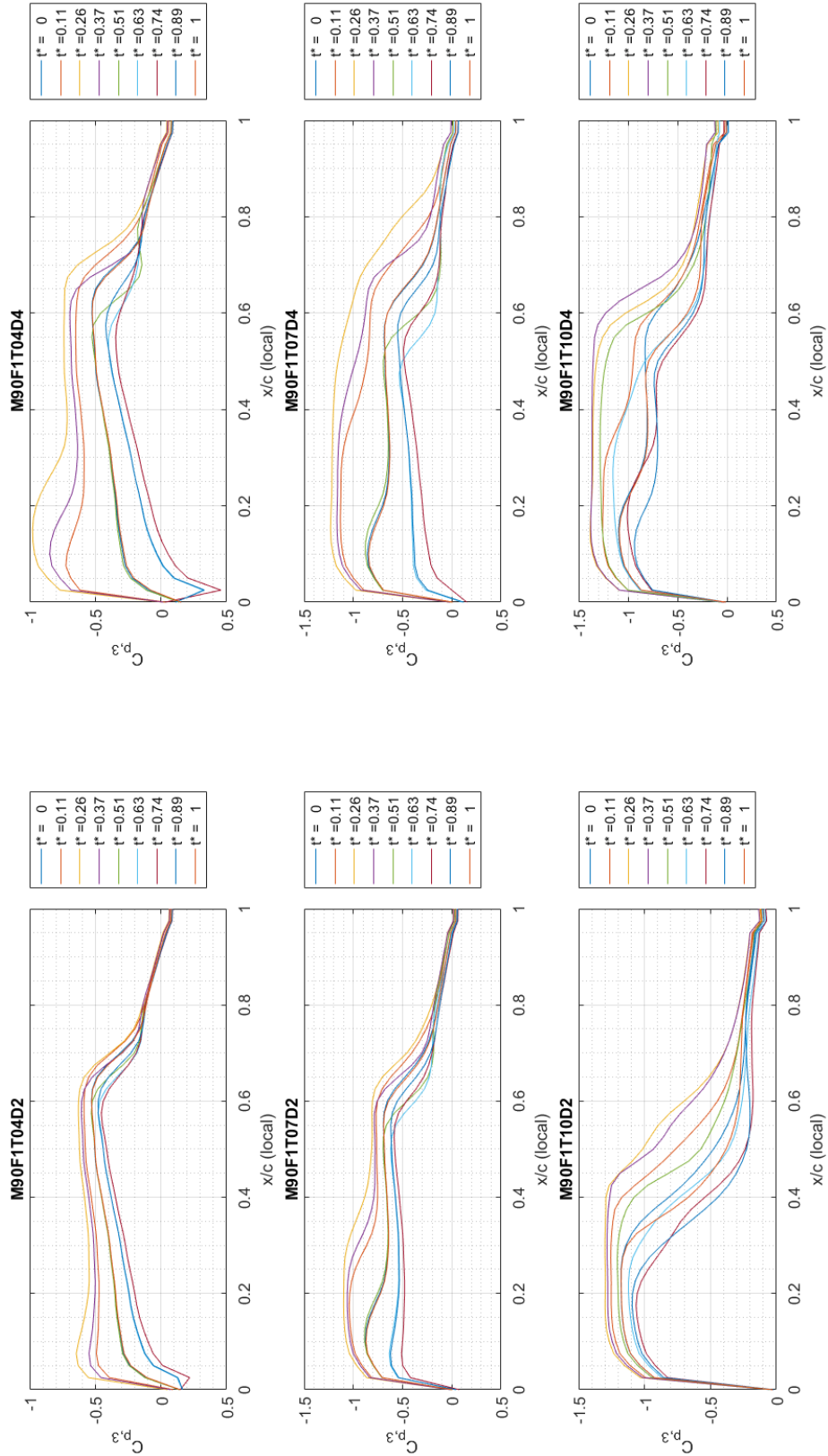


Figure C.7: BLC trim and $\Delta\alpha$ comparison of C_p . $M = 0.9$, Frequency = 5.7 Hz.

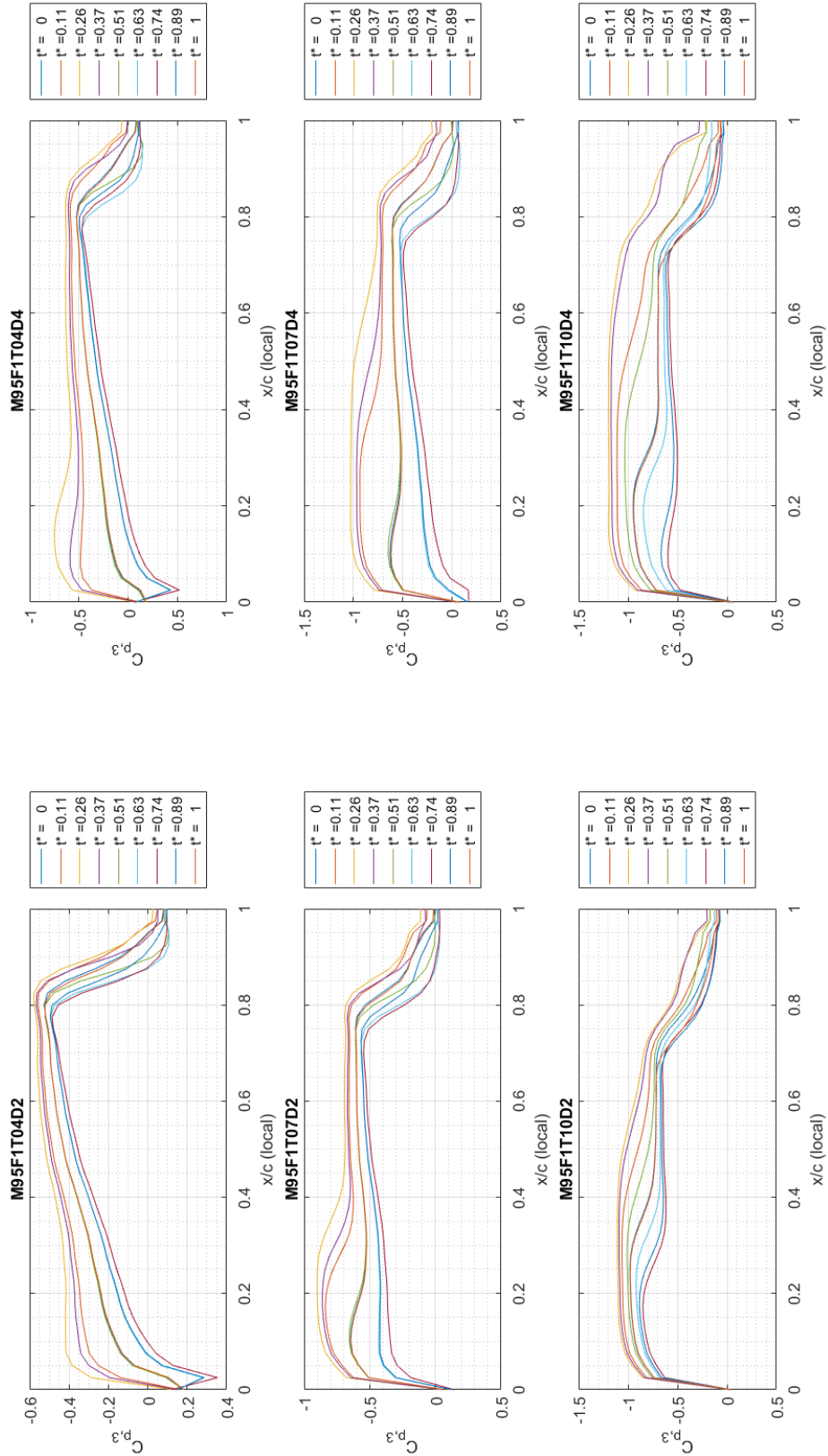


Figure C.8: BLC trim and $\Delta\alpha$ comparison of C_p . $M = 0.95$, Frequency = 5.7 Hz.

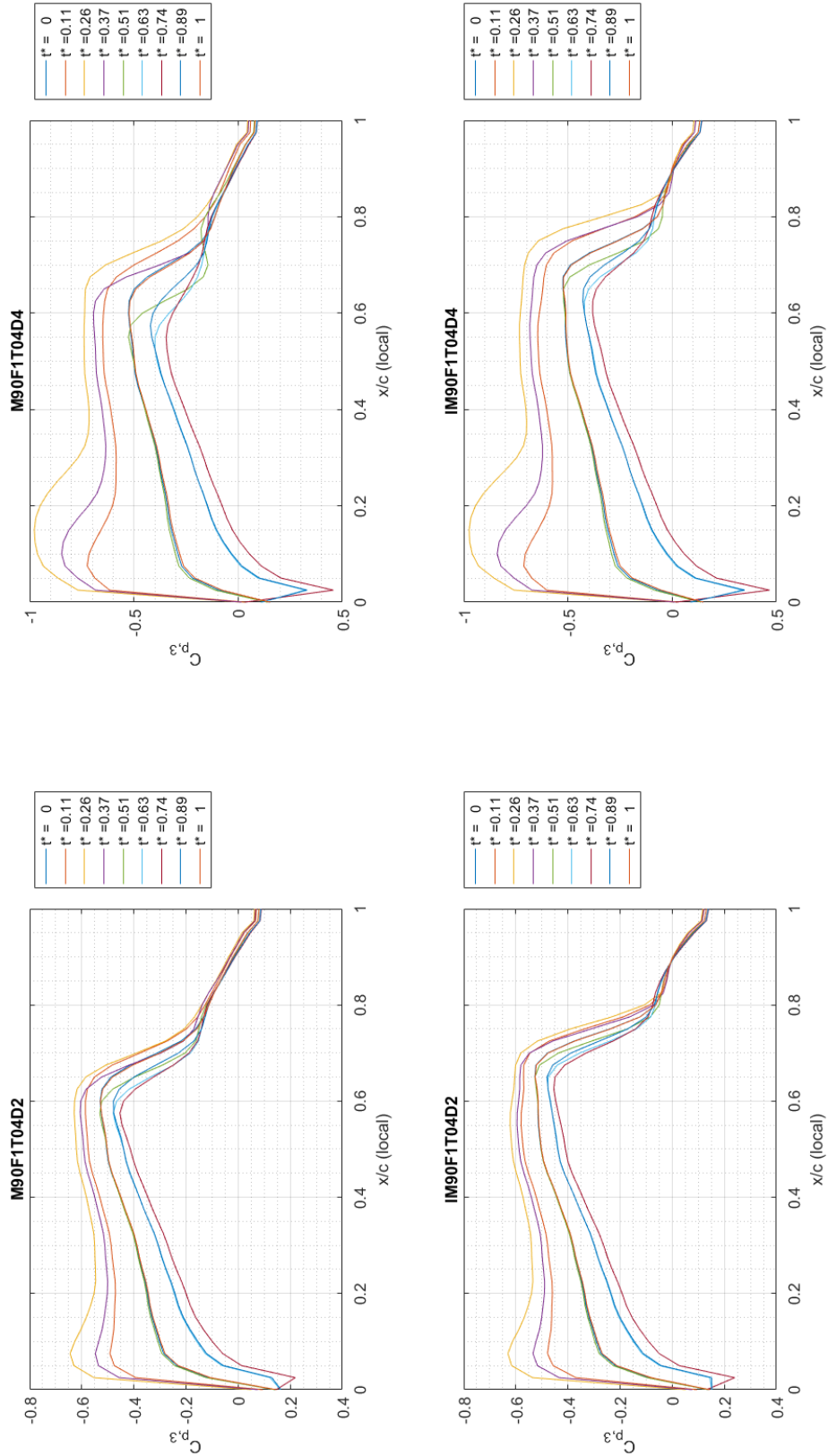


Figure C.9: Inviscid/Viscous comparison of C_p . $M = 0.9$, Frequency = 5.7 Hz, Trim $\alpha = 4^\circ$.

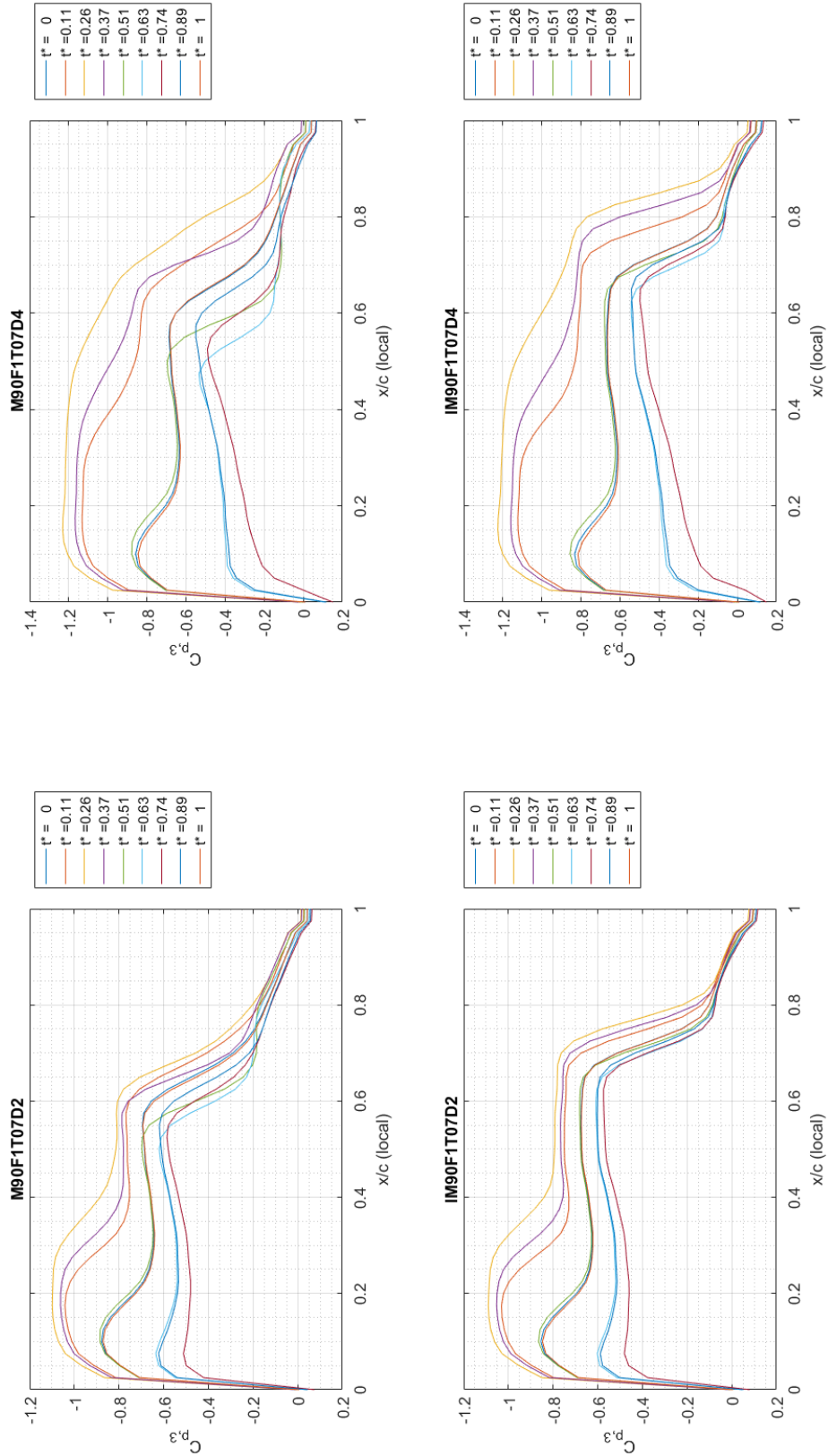


Figure C.10: Inviscid/Viscous comparison of C_p . $M = 0.9$, Frequency = 5.7 Hz, Trim $\alpha = 7^\circ$.

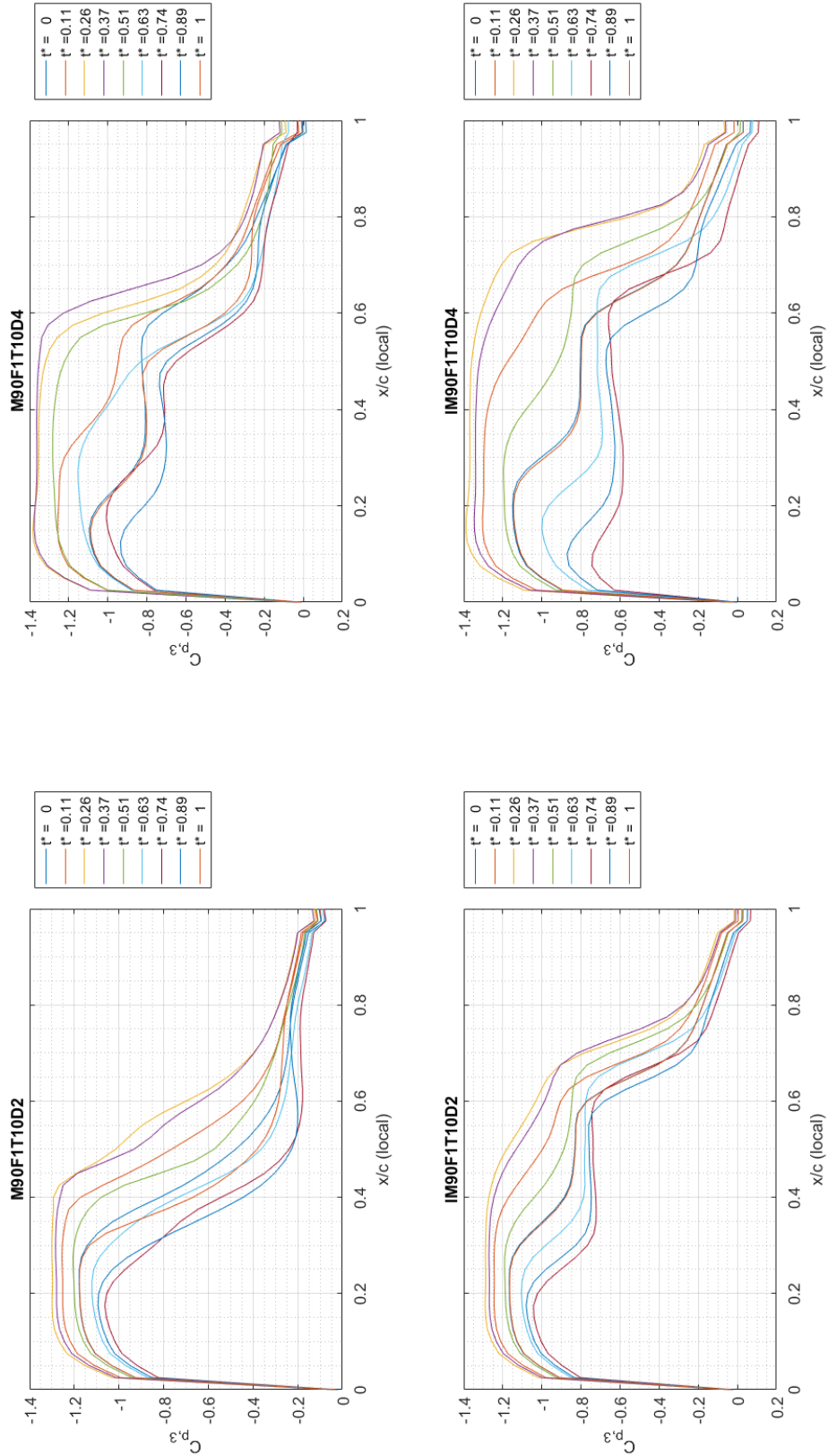


Figure C.11: Inviscid/Viscous comparison of C_p . $M = 0.9$, Frequency = 5.7 Hz, Trim $\alpha = 10^\circ$.

Appendix D. C_p Data for Wing Station 4

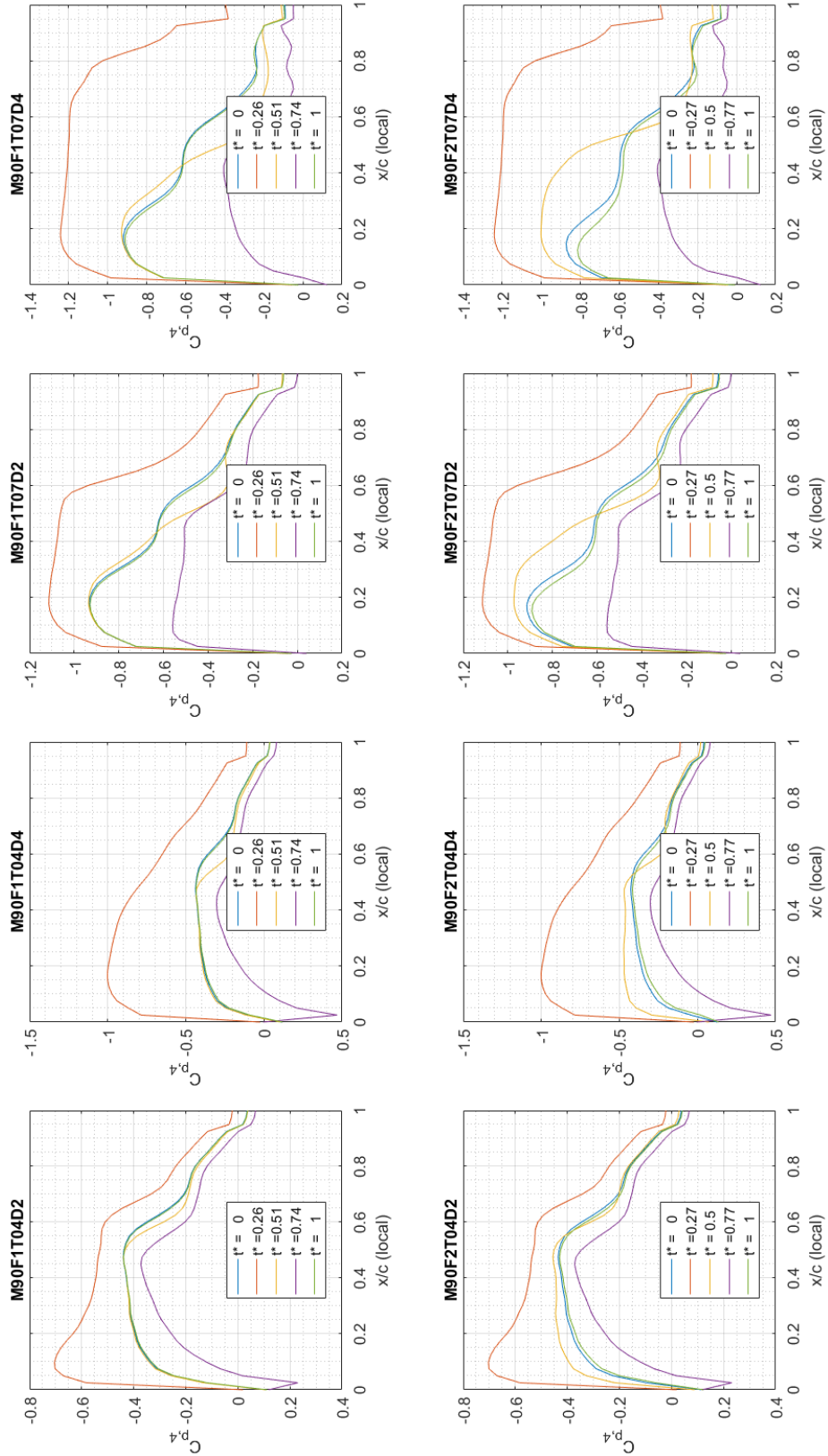


Figure D.1: Frequency Comparison. Time history of C_p for $M = 0.90$, Frequency = 5.7 Hz.

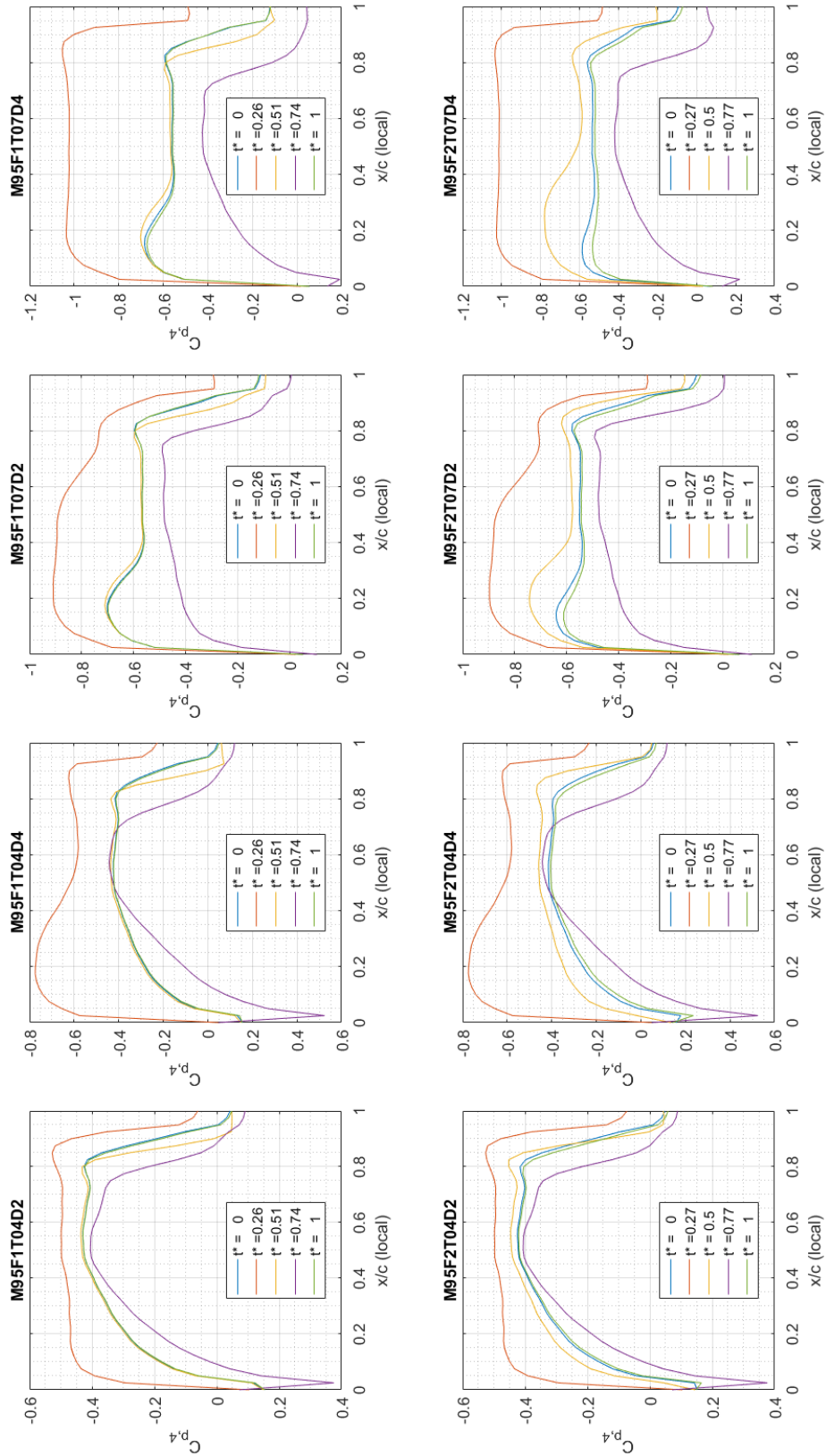


Figure D.2: Frequency Comparison. Time history of C_p for $M = 0.90$, Frequency = 7.4 Hz.

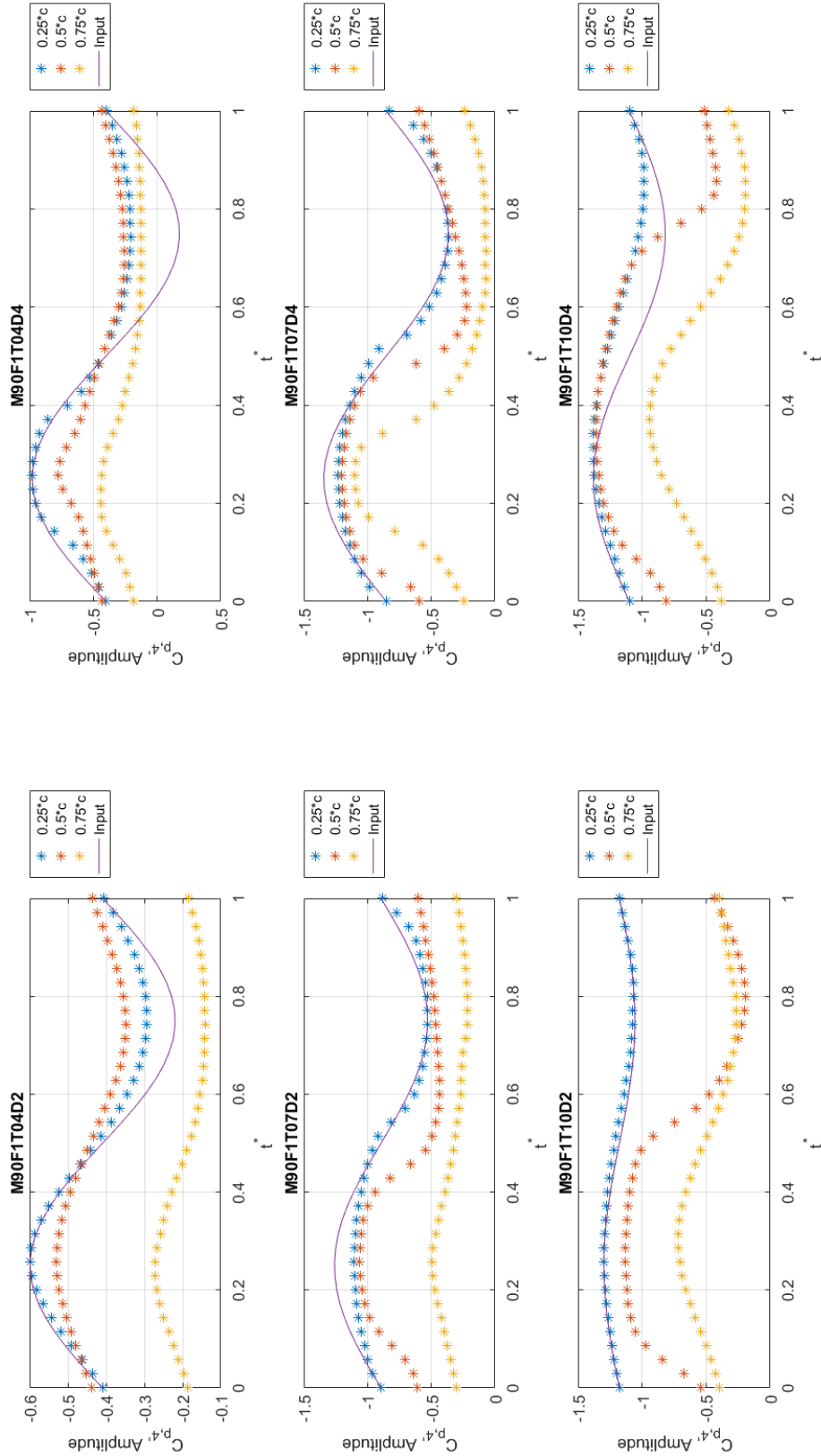


Figure D.3: Time history of C_p for for three points along the chord of station 4. $M = 0.90$, Frequency = 5.7 Hz.

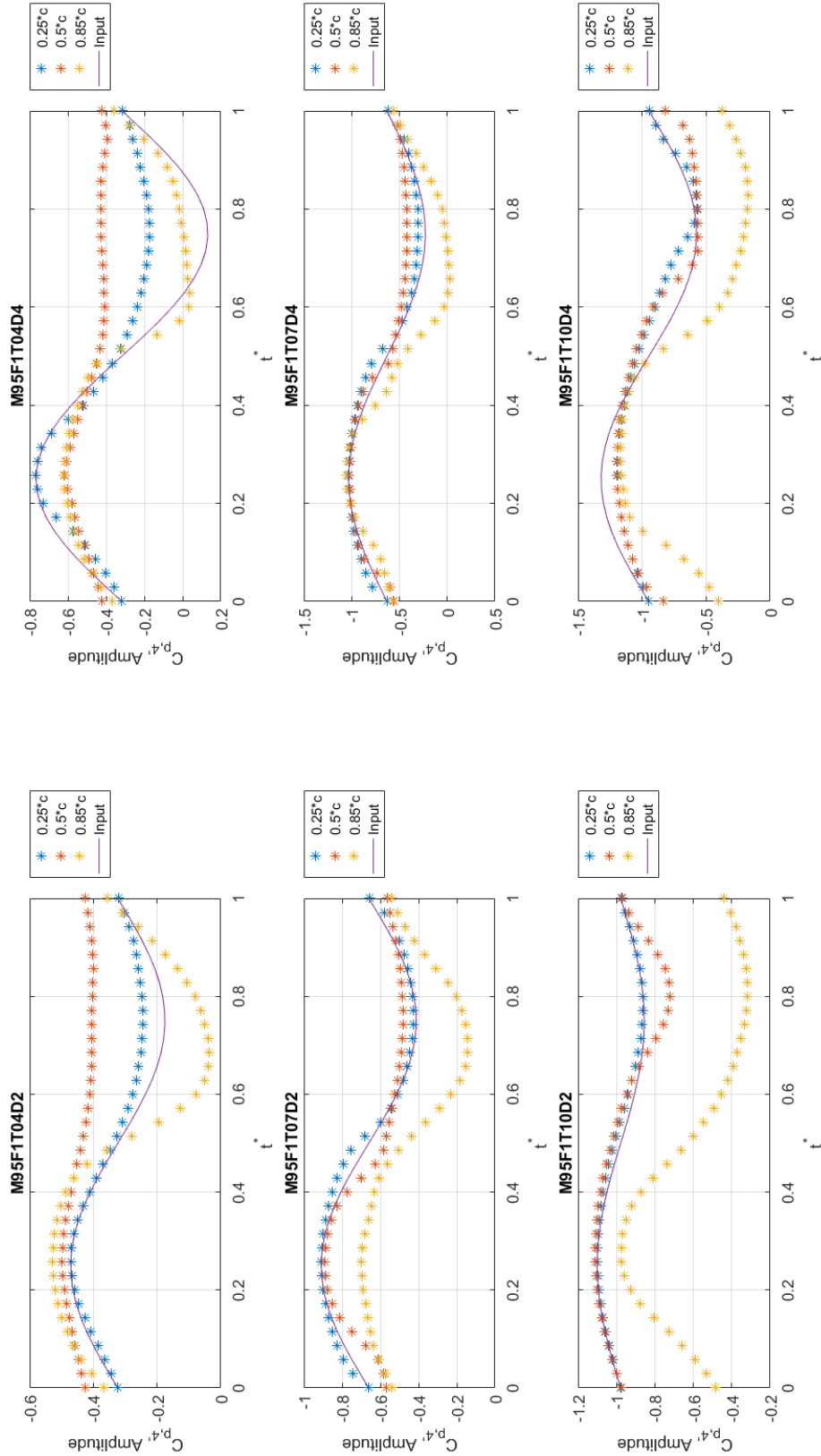


Figure D.4: Time history of C_p for for three points along the chord of station 4. $M = 0.95$, Frequency = 5.7 Hz.

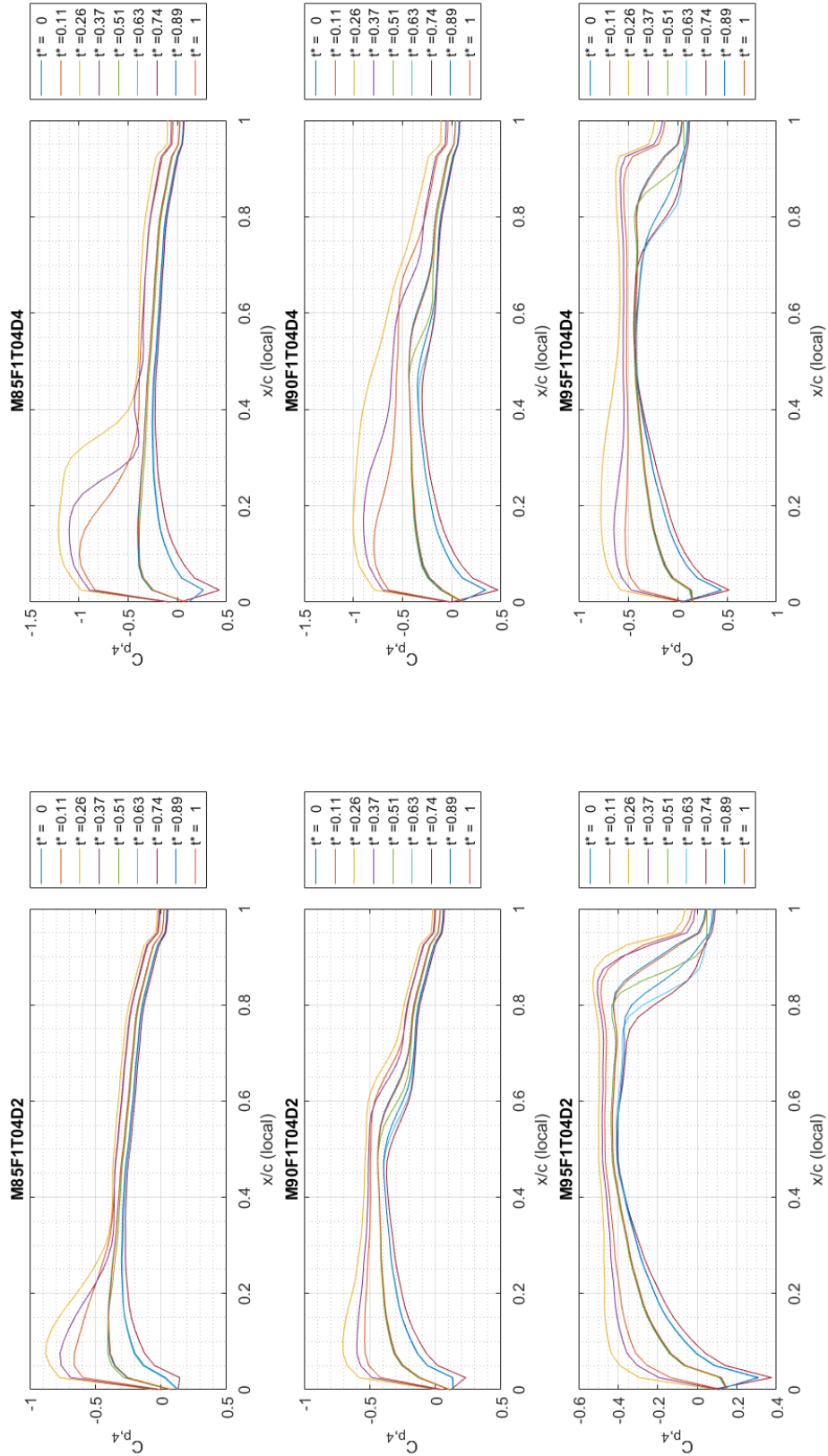


Figure D.5: Mach Comparison. Time history of C_p varying Mach number down the column. Frequency = 5.7 Hz, Trim = 4° .

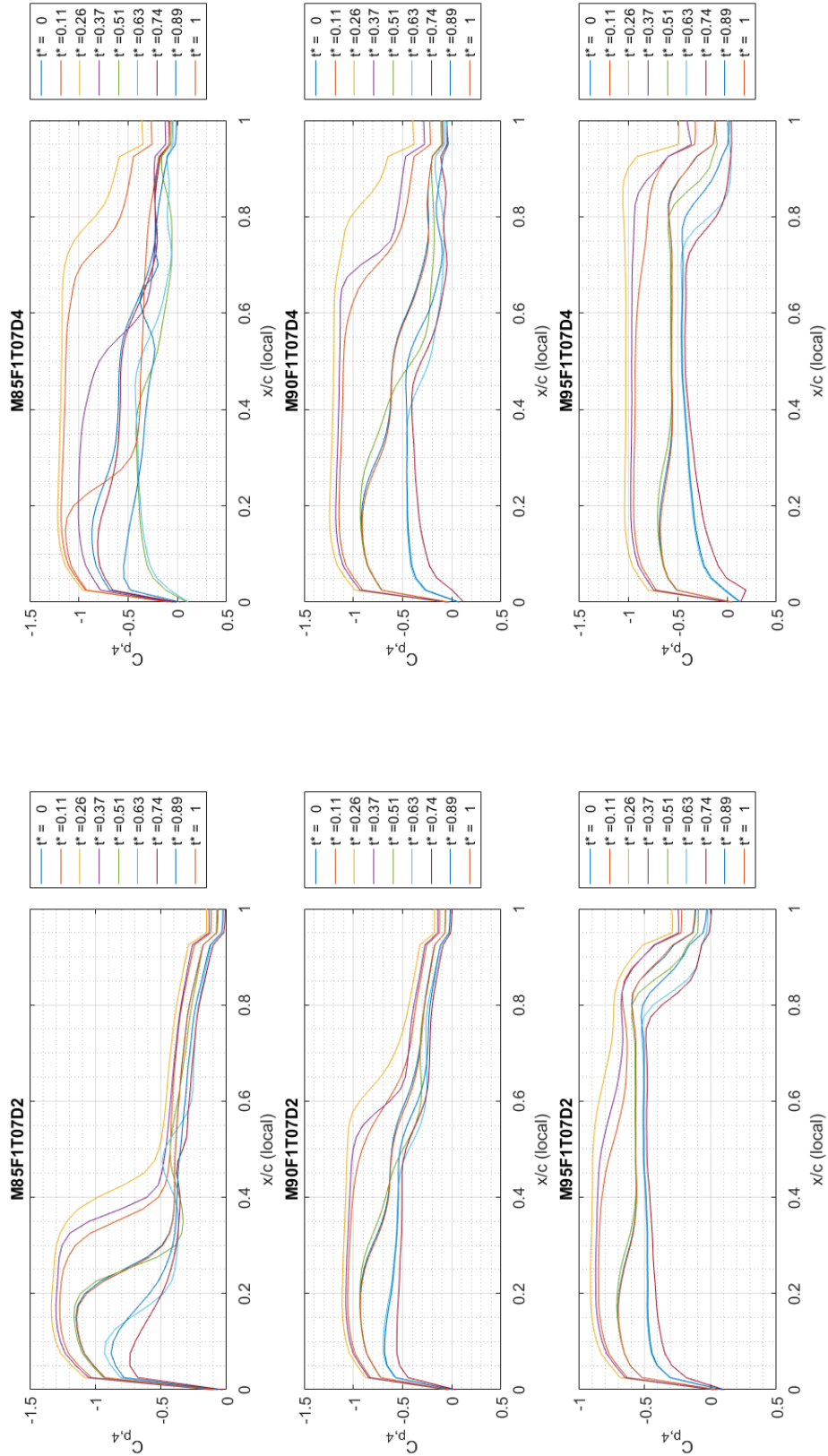


Figure D.6: Mach Comparison. Time history of C_p varying Mach number down the column. Frequency = 5.7 Hz, Trim = 7° .

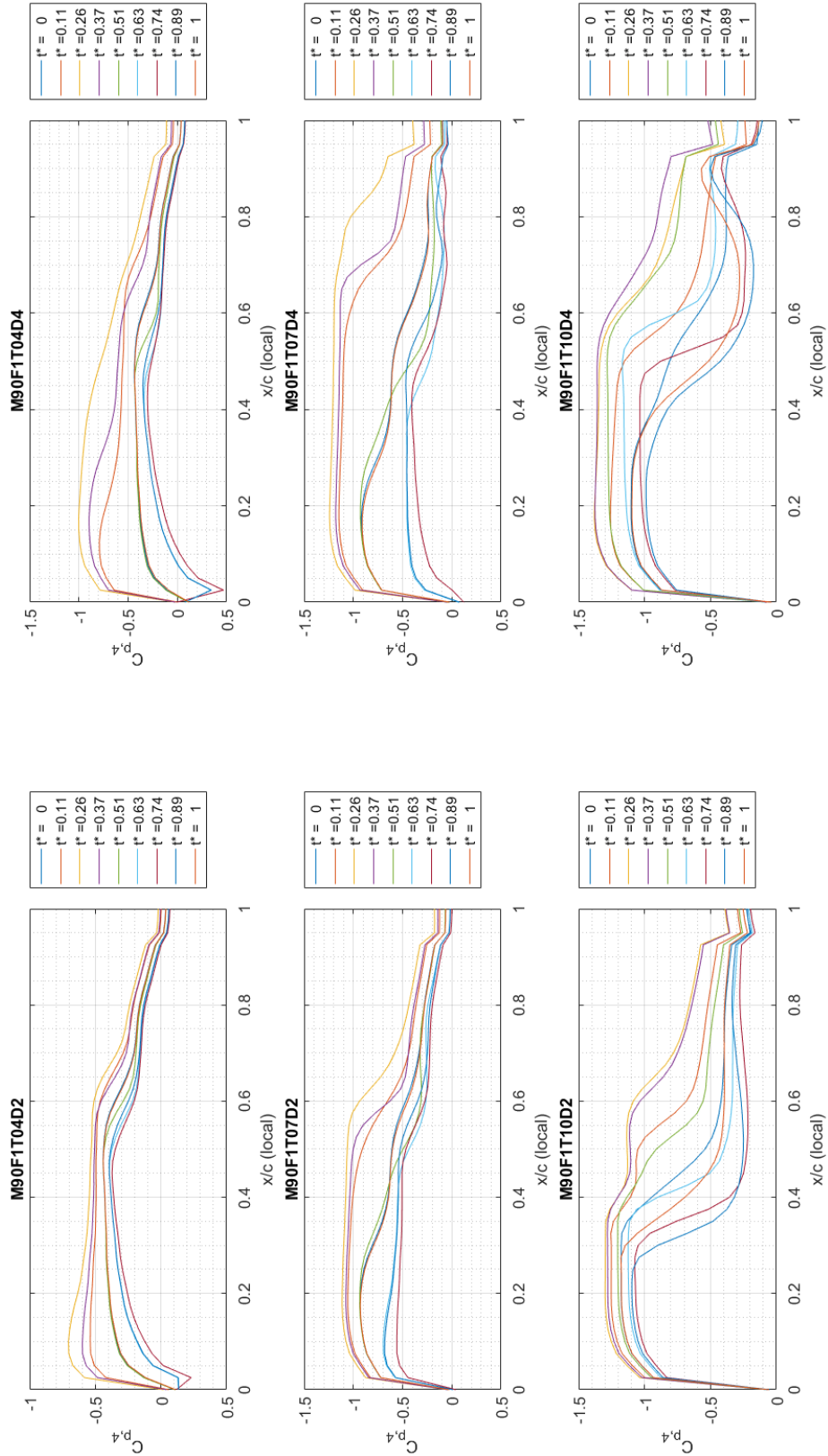


Figure D.7: BLC trim and $\Delta\alpha$ comparison of C_p . $M = 0.9$, Frequency = 5.7 Hz.

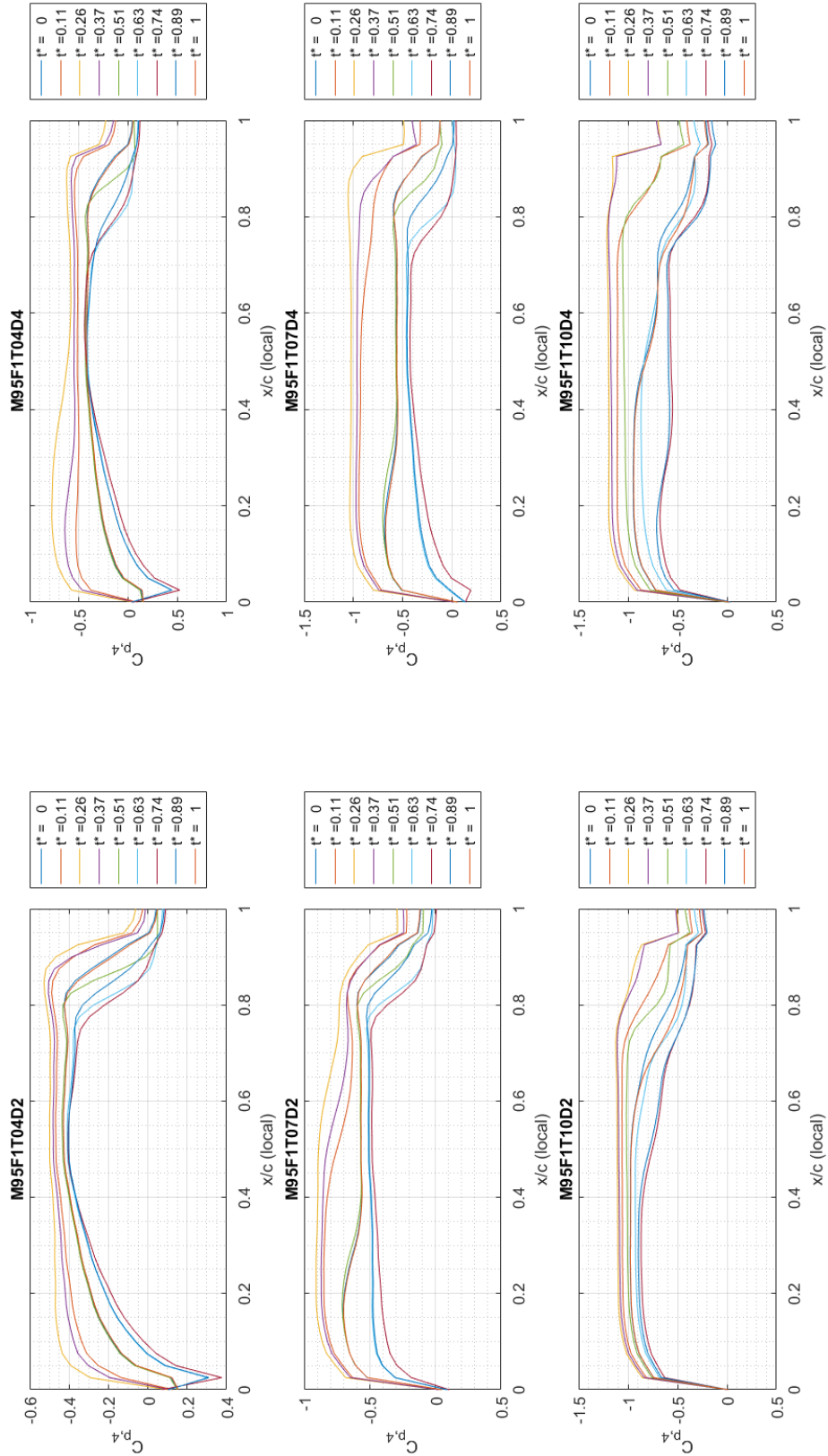


Figure D.8: BLC trim and $\Delta\alpha$ comparison of C_p . $M = 0.95$, Frequency = 5.7 Hz.

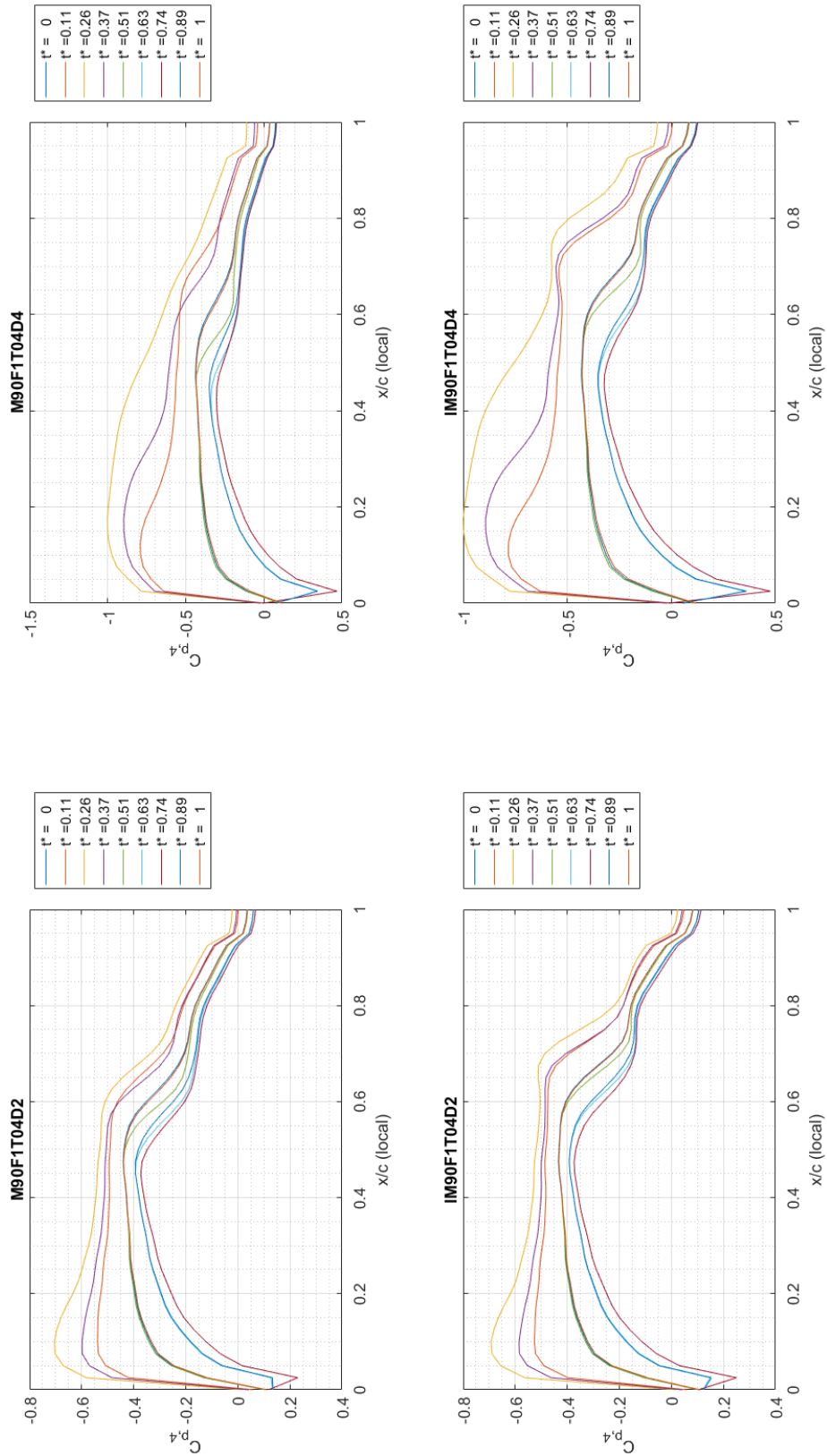


Figure D.9: Inviscid/Viscous comparison of C_p . $M = 0.9$, Frequency = 5.7 Hz, Trim $\alpha = 4^\circ$.

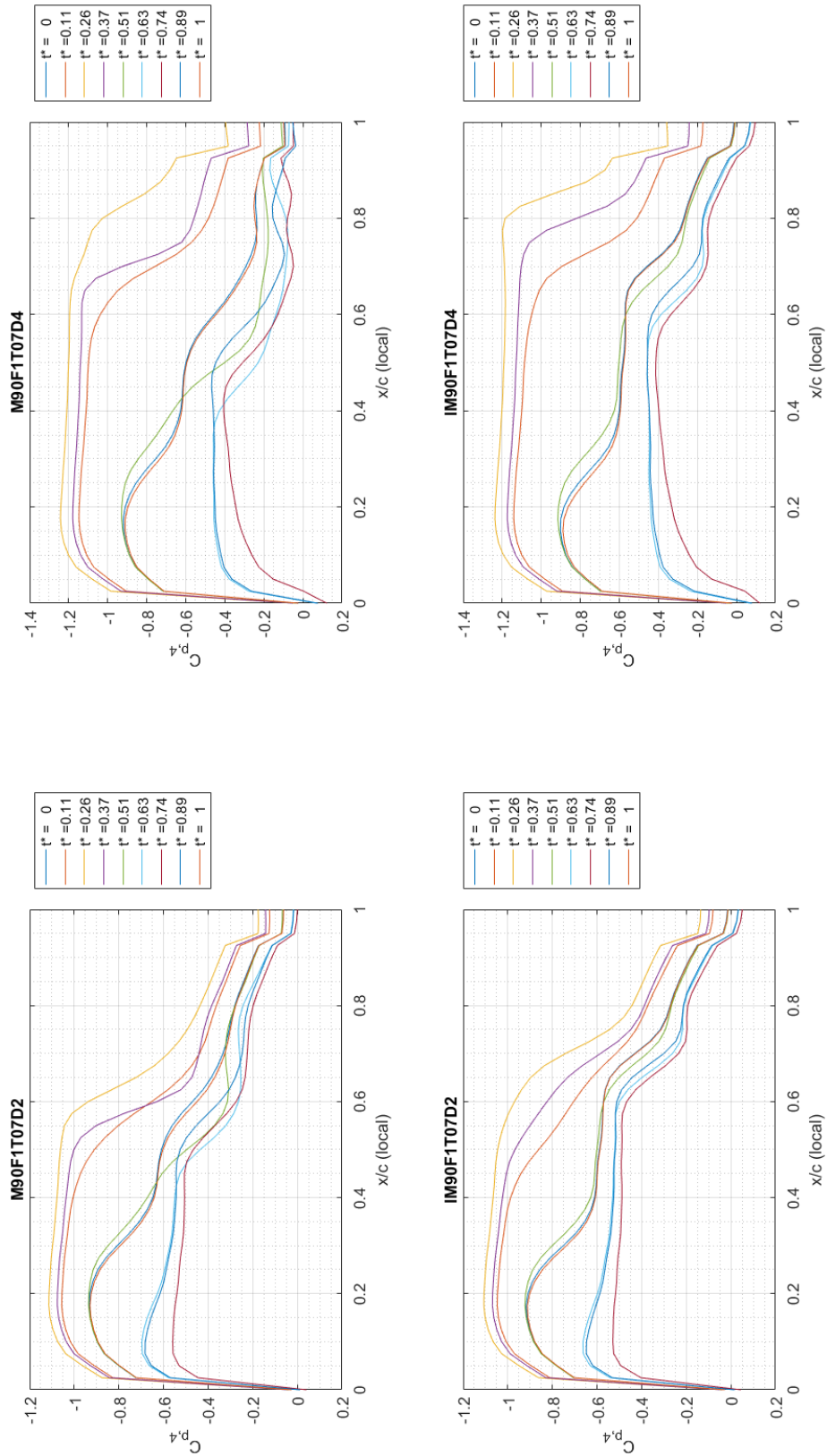


Figure D.10: Inviscid/Viscous comparison of C_p . $M = 0.9$, Frequency = 5.7 Hz, Trim $\alpha = 7^\circ$.

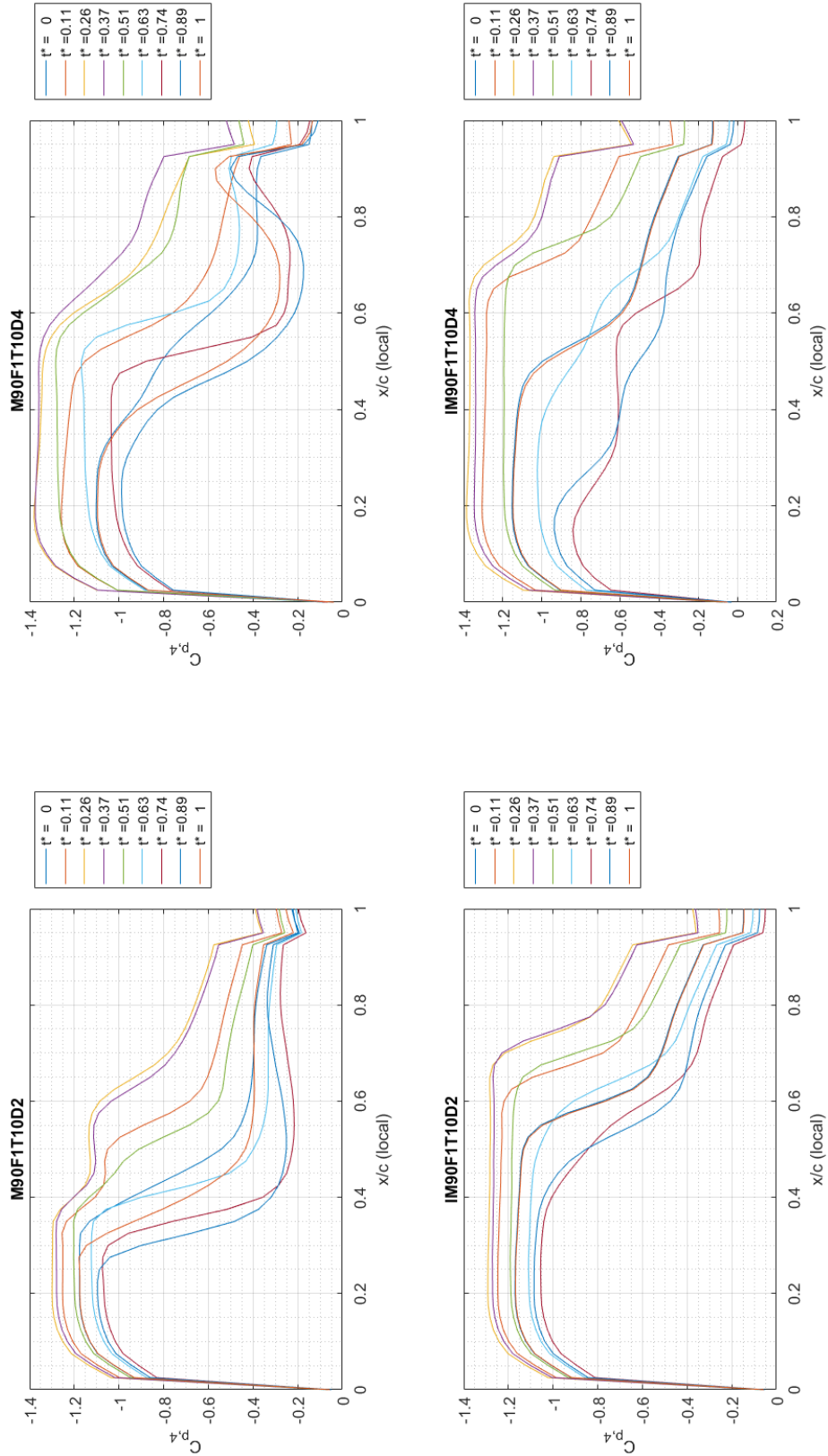


Figure D.11: Inviscid/Viscous comparison of C_p . $M = 0.9$, Frequency = 5.7 Hz, Trim = 10° .

Appendix E. Temporal Comparison of each wing station

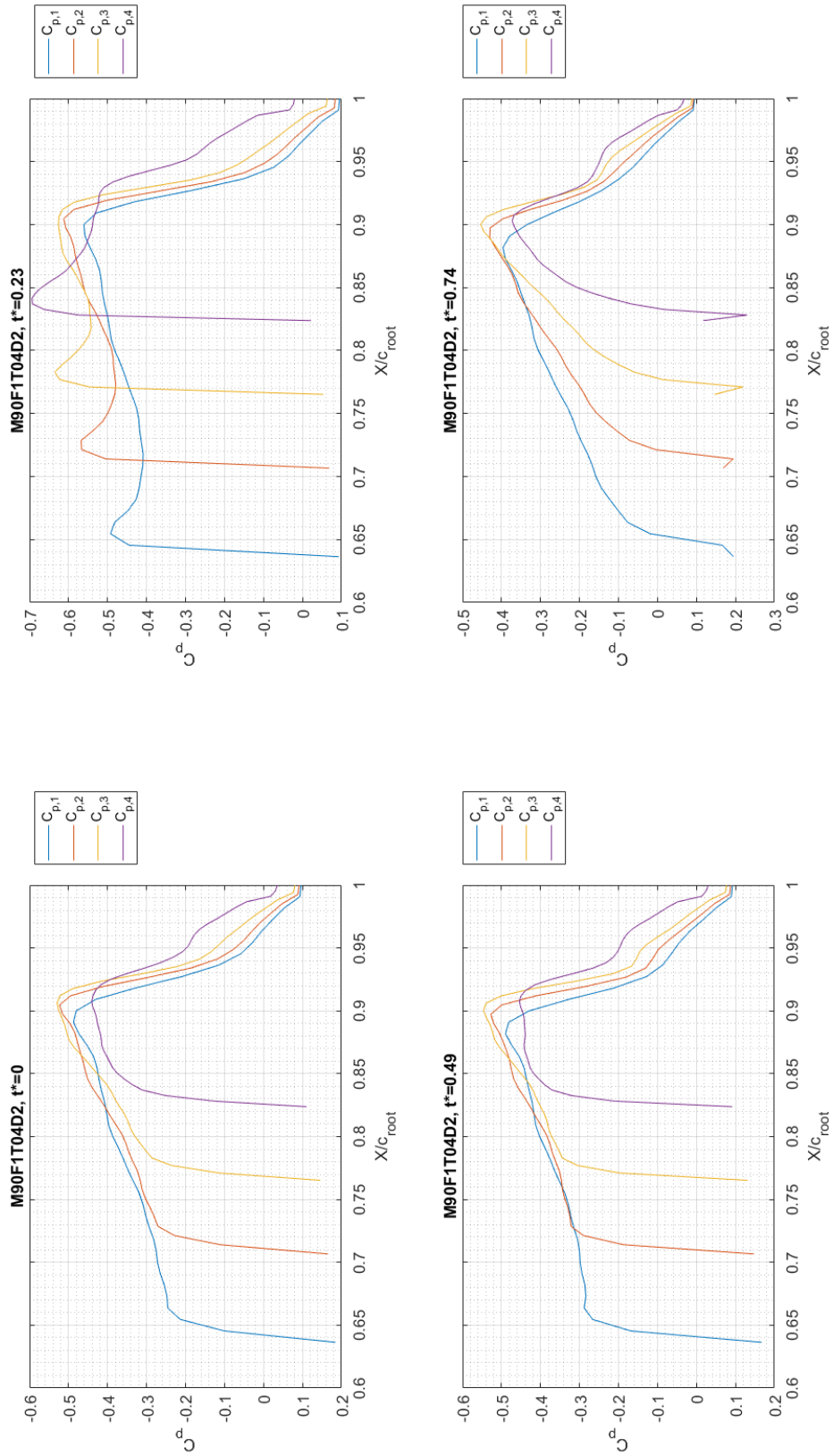


Figure E.1: C_p on the wing's surface for all 4 chordwise stations. Each plot indicates a temporal snapshot for the test case: $M = 0.90$, Frequency = 5.7 Hz, Trim = 4° , $\Delta\alpha = \pm 2^\circ$. 126

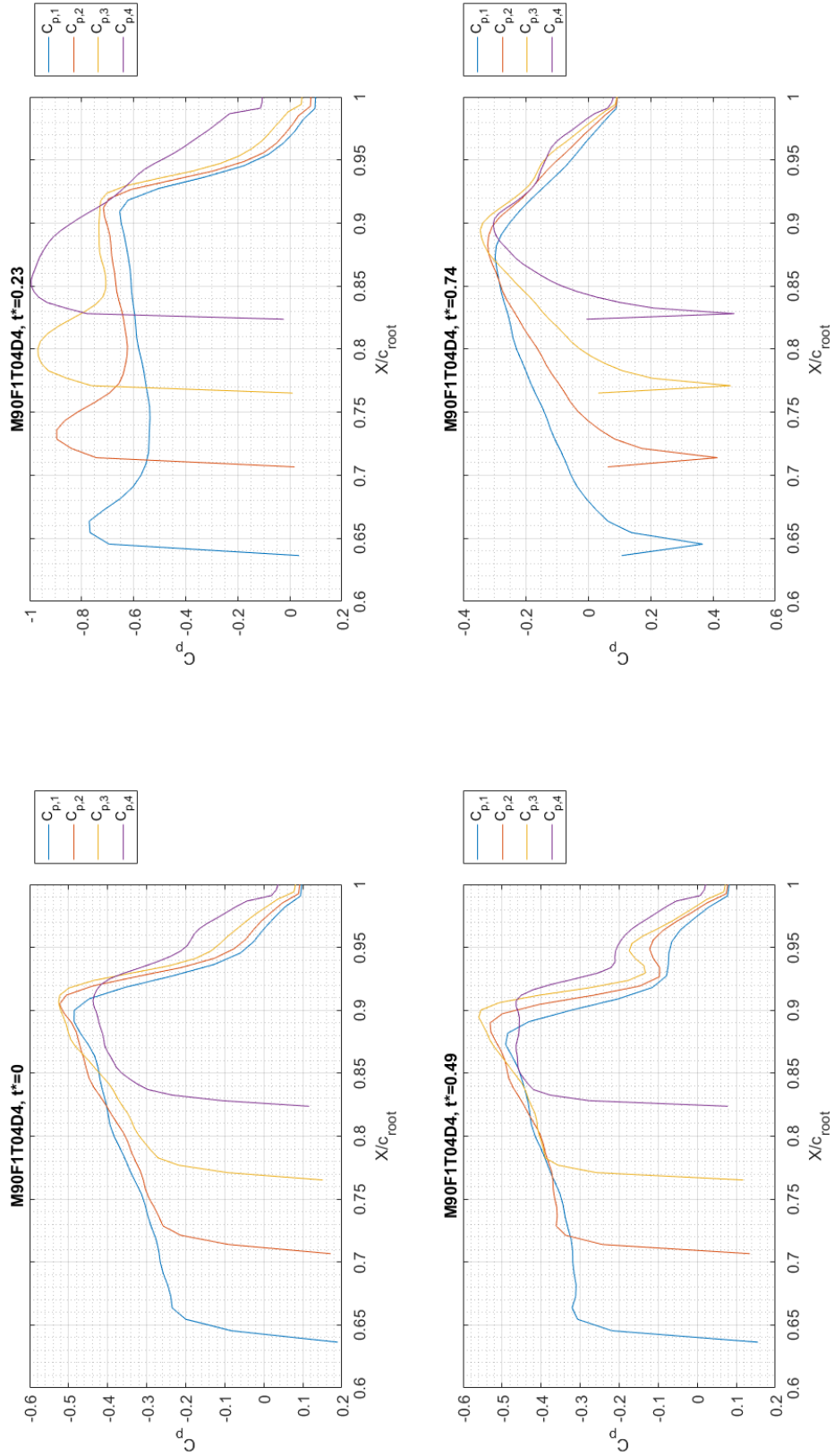


Figure E.2: C_p on the wing's surface for all 4 chordwise stations. Each plot indicates a temporal snapshot for the test case: $M = 0.90$, Frequency = 5.7 Hz, Trim = 4° , $\Delta\alpha = \pm 4^\circ$. 127

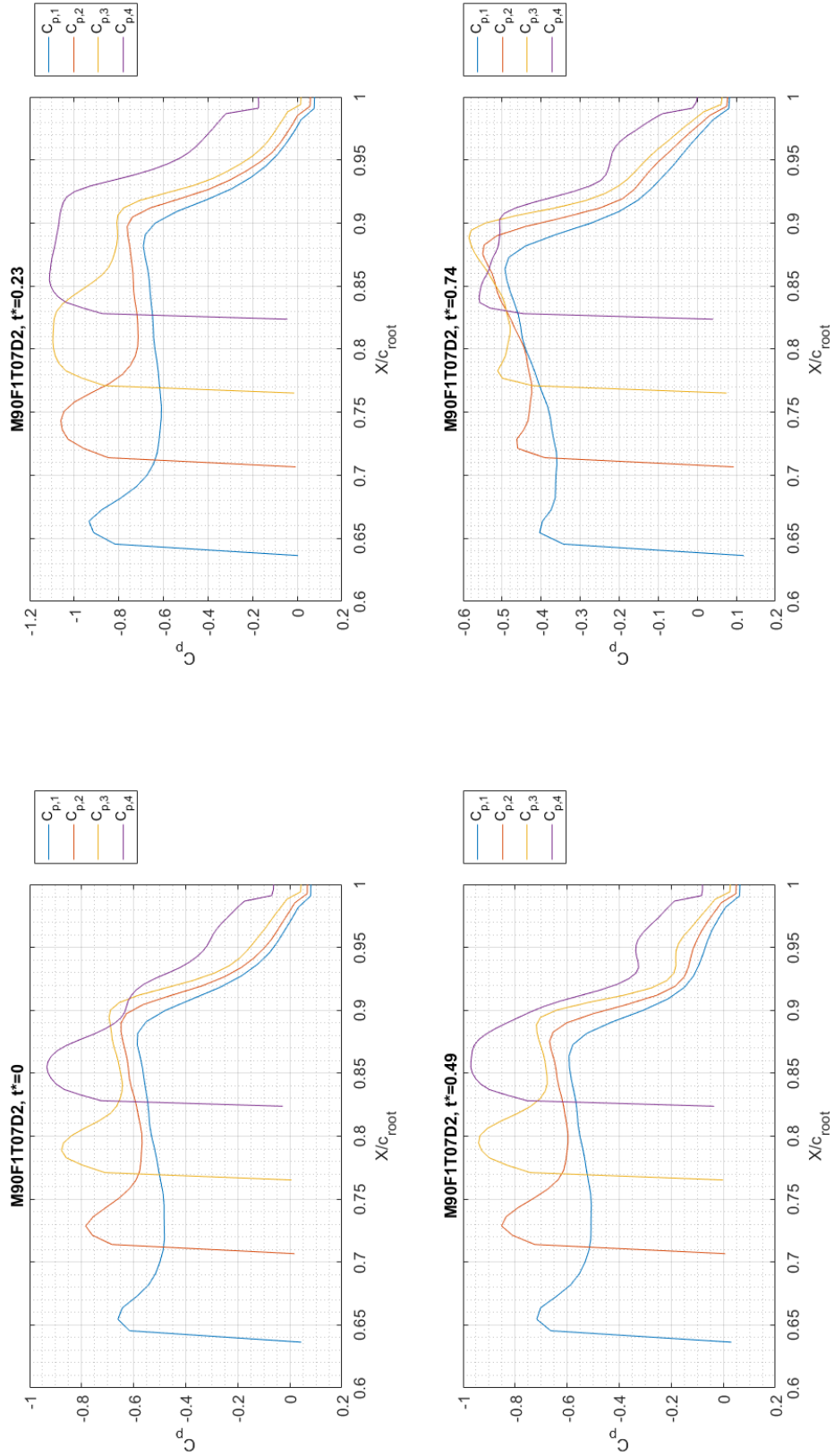


Figure E.3: C_p on the wing's surface for all 4 chordwise stations. Each plot indicates a temporal snapshot for the test case: $M = 0.90$, Frequency = 5.7 Hz, Trim = 7° , $\Delta\alpha = \pm 2^\circ$. 128

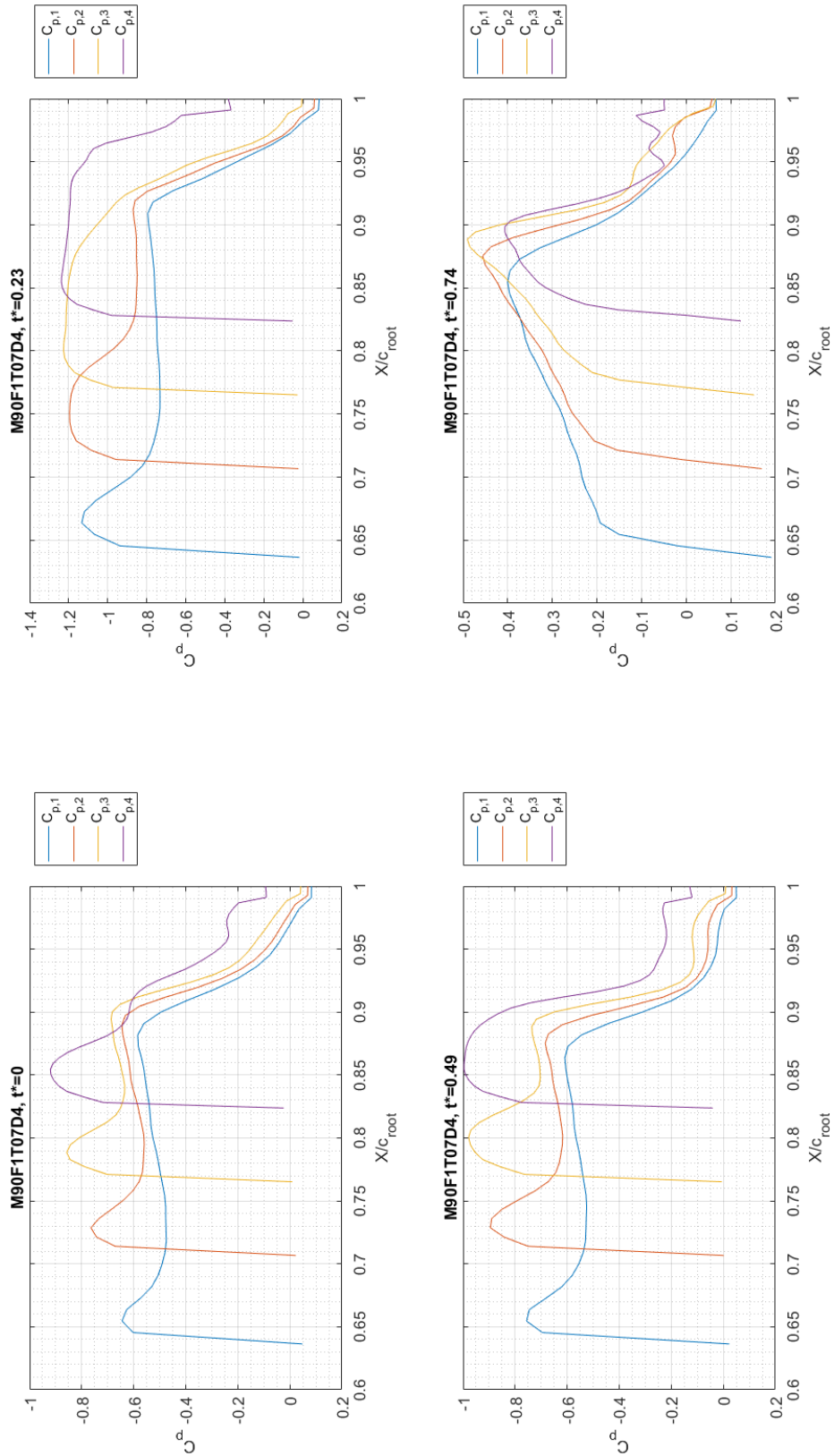


Figure E.4: C_p on the wing's surface for all 4 chordwise stations. Each plot indicates a temporal snapshot for the test case: $M = 0.90$, Frequency = 5.7 Hz, Trim = 7° , $\Delta\alpha = \pm 4^\circ$. 129

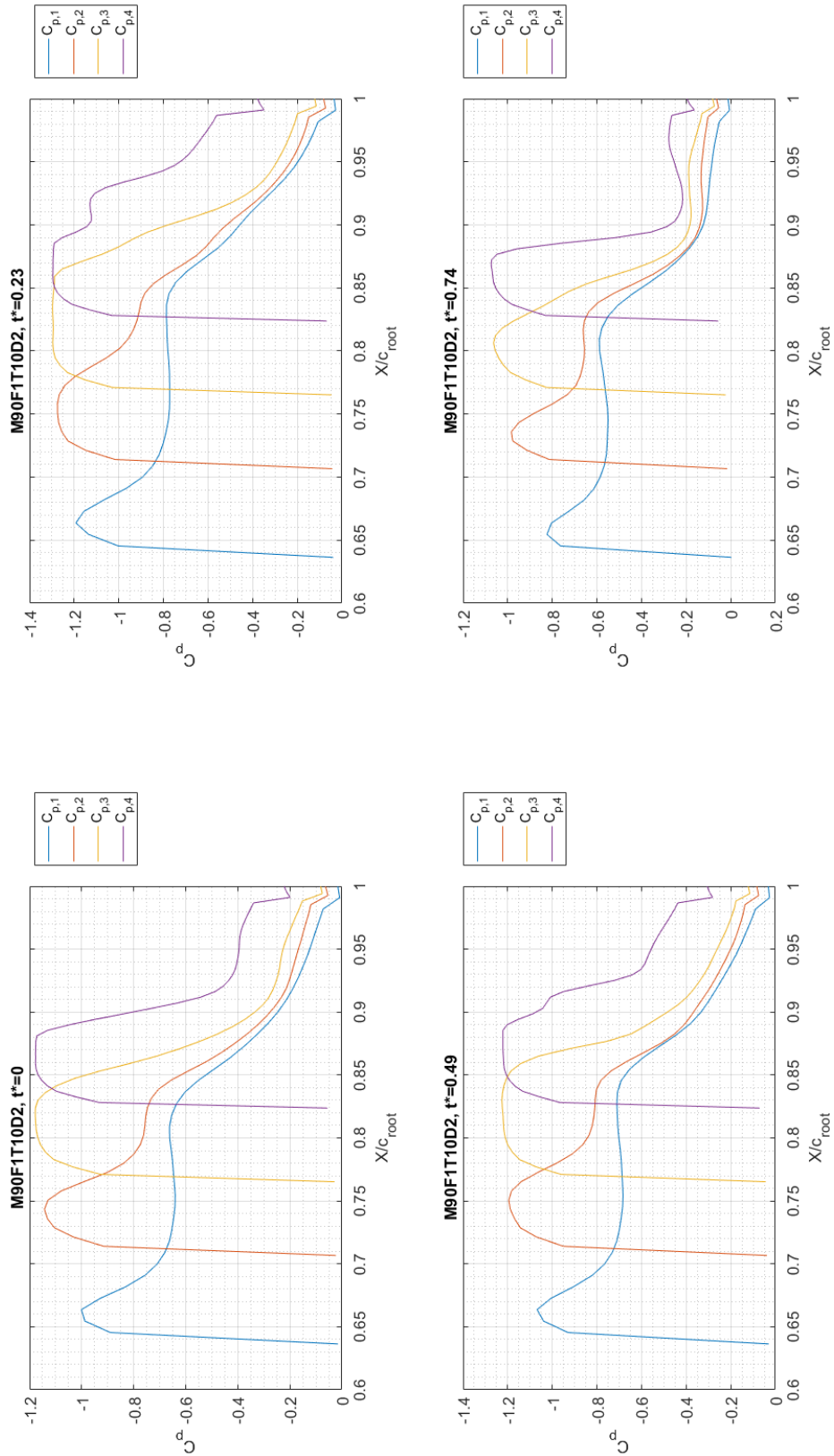


Figure E.5: C_p on the wing's surface for all 4 chordwise stations. Each plot indicates a temporal snap shot for the test case: $M = 0.90$, Frequency = 5.7 Hz, Trim = 10° , $\Delta\alpha = \pm 2^\circ$. 130

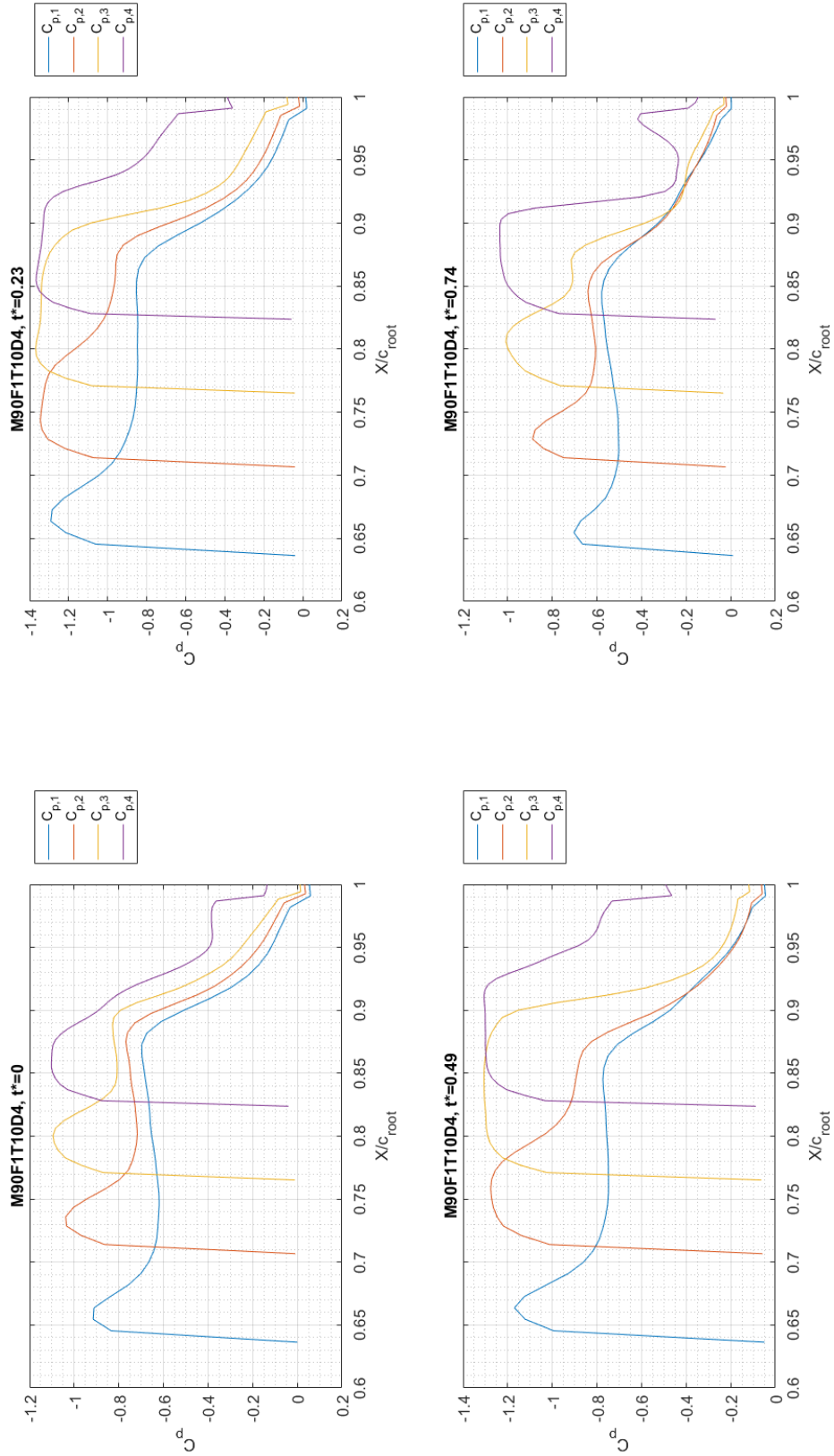


Figure E.6: C_p on the wing's surface for all 4 chordwise stations. Each plot indicates a temporal snap shot for the test case: $M = 0.90$, Frequency = 5.7 Hz, Trim = 10° , $\Delta\alpha = \pm 4^\circ$. 131

Bibliography

1. den Boer, R.G. and A.M. Jr. Cunningham. "Low Speed Unsteady Aerodynamics of a Pitching Straked Wing at High Incidence". *Journal of Aircraft*, 27:22–30, 1990.
2. Bunton, Robert W. and Charles M. Denegri, Jr. "Limit Cycle Oscillation Characteristics of Fighter Aircraft". *Journal of Aircraft*, 37(5):916–918, Sep 2000.
3. Carter, J.E. "A New Boundary-Layer Inviscid Iteration Technique for Separated Flow". 1979-1450. 4th Computational Fluid Dynamics Conference, Williamsburg, VA, July 1979.
4. Chen, P.C. "Damping Perturbation Method for Flutter Solution: The g-Method". *AIAA Journal*, 38(9):1519–1524, September 2000.
5. Chen, P.C., D. Sarhaddi, and D.D. Liu. "Limit Cycle Oscillation Studies of a Fighter with External Stores". 98-1727. 39TH AIAA/ASME/ASCE/AHS/ASC STRUCTURES, STRUCTURAL DYNAMICS, AND MATERIALS CONFERENCE AND EXHIBIT, Long Beach, CA, April 1998.
6. Cunningham, A. M. *The Role of Shock Induced Trailing-Edge Separation In Limit Cycle Oscillations*. Technical report, General Dynamics, 1989.
7. Cunningham, A. M. and den Boer R.G. *Overview of Unsteady Transonic Wing Tunnel Test on a Semispan Straked Delta Wing Oscillating in Pitch*. Technical report, Lockheed Fort Worth Company and Nation Aerospace Laboratory, 1994.
8. Cunningham, A. M. and den Boer R.G. *Overview of Unsteady Transonic Wing Tunnel Test on a Semispan Straked Delta Wing Oscillating in Pitch, Part 1*. Technical report, Lockheed Fort Worth Company and Nation Aerospace Laboratory, 1994.
9. Cunningham, A.M. Jr. and R.G. den Boer. *Unsteady Low Speed Wind Tunnel Test of a Straked Delta Wing, Oscillating in Pitch*. Technical Report AFWAL-TR-87-3098.
10. Denegri, Charles M., Jr. "Limit Cycle Oscillation Flight Test Results of a Fighter with External Stores". *Journal of Aircraft*, 37(5):761–769, September 2000.
11. Denegri, Charles M., Jr., James A. Dubben, and Daniel L. Maxwell. "In-Flight Wing Deformation Characteristics During Limit-Cycle Oscillations". *Journal of Aircraft*, 42(2):500–508, March 2005.
12. Denegri, Charles M., Jr. and Michael R. Johnson. "Limit Cycle Oscillation Prediction Using Artificial Neural Networks". *Journal of Guidance, Control, and Dynamics*, 24(5):887–895, September 2001.

13. Dubben, James A. and Jr. Charles M. Denegri. “Underwing Missile Aerodynamic Effects on Flight-Measured Limit Cycle Oscillations”. 48th AIAA/ASME/ASCE/AHS/ASC Structures, Structural Dynamics and Materials Conference, Honolulu HI, April 2007.
14. Edwards, J.W. “Transonic Shock Oscillations Calculated with a New Interactive Boundary Layer Coupling Method”. 93-0777. 31st Aerospace Sciences Meeting, Reno, NV, Jan 1993.
15. E.H. Dowell, K.C. Hall, J.P. Thomas. “Theoretical Predictions of F-16 Fighter Limit Cycle Oscillations for Flight Flutter Testing”. *Journal of Aircraft*, 46(5):1667–1672, 2009.
16. Hajj, Muhammad R. and Philip S. Beran. “Identification of Nonlinearities Responsible for Limit Cycle Oscillations of Fighter Aircraft”. 48th AIAA/ASME/ASCE/AHS/ASC Structures, Structural Dynamics, and Materials Conference, Honolulu HI, April 2007.
17. Hasminoto, Atsushi, Takashi Ishada, Yuya Ohmichi, Takashi Aoyama, Takahiro Yamamoto, and kenji Hayashi. “Current Progress in Unsteady Transonic Buffet Simulation with Unstructured Grid CFD Code”. 2018 AIAA Aerospace Sciences Meeting, Kissimmee, Florida, 2018.
18. Hodges, Dewey H. and G. Alvin Pierce. *Introduction to Structural Dynamics and Aeroelasticity*. Cambridge University Press, New York NY, first edition, 2002.
19. Janardhan, Eastep, Grandhi and Sanders. “Parametric Studies of Transonic Aeroelastic Effects of an Aircraft Wing/Tip Store”. *Journal of Aircraft*, 42(1):253–263, 2005.
20. Maxwell, Daniel L., Jr. Charles M. Denegri, Kenneth S. Dawson, and James Dubben. “Effect of Underwing Store Aerodynamics on Analytically Predicted F-16 Aeroelastic Instability”. 48th AIAA/ASME/ASCE/AHS/ASC Structures, Structural Dynamics, and Materials Conference, Honolulu HI, April 2007.
21. Meijer, J. J. and Jr. A. M. Cunningham. *Understanding and Development of a Prediction Method of Transonic Limit Cycle Oscillation Characteristics of Fighter Aircraft*. Technical Report ICAS-92.6.4.3, 1992.
22. Melville, Reid. “Aeroelastic Instability of Tactical Aircraft in Nonlinear Flow Regimes”. 32nd AIAA Fluid Dynamics Conference, St. Louis MO, June 2002.
23. Mignolet, M.P. and D.D. Liu. “On the Nonlinear Structural Damping Mechanism of the Wing/Store Limit Cycle Oscillation”. *AIAA Archive Set 709*, 2148–2161, January.
24. Nikbay, Melike, Pinar Acar, and Zhicao Zhang. “Euler Solver Based Aeroelastic Predictions for Steady and Unsteady Flow Characteristics of HIRENASD Wing”. SI organization, 2018.

25. Parker, Gregory H., Raymond C. Maple, and Philip S. Beran. “Analysis of Store Effects on Limit-Cycle Oscillation”. 47th AIAA/ASME/ASCE/AHS/ASC Structures, Structural Dynamics and Materials Conference, Newport RI, May 2006.
26. Rokoni, A. A. and A. B. M. T. Hasan. “Prediction Of Shock Induced Buffet Onset for Flow Over a Supercritical Airfoil”. International Conference on Mechanical Engineering, Dhaka, Bangladesh, December 2011.
27. Tang, L., R.E. Bartels, P.C. Chen, and D.D.Liu. “Simulation of Transonic Limit Cycle Oscillations Using a CFD Time-Marching Method”. AIAA Paper 2001-1290, 2001.
28. Tauer, Thomas M. *Identifying Non-linear Aerodynamic Phenomena Contributing to F-16 Limit Cycle Oscillation*. Master’s thesis, Air Force Institute of Technology, 2015.
29. Tijdeman, H. and R. Seebass. “Transonic Flow Past Oscillating Airfoils”. *Annual Review of Fluid Mechanics*, 12(8157):181–222, 1980.
30. Toth, Raymond G., Rober A. Canfield, and Reid Melville. “Non-Linear Transonic Flutter Analysis for F-16 Stores Configuration Clearance”. 43rd AIAA/ASME/ASCE/AHS/ASC Structures, Structural Dynamics, and Materials Conference, Denver CO, April 2002.
31. Zhang, Z., F. Liu, and D.M. Zhuser. “An Efficient Euler Method on Non-Moving Cartesian Grids with Boundary-Layer Correction for Wing Flutter Simulations”. 44th AIAA Aerospace Sciences Meeting and Exhibit., Reno, Nevada, 2006.
32. ZONA Technology, Inc., 9489 E. Ironwood Square Drive, Scottsdale, AZ 85258-4578. *ZEUS Version 3.7 User’s Manual*, 4 edition, February 2012.
33. ZONA Technology, Inc., 9489 E. Ironwood Square Drive, Scottsdale, AZ 85258-4578. *ZAERO Version 9.2 Theoretical Manual*, 11-16 edition, November 2016.

Vita

Lt Dylan Hope was born in Singapore and raised in Spring, TX. He graduated from Klein Collins High School in 2012 and subsequently attended the United States Air Force Academy where he earned a Bachelor of Science degree in Aeronautical Engineering in 2016. Following Lt Hope's commission, he began his AFIT master's degree program in the fall of 2016; this thesis completes his degree requirements to earn a Master of Science degree in Aeronautical engineering.

Permanent address: 2950 Hobson Way
Air Force Institute of Technology
Wright-Patterson AFB, OH 45433

REPORT DOCUMENTATION PAGE			<i>Form Approved</i> OMB No. 0704-0188		
The public reporting burden for this collection of information is estimated to average 1 hour per response, including the time for reviewing instructions, searching existing data sources, gathering and maintaining the data needed, and completing and reviewing the collection of information. Send comments regarding this burden estimate or any other aspect of this collection of information, including suggestions for reducing this burden to Department of Defense, Washington Headquarters Services, Directorate for Information Operations and Reports (0704-0188), 1215 Jefferson Davis Highway, Suite 1204, Arlington, VA 22202-4302. Respondents should be aware that notwithstanding any other provision of law, no person shall be subject to any penalty for failing to comply with a collection of information if it does not display a currently valid OMB control number. PLEASE DO NOT RETURN YOUR FORM TO THE ABOVE ADDRESS.					
1. REPORT DATE (DD-MM-YYYY) 22-03-2018		2. REPORT TYPE Master's Thesis	3. DATES COVERED (From — To) Aug 2016 – Mar 2018		
4. TITLE AND SUBTITLE An Efficient Euler Method to Predict Shock Migration on an Oscillating Straked Delta Wing Design			5a. CONTRACT NUMBER		
			5b. GRANT NUMBER		
			5c. PROGRAM ELEMENT NUMBER		
6. AUTHOR(S) Hope, Dylan N., 2d Lt, USAF			5d. PROJECT NUMBER		
			5e. TASK NUMBER		
			5f. WORK UNIT NUMBER		
7. PERFORMING ORGANIZATION NAME(S) AND ADDRESS(ES) Air Force Institute of Technology Graduate School of Engineering and Management (AFIT/ENY) 2950 Hobson Way WPAFB OH 45433-7765			8. PERFORMING ORGANIZATION REPORT NUMBER AFIT-ENY-18-M-264		
9. SPONSORING / MONITORING AGENCY NAME(S) AND ADDRESS(ES) Air Force SEEK EAGLE Office (46 SK/SKC) ATTN: Dr. Chuck Denegri 205 West D Ave Suite 348 Eglin AFB FL 32542-6866 Charles.Denegri@eglin.af.mil (850) 882-0396 (DSN: 872-0396)			10. SPONSOR/MONITOR'S ACRONYM(S) AFOSR		
			11. SPONSOR/MONITOR'S REPORT NUMBER(S)		
12. DISTRIBUTION / AVAILABILITY STATEMENT DISTRIBUTION STATEMENT A. Approved for public release. Distribution Unlimited.					
13. SUPPLEMENTARY NOTES This material is declared a work of the U.S. Government and is not subject to copyright protection in the United States.					
14. ABSTRACT In support of the Air Force Office of Scientific Research, this project sought to identify the significance of nonlinear aerodynamic phenomena in regards to LCO of a straked delta wing design. Previous works include unsteady Navier-Stokes aeroelastic analysis of various wing designs and flight test of F-16 transonic LCO with interest focused on oscillatory SITES behavior. The research presented within this investigation further expanded the understanding of unsteady aerodynamics by performing aeroelastic analysis of a wing oscillated in pitch with an Euler-based, boundary layer coupled numerical method (ZEUS). The wing was tested for a multitude of LCO parameters such as median AoA, oscillation amplitude, oscillation frequency, Mach number, and the type of numerical solver used. Computed pressure data sets were analyzed along the wing's surface at 4 chordwise stations along the wing's span. Results indicate that oscillatory shock migration occurs in response to the pitching motion of the wing. ZEUS has the capability to run either a fully inviscid solution or a boundary layer coupled solution (BLC). While the use of both methods found shock migration to occur, the BLC solution predicted more significant shock migration. The inviscid solution predicted more aggressive shocks located further aft on the wing than the BLC solution. In regards to oscillation amplitude, increasing the amplitude resulted in a greater range of shock migration than lower amplitude cases. Both oscillation frequencies tested did not show any noteworthy differences. The aforementioned findings support the theory that potential oscillatory shock migration can occur during certain cases of transonic LCO. In addition, it was concluded that based on the flow solver used (ZEUS), shock movement during LCO is not purely a function of viscosity (SITES), although the modeling of viscous effects does affect the range of shock migration.					
15. SUBJECT TERMS Flutter Limit Cycle Oscillation LCO SITES F-16					
16. SECURITY CLASSIFICATION OF:		17. LIMITATION OF ABSTRACT UU	18. NUMBER OF PAGES 158 136	19a. NAME OF RESPONSIBLE PERSON Dr. Donald Kunz	
a. REPORT U	b. ABSTRACT U			c. THIS PAGE U	19b. TELEPHONE NUMBER (Include Area Code) (937)255-3636, ext 4548 Email: Donald.Kunz@afit.edu